

**A Thesis Submitted for the Degree of PhD at the University of Warwick**

**Permanent WRAP URL:**

<http://wrap.warwick.ac.uk/166868>

**Copyright and reuse:**

This thesis is made available online and is protected by original copyright.

Please scroll down to view the document itself.

Please refer to the repository record for this item for information to help you to cite it.

Our policy information is available from the repository home page.

For more information, please contact the WRAP Team at: [wrap@warwick.ac.uk](mailto:wrap@warwick.ac.uk)



# Microswimmer Navigation in External Fields

by

**Simone Coppola**

**Thesis**

Submitted to the University of Warwick

for the degree of

**Doctor of Philosophy**

**Department of Physics**

December 2021

# Contents

<b>List of Figures</b>	<b>iv</b>
<b>Acknowledgments</b>	<b>vi</b>
<b>Declarations</b>	<b>viii</b>
<b>Abstract</b>	<b>ix</b>
<b>Chapter 1 Introduction</b>	<b>1</b>
<b>Chapter 2 Theory</b>	<b>4</b>
2.1 Pushers and Pullers . . . . .	6
2.2 Biological Microswimmers . . . . .	7
2.2.1 <i>Chlamydomonas reinhardtii</i> . . . . .	7
2.2.2 Bacteria . . . . .	8
2.2.3 Sperm . . . . .	10
2.3 Swimmers in High Viscosity Media . . . . .	11
2.3.1 Chlamydomonas in High viscosity Media . . . . .	12
2.3.2 Sperm in High Viscosity Media . . . . .	13
2.4 Microswimmers in Viscosity Gradients . . . . .	15
2.4.1 Viscotaxis by Shape . . . . .	15
2.4.2 Viscotaxis by Swimming Gait . . . . .	16
2.5 Microswimmers in Complex Environments . . . . .	19
2.5.1 Microswimmer Interaction with Plain Walls . . . . .	19
2.5.2 Microbial Motion Rectification . . . . .	21
2.6 Microswimmers in Temperature Gradients . . . . .	23
2.6.1 Sperm Thermotaxis . . . . .	24
<b>Chapter 3 Methodology</b>	<b>27</b>
3.1 Microfluidics Device Preparation . . . . .	27

3.2	Microscopy and Image Processing Techniques . . . . .	30
3.2.1	Particle Tracking . . . . .	30
3.3	Microbiology Techniques . . . . .	33
3.3.1	<i>Chlamydomonas reinhardtii</i> . . . . .	33
3.3.2	Bacteria . . . . .	33
3.3.3	Sperm . . . . .	34
<b>Chapter 4 <i>Chlamydomonas reinhardtii</i> behaviour at sharp viscosity interfaces</b>		<b>35</b>
4.1	Introduction . . . . .	35
4.2	Methods . . . . .	37
4.3	Results and Discussion . . . . .	39
4.3.1	Velocity Distributions & Motility Characterization . . . . .	39
4.3.2	Scattering at the Interface . . . . .	42
4.3.3	Concentration Profile . . . . .	44
4.4	Conclusions . . . . .	45
<b>Chapter 5 Ram Sperm behaviour at sharp viscosity interfaces</b>		<b>47</b>
5.1	Introduction . . . . .	47
5.2	Experimental Details . . . . .	48
5.2.1	Media and Sample Preparation . . . . .	48
5.2.2	Experimental Setup & Imaging . . . . .	48
5.2.3	Data Analysis and Flagella Tracing . . . . .	50
5.3	Results & Discussion . . . . .	52
5.3.1	Ram Sperm Motility in High Viscosity Media . . . . .	52
5.3.2	Crossing Viscosity Interfaces . . . . .	53
5.4	Conclusions . . . . .	55
<b>Chapter 6 Curved Ratchets improve Bacteria Rectification in Microfluidics Devices</b>		<b>58</b>
6.1	Introduction . . . . .	58
6.2	Methodology . . . . .	60
6.2.1	Microscopy and Imaging . . . . .	61
6.3	Experimental Results . . . . .	62
6.3.1	Concentration Curves . . . . .	62
6.3.2	Ratchet Comparison . . . . .	64
6.4	Numerical Simulation . . . . .	67
6.5	Conclusions . . . . .	70



<b>Chapter 7</b>	<b>Bull Sperm Thermotaxis</b>	<b>72</b>
7.1	Introduction . . . . .	72
7.2	Experimental Details . . . . .	73
7.2.1	Sperm Preparation . . . . .	73
7.2.2	Experimental Setup . . . . .	73
7.2.3	Device Preparation and Imaging Details . . . . .	75
7.3	Results . . . . .	76
7.3.1	Sperm Motility as a function of Temperature . . . . .	76
7.3.2	Sperm Thermotaxis . . . . .	79
7.4	Conclusions . . . . .	82
<b>Chapter 8</b>	<b>Conclusions</b>	<b>83</b>

# List of Figures

2.1	Microswimmer Deformations . . . . .	5
2.2	Microswimmer Flow Fields . . . . .	7
2.3	The structure and flow field of <i>Chlamydomonas reinhardtii</i> . . . . .	9
2.4	The run-and-tumble behaviour of <i>E. coli</i> . . . . .	10
2.5	The structure of a sperm cell . . . . .	11
2.6	Sperm Swimming in low and high viscosity . . . . .	14
2.7	Negative Viscotaxis of Triangular Swimmers . . . . .	17
2.8	Uni-axial swimmers in Viscosity Gradients . . . . .	18
2.9	Pusher and pullers in Viscosity Gradients . . . . .	19
2.10	Pushers and Pullers approaching a planar wall . . . . .	21
2.11	V-Shaped Ratchets for Microbial Motion Rectification . . . . .	22
2.12	Chirality-based Particle Separation . . . . .	23
2.13	Sperm Sorting in Microfluidics Devices . . . . .	24
2.14	Sperm Thermotaxis Device . . . . .	26
3.1	The Photolithography Process . . . . .	29
3.2	Microscopy Methods . . . . .	31
3.3	Image Processing for Particle Tracking . . . . .	32
4.1	Microfluidic device for Sharp Viscosity Gradient Generation . . . . .	38
4.2	The Relation between Swimming Velocity and Fluid Viscosity for <i>Chlamydomonas reinhardtii</i> algae . . . . .	40
4.3	Diffusion Properties of <i>Chlamydomonas reinhardtii</i> algae in Viscous Fluids . . . . .	41
4.4	<i>Chlamydomonas reinhardtii</i> Scattering Events at a Sharp Viscosity Interface . . . . .	43
4.5	Time evolution of <i>Chlamydomonas reinhardtii</i> concentration in a vis- cosity gradient . . . . .	46

5.1	Device for studying sperm behaviour at a viscosity interface . . . . .	49
5.2	Sperm Flagella Processing . . . . .	51
5.3	Sperm Velocity in High Viscosity Media . . . . .	53
5.4	Flagellar Beating properties in High Viscosity Media . . . . .	54
5.5	Scattering Angles for Sperm Crossing the Interface . . . . .	56
6.1	Microfluidics Device for Bacteria Rectification . . . . .	61
6.2	Concentration Curve for Different Ratchet Shapes . . . . .	64
6.3	The Residence Time of Bacteria on Ratchets . . . . .	65
6.4	Scattering from Outer Side of the Ratchet . . . . .	66
6.5	Probability Distribution of $\theta_{\text{out}}$ for different types of ratchet . . . . .	67
6.6	Scattering algorithm . . . . .	69
6.7	Bacteria Rectification Simulation results . . . . .	70
7.1	Thermotaxis Experiment Schematics . . . . .	74
7.2	Temperature Simulations for Thermotaxis Setup . . . . .	75
7.3	Velocity of Sperm Trajectories as a function of Temperature . . . . .	77
7.4	Sperm Motility at 30 and 40°C . . . . .	77
7.5	Flagella Motility as a function of Temperature . . . . .	78
7.6	The linear relationship between flagella and trajectory radius . . . . .	79
7.7	Sperm Thermotaxis Experiments . . . . .	80
7.8	Thermotaxis Reversal . . . . .	81

# Acknowledgments

Completing a PhD is no easy feat and it would not have been possible had I not been lucky enough to have many people who supported and helped me during the past three and a half years.

I would like to thank my supervisor, Dr. Vasily Kantsler for his support during the PhD. You were patient with me when I started and watching you work in the lab has been inspirational.

I also want to thank all the people I have had the pleasure to share an office and a lab with in the past few years, who have all at some point or another listened to me ramble about my work or life.

Max, thank you for not only being a great teacher and mentor but also an even better friend: you were there for me during both the worst and best times of this long journey, always happy to chat things over a cup of coffee and being the voice of reason. I'm not sure how many coffees and pints I owe you, but I hope one day I can make a dent in my debt!

Richard and Maria, thanks for all your teachings and wisdom. With Max, you helped me when I was clueless in the lab and I wouldn't be where I am at today without the knowledge I gained from you in those early months of the PhD.

Steve, thank you for always being a positive presence in the lab and in the office!

Stefan, thank you for listening to many of my rambles in the office and never saying no whenever I felt stuck with my work and wanted to go get a coffee to get out of the office!

Moving on to family, I want to thank my aunt "Zia Patti" for checking on me weekly during the course of the PhD. I know I don't get in touch as often as I should, but

you are always in my thoughts with the rest of the aunts, uncles and my amazing grandparents.

Mary, thank you for being patient with me and listening to my rambles every day! Your work ethic is superhuman and your passion for science contagious. Your positivity and energy make everyday better and more exciting.

Lastly, I want to thank my parents and my brother. You have been there for me every single day, supporting me in every single possible way - no matter the distance and the barriers. Without you, I wouldn't be who I am. This thesis is dedicated to you for you are my strength and wisdom.

# Declarations

I declare that this thesis reports the work I carried out between July 2018 and December 2021 under the supervision of Dr. Vasily Kantsler. The studies in this thesis have not been submitted either in full or in part to this or any other academic institution for the admission of a higher degree. In exception from where clearly indicated by reference in the text, any work reported in this thesis has been performed by myself.

Any views expressed in this thesis are those of the author.

Chapters 4 and 6 are based on manuscripts which have been published during the course of the PhD:

- Coppola, S., Kantsler, V. *Green algae scatter off sharp viscosity gradients*. **Sci Rep** 11, 399 (2021).
- Coppola, S., Kantsler, V. *Curved ratchets improve bacteria rectification in microfluidic devices*. **Phys. Rev. E** 104, 014602 (2021).

I was responsible for data acquisition, analysis and simulations for both manuscripts. Interpretation of the data was performed jointly with Dr. Vasily Kantsler. Both manuscripts were written by myself with help and comments from Dr. Vasily Kantsler.

# Abstract

We characterize the behaviour of the green alga *Chlamydomonas reinhardtii* and ram sperm when they navigate through sharp viscosity gradients, showing that the swimming gait plays a key role in determining how a microswimmer is affected when crossing the interface between the two media.

In addition to that, we investigate how the temperature of the surrounding environment affects the motility of bull sperm, revealing a previously unreported phenomenon at high temperatures. We also study the thermotactic behaviour of bull sperm through the use of microfluidics, showing results in line with others published for different mammalian cells.

Lastly, we develop microfluidics devices which allow to control the swimming direction of bacteria and concentrate them in a specific region, using experiments and simulations to guide the design process and identify how to obtain the best results from bacteria rectification devices.

*There are two possible outcomes: if the result confirms the hypothesis, then you've made a measurement. If the result is contrary to the hypothesis, then you've made a discovery.*

—Enrico Fermi



# Chapter 1

## Introduction

The world surrounding us is rich with swimming biological microorganisms: from the algae in the sea to the bacteria in the ponds and our body, going through to the spermatozoa which allow fertilisation and life, microswimmers play a key role in many aspects of our existence.

A marvel of biological evolution for microorganisms has been the development of microbial motility. In fact, the majority of microorganisms share the ability of being able to swim thanks to whip-like appendages known as flagella (or cilia, depending on their properties) [1, 2].

Similarly to all other living organisms, microbes have developed ways to sense whether an environment is favourable for them and respond accordingly. For example, bacteria can sense a nutrient gradient if they are in one, and change their motion to swim towards a food source or away from any toxic environment [3]. The same principle is believed to be one of the main guidance mechanisms which lead the sperm to the egg and allow fertilization [4].

Chemical gradients are not the only changes in the environment to which microorganisms can respond. It has been shown that algae can respond to illumination gradients (phototaxis) [5], and both sperm and bacteria can respond to flow gradients (rheotaxis) [6, 7]. Similarly, it is possible to observe responses from topographical gradients (topotaxis) [8] and temperature gradients (thermotaxis) [9].

This response to a chemical gradient in the environment - known as chemotaxis - has been discovered in the late 1800s, but it was only in the past 50 years that research regarding it could be conducted in a systematic way thanks to a wide array of new modern techniques which have only recently become available.

Studying and understanding the behaviour of microorganisms when they face a gradient not only allows us to unlock the puzzle of many natural/biological phenomena,

but also opens up endless possibilities to merge our knowledge with the wonders of modern technologies and techniques to develop both research and biomedical tools to use these responses to our advantage [10, 11].

One of the modern tools that lets us study systematically microbial motility is microfluidics, through which it is possible to manipulate precisely small volumes of fluid ( $\mu\text{L}$ ) constrained in well-defined geometries. These devices, cheap and easy to use, can be utilised to generate gradients of all sorts to study how micro-organisms respond to them. Furthermore, specific geometries can be designed to take advantage of such responses and use them for bio-engineering purposes such as sperm sorting or drug delivery [12, 13].

The work presented in this thesis focuses on characterising the motility of a variety of microorganisms (bacteria, sperm and green algae) in different external environments. The results will focus not only on single cell motility, such as the scattering of *Chlamydomonas reinhardtii* off sharp viscosity gradients or how bacteria scatter off obstacles, but also on collective behaviour of the cells in the gradients.

The thesis will be structured as follows:

- **Chapter 2** presents a background in microbial motility, going from how microorganisms achieve locomotion in fluids to how swimming gaits affect how the microorganisms interact with their surrounding environment. This chapter will also put into context the results reported in this thesis by outlining key information already available in the literature;
- **Chapter 3** focuses on the techniques used to perform the motility experiments presented in this thesis. Topics such as microfluidics manufacturing and microscopy will be covered in this chapter. All the microbiology methods used to culture microorganism and prepare samples will also be discussed here;
- **Chapter 4** presents an experimental analysis of the behaviour of the green alga *Chlamydomonas reinhardtii* (CR) in two adjacent regions of significantly different viscosity. The results will focus on how CR behaves when crossing from one region to the other as well as showing a novel effect by which the algae concentrate in low viscosity regions.
- **Chapter 5** follows by showing how ram sperm behaves in the same type of environment as that outlined in Chapter 4. The results will highlight how the swimming gait of a microswimmer can affect navigation in viscosity gradients and lead to different results.
- **Chapter 6** presents a study on how bacteria rectification microfluidic devices

can be optimised by modulating the geometry of the ratchets used to rectify the motion. Through experiments and simulations, the results show bacteria rectification can be improved significantly by designing ratchets with curved geometries;

- **Chapter 7** focuses on the behaviour of bull spermatozoa in different temperatures, showing that bull sperm cells start swimming in circular trajectories at temperatures higher than 35°C. The behaviour of sperm cells in temperature gradients will also be studied, showing that bull sperm cells navigate to higher temperatures in a gradient.
- **Chapter 8** concludes the thesis with a summary of the major findings presented in Chapters 4-7.

## Chapter 2

# Theory

Microswimmers use whip-like appendages (cilia or flagella) to move the fluid around them and achieve locomotion [2]. Assuming incompressibility, the dynamics of a Newtonian fluid surrounding the microswimmer can then be described by the *Navier-Stokes equation*:

$$\rho \left( \frac{\partial \mathbf{v}}{\partial t} + (\mathbf{v} \cdot \nabla) \cdot \mathbf{v} \right) = \eta \nabla^2 \mathbf{v} - \nabla p + \mathbf{f}, \quad (2.1)$$

where  $\rho$  is the fluid density,  $\eta$  is the fluid viscosity and  $\mathbf{v}(\mathbf{r}, t)$ ,  $p(\mathbf{r}, t)$  and  $\mathbf{f}(\mathbf{r}, t)$  are the microswimmer velocity field, pressure field and applied body force respectively [14].

It is possible to qualitatively describe the characteristics of the flow obtained solving the Navier-Stokes equation by introducing a dimensionless quantity called *Reynolds number*. The Reynolds number  $Re$  can be defined as the ratio between the inertial terms in Eq. 2.1,  $\sim \rho(\mathbf{v} \cdot \nabla) \cdot \mathbf{v}$  to the viscous forces per unit volume,  $\sim \eta \nabla^2 \mathbf{v}$  so that

$$Re = \frac{\text{inertial forces}}{\text{viscous forces}} = \frac{\rho v_0 L}{\eta}, \quad (2.2)$$

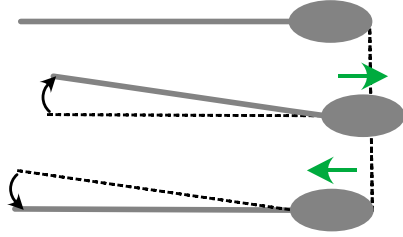
where  $L$  and  $v_0$  are the characteristic length and speed of the microswimmer.

If we consider typical numbers for the microorganisms studied in this thesis, i.e.  $L \approx 10 \mu\text{m}$  and  $v_0 \approx 50 \mu\text{m/s}$  swimming in water ( $\eta/\rho = 10^{-6} \text{ m}^2/\text{s}$ ) we calculate the Reynolds number to be  $\approx 10^{-3}$ .

This result shows swimming at the microscale is dominated by viscous forces, thus meaning we can discard inertial terms from Eq. 2.1 and rewrite it as

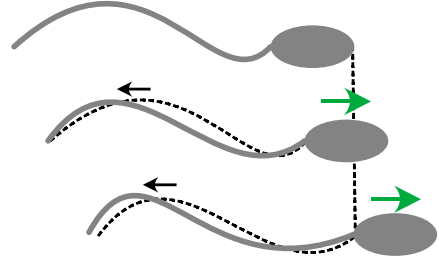
$$\nabla p - \eta \nabla^2 \mathbf{v} = \mathbf{f}, \quad (2.3)$$

## Reciprocal motion



zero net displacement!

## Non-reciprocal motion



positive net displacement!

Figure 2.1: Two different types of swimmer deformation. On the left, reciprocal motion which does not lead to locomotion due to its time reversibility. On the right, a type of non-reciprocal motion (flexible oar) which leads to locomotion of the microswimmer.

which is known as the *Stokes' Equation*.

One peculiar property of the Stokes' equation is the absence of any time-dependence. Therefore, since the equation is fully symmetric under time reversal, not all swimming mechanisms will allow microorganisms to achieve locomotion.

This consequence was the main topic of Edward Purcell's seminal talk "Life at Low Reynolds number", in which he coined the famous "Scallop Theorem" [15].

The theorem states that swimmers undergoing time-symmetric deformations in the low Reynolds number regime will not be able to produce any net displacement i.e. a scallop opening and closing its shell will just move back and forth.

How do microswimmers achieve locomotion then? Purcell mentions two possible solutions to the low Reynolds number constraints, which he names the "flexible oar" and the "corkscrew". The flexible oar fixes the problem of time-reversability by allowing the flagellum to bend one way during the first part of the stroke, and another during the second part. This roughly corresponds to how sperm cells and the green alga *Chlamydomonas reinhardtii* swim (see later sections). In the corkscrew case, the flagellum moves like a corkscrew which is constantly being rotated. This also solves time-reversability and corresponds to how bacteria move.

Being able to disregard inertial effects has also consequences on how the environment surrounding the swimmer responds to any changes due to flagellar movement. In fact, at low Reynolds number Newton's second law just becomes a statement of instantaneous balance between fluid and external forces and torques

$$\mathbf{F}_{\text{ext}}(t) + \mathbf{F}(t) = \mathbf{0}, \quad (2.4)$$

$$\mathbf{L}_{\text{ext}}(t) + \mathbf{L}(t) = \mathbf{0}, \quad (2.5)$$

where  $\mathbf{F}_{\text{ext}}(t) = \mathbf{L}_{\text{ext}}(t) = \mathbf{0}$  for most cases, excluding cases of bottom-heavy or nose-heavy cells, in which the external torque  $\neq \mathbf{0}$ .

Such instantaneous balance between fluid and external forces and torques means that the fluid responds instantaneously to any boundary motion, such as the flagellar beating of microorganisms [2, 14].

## 2.1 Pushers and Pullers

To fully understand the flow field generated by microswimmers, it is necessary to solve the Stokes' equation (Eq. 2.3). Thanks to its linearity, it is possible to construct solutions relating to complex pressure and velocity fields by superposing solutions for simpler ones [16].

We now consider the simplest case Eq. 2.3 can be solved for, i.e. the flow generated by a Dirac-delta forcing of the form  $\mathbf{f} = \delta(\mathbf{x})\hat{\mathbf{e}}$ .

In this case, the resulting velocity field can be expressed as

$$\mathbf{v}(\mathbf{r}) = \frac{1}{8\pi\eta r} \left[ \hat{\mathbf{e}} + \frac{(\mathbf{r} \cdot \hat{\mathbf{e}})\mathbf{r}}{r^2} \right], \quad (2.6)$$

This solution is known as a *stokeslet* and has two key properties: (i) the velocity field decays as  $1/r$  and (ii) the locomotion it induces has a directional anisotropy. In fact, it is possible to show that the velocity in the direction parallel to the that of the applied force is  $v_{\parallel} = 1/4\pi\eta r$ , whereas the velocity in the direction perpendicular to the applied force is  $v_{\perp} = 1/8\pi\eta r$ . Such anisotropy is at the basis of the drag-based method of swimming used by microorganisms [14].

However, most microswimmers do not move through an external force, but they do so autonomously by moving their flagella and applying a force on the fluid. In such cases, the total net force applied by the swimmer on the fluid and vice-versa must be equal to zero due to the properties of the low Reynolds number regime.

As previously mentioned Eq. 2.3 lacks any non-linear terms, thus allowing us to represent more complicated flow fields as a superposition of singular solutions. One of such solutions is the *Stokes dipole*, which can be thought of as flow field generated by two nearby and opposing point forces. A Stokes dipole flow field can be expressed as

$$\mathbf{v}(\mathbf{r}) = \frac{P}{8\pi\eta r} [3(\mathbf{r} \cdot \hat{\mathbf{e}})^2 - 1], \quad (2.7)$$

where  $P$  is the magnitude of the force dipole [2]. As it will be shown in later sections of this chapter, it has been found that the velocity field generated by a Stokes dipole describes remarkably well the far-field hydrodynamics (i.e. at a distance much larger than that of its body) of many biological microorganisms, such as bacteria, sperm or *Chlamydomonas reinhardtii* [17, 18].

Similarly to electrical charges, it is also possible to distinguish between two types of flow dipoles. A microorganism which has its motor in the back and drags its passive body in front of it can be referred to as a *pusher*. On the other hand, a microswimmer whose motor is in the front, and drags his body behind is commonly called *puller*. It is possible to see in Fig. 2.2 that the two flow fields are very similar but have opposite directions [19].

Lastly, it is worth noting that the equations and results mentioned so far only apply for microorganisms swimming in *free space* i.e. they do not include any effects due to confinement or wall interactions. Those topics are discussed in latter parts of this introductory chapter, in which it will be shown that the sign of a force dipole has important consequences on the swimmer's interaction with planar walls [20, 21].

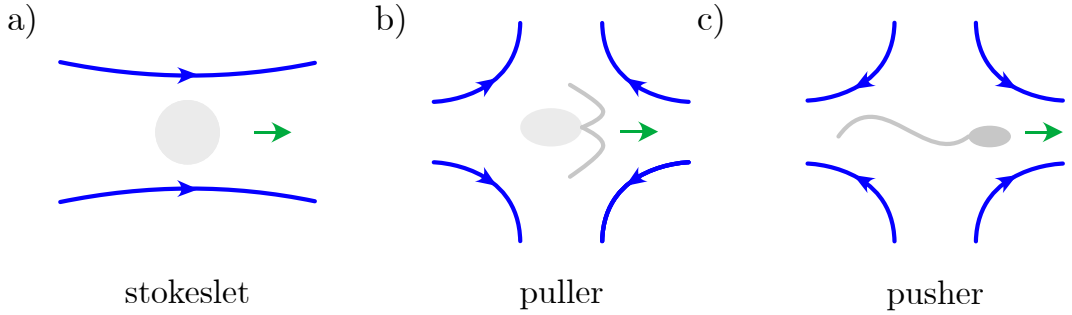


Figure 2.2: a) flow field from a point force (i.e. stokeslet) compared to those from force dipoles solutions for puller (b) and pusher (c) microswimmer

## 2.2 Biological Microswimmers

In the previous section I discussed the hydrodynamics of ideal microswimmers, starting from the Navier-Stokes equation. In this section, I will introduce the microorganisms used to perform the experiments reported in this thesis.

### 2.2.1 *Chlamydomonas reinhardtii*

*Chlamydomonas reinhardtii* (CR) is a unicellular green alga which has garnered a lot of attention from the active matter community in the past decade, often being

referred to as the “premier model microswimmer”. CR owes its success to three main factors: (i) how easy it is to grow in the lab (see Methodology Chapter), (ii) the large variety of strains available, which offer ample experimental possibilities and (iii) how closely its hydrodynamic signature resembles that of an ideal “puller” microswimmer [17, 22].

CR can be roughly described as a  $10\mu\text{m}$  diameter spheroid which contains all standard eukaryotic organelles (see Fig. 2.3). The cell has a front-back asymmetric architecture due to its basal 2/3 being occupied by the chloroplast, through which CR achieves photosynthesis. CR cells also have an eyespot, which can be found in the upper half of the cell and is used by CR to swim towards light (phototaxis). Lastly, it is possible to find two basal bodies at the apex of the cell body, from which the  $10\text{--}12\mu\text{m}$  long flagella extend [5].

CR flagella beat at 50 Hz in a breaststroke-like manner in which it is possible to distinguish two phases: a power stroke and a recovery stroke [11]. The flagella beat synchronously, although there is the possibility for them to get out of phase causing the cell to quickly re-orient (similar to the run-and-tumble motion of bacteria, see next section) [23]. It is also possible to observe the two flagella displaying flagellar type (corkscrew-like) beating, particularly in response to a shock from the surrounding environment [24].

Numerous studies have been carried out to identify the hydrodynamic field of CR. These have revealed complex time dependent fields, which change depending on the beating phase. Interestingly, however, it has been shown that the time average fluid flow of CR matches that of a model “puller” microswimmer [11, 17]. This allowed CR to gain a lot of attention from the experimental active matter community, as now CR is regularly used as an experimental model microswimmer.

### 2.2.2 Bacteria

Bacteria - in particular *Escherichia coli* - were the first microorganism to gain attention from the biophysical community in the 1970s, thanks to work of H. C. Berg [25, 26]. Similarly to CR, bacteria are quite easy to grow and their genome has been studied in detail, thus allowing numerous modified strains to be made (non-tumbling smooth swimmer, fluorescent etc.) and a wide variety of systems to be investigated experimentally. Studying bacteria has a wide range of applications, from understanding antibiotic resistance and making smart materials to studying complex active statistical physics systems [1].

Bacteria can have a variety of shapes, flagella positions etc. To avoid confusion, in this work I will be referring only to bacteria whose flagella have *peritrichous*



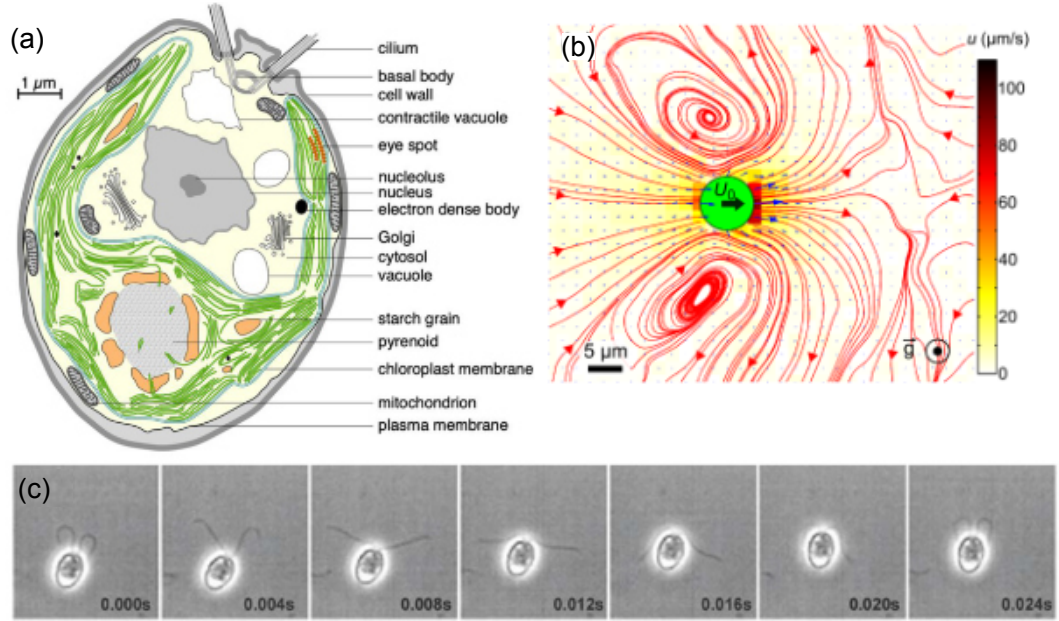


Figure 2.3: a) detailed structure of a *Chlamydomonas reinhardtii* cell and (b) of the average flow field it generates when swimming. (c) is an image sequence showing the “breaststroke” beating pattern. Adapted from [17] and [22].

arrangement. These bacteria are usually rod-shaped, with a length of  $\sim 1\mu\text{m}$  and flagella which can grow anywhere on their bodies. The flagella are powered by a motor placed at their base, where the flagella connect to the body [27].

Bacteria swim by bundling up their flagella when they all move counterclockwise. Even just one flagellum desynchronizing will cause the bundle to open up, and the bacteria to undergo a sharp re-orientation (see Fig. 2.4). This type of motion is known as run-and-tumble, and its rate ( $\sim 1\text{Hz}$  in normal conditions) is affected by the chemicals surrounding the bacteria. In fact, bacteria will tumble more when they are in a favourable region, such as one rich with nutrients, to increase the amount of time spent there. It is also possible to obtain “smooth” swimming bacteria by removing the receptors responsible for chemotaxis, effectively disabling the ability to tumble for the bacteria. In this case, the bacteria still experience thermal fluctuations on their orientations, similar to a Brownian particle, but they will not tumble and re-orient sharply every second [25, 28].

Similarly to CR, numerous studies have been made to investigate the properties of the flow field generated by swimming bacteria. In particular, Drescher *et al.* showed that the flow field of a freely swimming bacterium matches surprisingly well the flow field of an ideal “pusher” microswimmer [17]. As we will see later, this plays a big role in how bacteria interact with surfaces and - in particular - how they accumulate

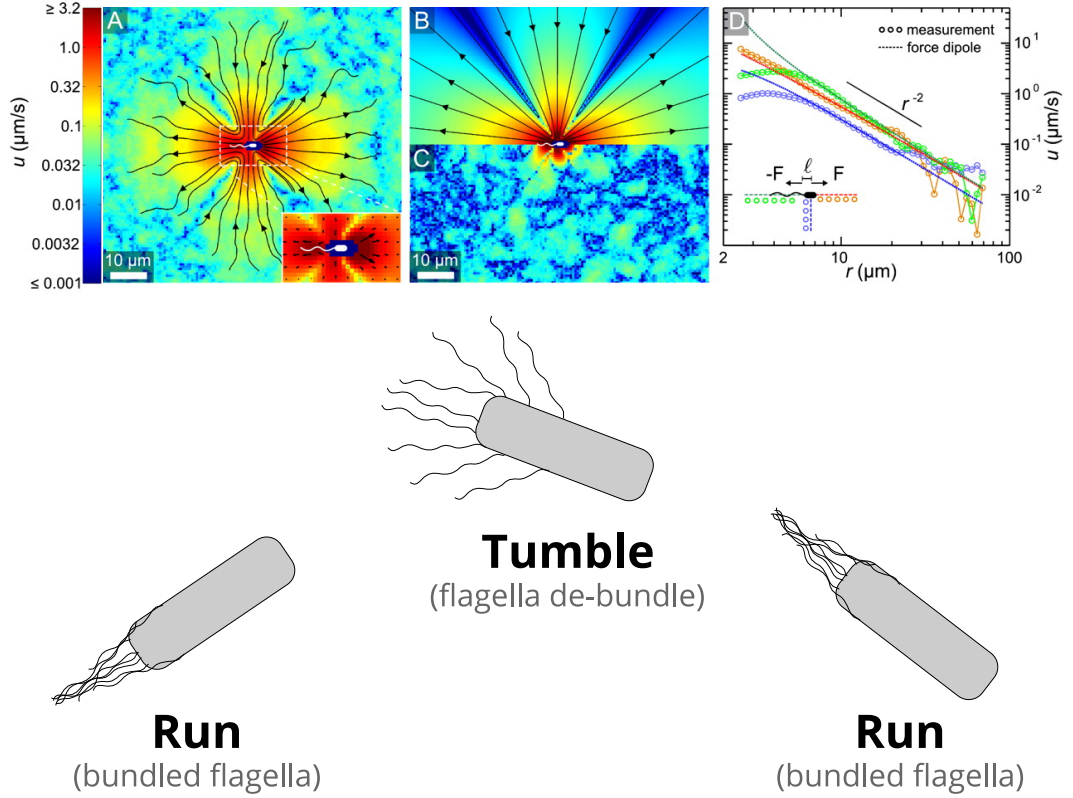


Figure 2.4: Top: the flow field of *E. coli* bacteria (A) Direct measurement, B) best fit of dipole flow C) residual flow field obtained by subtracting the best fit from the measurement D) radial decay of the flow field. Adapted from [18] Bottom: a schematic showing run-and-tumble motion for a peritrichous bacterium such as *E. coli*.

on them.

### 2.2.3 Sperm

Spermatozoa are the last of the microorganisms of interest in this thesis. It is worth noting that sperm cells of different species have different properties and can respond differently to the same stimuli. Nevertheless, it is possible to find some general properties which are common to sperm cells of all species.

Sperm cells are usually  $\sim 45\mu\text{m}$  long, with a  $3\text{--}5\mu\text{m}$  head and a  $40\mu\text{m}$  long flagella. The main structures which compose a sperm cell are its head, midpiece, principal piece and end piece (Fig. 2.5). In simple terms, the head is responsible for carrying the genetic material, the midpiece is where the ATP necessary for movement is produced by the mitochondria and the principal and end piece are what constitutes

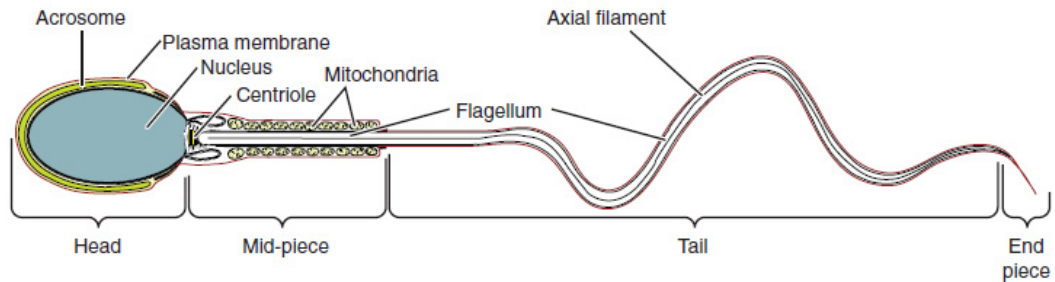


Figure 2.5: From [30]. The structure of mammalian spermatozoa.

the flagellum, i.e. the main motile appendage through which sperm cells swim. Needless to say, each of these elements has complex biological structures inside of them; however, these complexities are far beyond the scope of this thesis so the interested reader is invited to consult ref. [29] for a detailed discussion on the finer structures of mammalian sperm. It is important to highlight that, contrary to bacteria, the sperm flagellum is not driven by a single motor but forces are generated throughout the flagellum by dynein motors.

Sperm swims by beating its flagellum in a snake-like manner. In order to overcome the time-reversability constraints put in place by the Scallop Theorem, the flagellar beat can be described as a propagating bending wave with wavelengths smaller than the flagella length.

No direct measurements of the flow field around a sperm cell exist, however many detailed studies have been carried out on the details of its flagellar beating. Through these studies researchers have reconstructed the flow field generated by human sperm cells, showing they can be classified as “pusher” microswimmers [31, 32].

## 2.3 Swimmers in High Viscosity Media

In nature, microorganisms often find themselves swimming in a variety of environments with different viscosity - therefore having to adapt to the surrounding conditions in order to survive.

The properties of the fluid in which a microorganism swims plays a fundamental role in its behaviour and can affect its motility in a variety of ways, from changing its swimming gait to modulating its velocity. Fluid viscosity has in fact been shown to affect significantly the flagellar beating of spermatozoa or *Chlamydomonas reinhardtii*, thus altering their swimming velocity, rotational diffusion and other properties of their motion.

Microswimmer response to highly viscous environments depends on a number of

factors, including their hydrodynamic signature, their swimming gait as well as their shape and evolutionary adaptation to high viscosity environments. For example, while high viscosity slows down *Chlamydomonas reinhardtii* algae, it has been shown to increase the velocity of sperm and bacteria, most likely due to their ability to adapt their swimming gait in order to navigate through high viscosity mucus regions [31–33].

Often microswimmers have to navigate environments of spatially inhomogeneous viscosity i.e. go through different regions with varying viscosity. For this reason, understanding microbial motility in high viscosity regions is only one part of the story, with the other revolving around how a microswimmer navigates an environment whose viscosity changes as a function of position.

In this section, I will outline the results currently available in the literature for *Chlamydomonas reinhardtii* and sperm swimming in uniform, high viscosity media. These results will provide a starting point to deal with microswimmers in viscosity gradients, which will be the topic of the next section and of results Chapters 4 and 5.

### 2.3.1 *Chlamydomonas* in High viscosity Media

Despite the numerous theoretical and simulation works carried out on the matter of microswimmers in high viscosity media, not many experimental investigations on the matter have been carried out until recent years.

Recently, Qin *et al.* studied in detail how *Chlamydomonas reinhardtii* motility is affected when it swims through high viscosity media. Through their analysis, they were able to confirm the prediction that not only the swimming velocity of the algae would be affected, but also how they beat their flagella and how frequently they do so.

In particular, the authors showed that the beating frequency of CR flagella decreases with viscosity  $\mu$  consistently with the relation  $\omega \sim 1/\sqrt{\mu}$ . This relation is in agreement with predictions made by theory models indicating that flagellar beating is controlled by internal processes as well as the properties of the flagellum and those of the surrounding environment (i.e. the viscosity of the fluid is only one part of the equation) [34].

Furthermore, results indicate that velocity is inversely proportional to viscosity - suggesting that the algae operate at a constant thrust in the viscosity range of interest in this work.

More detailed experimental work on the effect of viscosity on the flagellar beating of CR algae has been carried out by Wilson *et al.* and Bottier *et al.* [35, 36].

As well as showing agreement with what had been previously been published, the work also shared some more insights on how CR behaves in high viscosity media. In particular, through detailed resistive force calculations, the authors were able to show that the force required to overcome viscous drag scales with the length of the flagella.

On top of that, the authors showed with detail how the flagellar waveforms adapt to increase efficiency at higher viscosity by increasing their curvature, an effect also seen by Qin *et al.* which points out to a possible mechanosensory response by CR in which the flagellar beating shape is adapted when in cases of high mechanical loads. It is important to mention that the works described in this section investigate the behaviour of CR in fluids with viscosity up to 10 times that of water, while the experiments reported in Chapter 4 deal with CR swimming in media with viscosity up to 60 times that of water. Nevertheless, the results outlined in this section offer a first point of reference to interpret the results, particularly in the lower viscosity regimes.

### 2.3.2 Sperm in High Viscosity Media

On their way to the egg, sperm cells have to navigate environments of varying viscosity, with regions reaching viscosities over 100 times that of water [37]. For this reason, understanding sperm motility in high viscosity regions has been the subject of many studies ever since the work of Kremer, who showed a sperm cell's ability to navigate through the viscoelastic mucus or viscous analogue is a good predictor of the sperm fertility potential [38].

Thanks to the possibilities offered by modern high speed microscopy and data analysis tools, research has been carried out to understand in detail how sperm motility changes in high viscosity environments.

One of the peculiar properties of sperm swimming in high viscosity fluids is the retention of progressive speed by sperm cells even at viscosities above 100 times that of water [32, 39]. This is particularly striking when compared to the aforementioned *Chlamydomonas reinhardtii*, which instead has its swimming velocity affected significantly by the increase in viscosity of its surroundings.

One immediate difference between sperm swimming in low and high viscosity is the reduction in sperm head yawing. As highlighted in Fig. 2.6, there is considerable amount of yawing in low viscosity, whereas trajectories in high viscosity do not exhibit the same amount of yawing. Reduction in yawing has been highlighted to be one of the main factors allowing sperm to improve its swimming efficiency at high viscosity and retain most of its velocity, but it is not the only change observed.

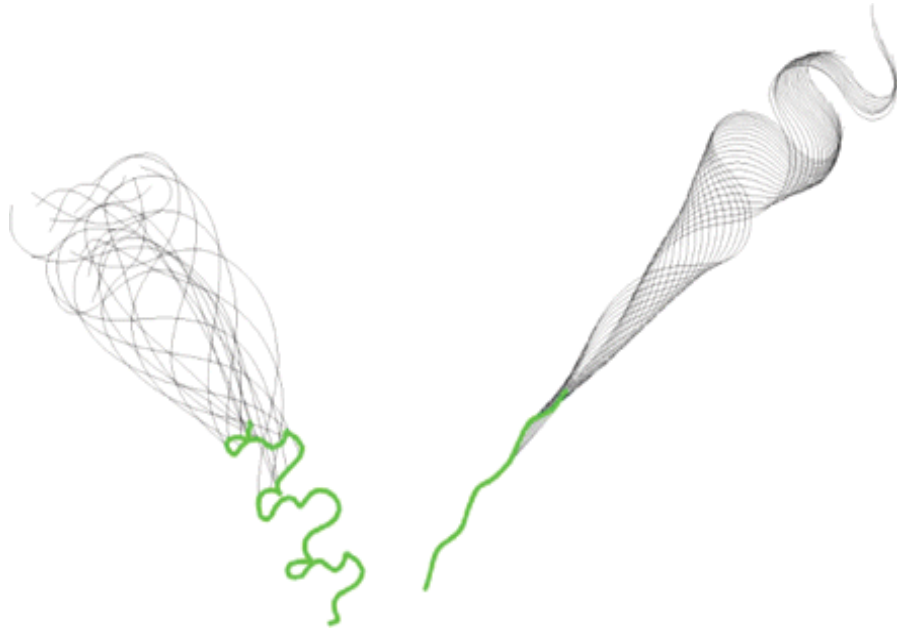


Figure 2.6: Left: human sperm swimming in low viscosity medium (as viscous as water). Right: human sperm swimming in high viscosity medium (approximately 100 times more viscous than water). The figure shows how yawing is reduced at higher viscosities, and how that flagellar shape changes to improve swimming efficiency (i.e. the progressive velocity is maintained despite the increase in viscosity). Note that the image displays only a full beating pattern per sperm cell. Adapted from [32].

Another key factor allowing sperm to retain most its velocity despite and observed reduction in beating frequency is the increase in the distance travelled per beat, this results in the conservation of the sperm progressive velocity.

This is achieved by a change in gait by which the wavelength of the bending wave travelling the flagellum increases as a function of viscosity, leading to a larger distance travelled per beat [32].

These results overall highlight how, due to its evolutionary needs, sperm cells have evolved to be able to navigate through high viscosity gradients by adjusting their gait accordingly.

We conclude this section highlighting that the results reported here concern human sperm, but similar trends have been reported for other mammalian species, such as

bull [40]. For this reason, we believe the results to be important to contextualise findings in Chapter 5, where the behaviour of ram sperm in high viscosity environments is studied.

## 2.4 Microswimmers in Viscosity Gradients

It should now be clear that fluid viscosity can affect significantly how microorganisms swim by modifying their swimming gait and - consequently - all properties associated with their motility i.e. velocity, rotational and translational diffusion etc. Understanding microbial motility in homogeneous environments of high viscosity provides us with a framework to start understanding many natural processes, but fails to provide us with detailed insight on the equally important phenomena in which microorganisms have to navigate through regions of inhomogeneous viscosity. In fact, such phenomena can occur in a variety of natural environments, ranging from how bacteria form biofilms to how spermatozoa navigate the female reproductive tract on their journey to the egg.

Despite this, not many experimental investigations have been carried out on the matter. On the contrary, a number of theoretical studies have been published in recent years, studying how shape [41] or swimming gait [42] can lead to different responses in the presence of a viscosity gradient.

These studies can provide us with a solid framework to interpret and analyse the experimental results which will be shown in later chapters, and will now be outlined.

### 2.4.1 Viscotaxis by Shape

One approach to study the effects of a viscosity gradient on the swimming trajectories of microbial organisms is to analyse the viscous forces acting on different parts of its body as it navigates through the gradient. To do so, Liebchen *et al.* [41] modelled microswimmers as  $N$  rigidly connected spheres of radii  $b_i$  and midpoints  $\mathbf{r}_i = (x_i, y_i)$  with  $i = 1, \dots, N$ .

The spheres experience self-propulsion forces as well as viscous drag from the fluid, which can be found from Stoke's law so that  $\mathbf{F}_R(\mathbf{r}_i) = -6\pi b_i \eta(\mathbf{r}_i) \dot{\mathbf{r}}_i$ .

It's important to note that all viscosity gradients in this paper can be considered to have negligible changes on the scale of a single sphere, but results are qualitatively the same for sharp interfaces [43].

This way, it is possible to write the equations of motion for a microswimmer as

follows:

$$\sum [\mathbf{F}_i - 6\pi b_i \eta(\mathbf{r}_i) \dot{\mathbf{r}}_i] = \mathbf{0}; \quad (2.8)$$

$$\sum (\mathbf{r}_i - \mathbf{R}) \times [\mathbf{F}_i - 6\pi b_i \eta(\mathbf{r}_i) \dot{\mathbf{r}}_i] = 0, \quad (2.9)$$

where  $\mathbf{R} = (X, Y)$  is a reference point, in this case the hydrodynamic centre of mass  $\mathbf{R} := \sum b_i \mathbf{r}_i / \sum b_i$ . The equations ensure that force- and torque-balance conditions are met.

To understand microbial response to viscosity gradients, the authors performed simulations using a wide range of shapes to draw general conclusions on what response one might expect from a microswimmer based on its geometric properties.

First off is the simple case of a dumbbell microswimmer with a propulsion force pointing along the symmetry axis connecting the two spheres. In this case, no viscous torque is generated and the swimmer does not change its direction of motion.

Next is the case of triangle swimmer, which shows viscotactic behaviour when initialised swimming down the viscosity gradient i.e. the swimmer re-orientes towards the high viscosity region, confirming that viscotaxis can be achieved by swimmers with suitable shapes.

The mechanism at play to cause viscotaxis is shown in Fig. 2.7: the sphere further down the viscosity gradient experiences a higher drag than the other ones, consequently moving slower. As a result, a torque is generated and the swimmer turns up the gradient until torque balance is reached.

The last case analysed by Liebchen *et al.* is that of chiral dumbbell microswimmers with back- or forward-propulsion (note that the propulsion force is allowed to point slightly off-axis to allow for viscous torques to occur, see Fig. 2.8). In this case, results show that both positive and negative viscotaxis can occur, depending on the type of propulsion. Swimmers moving with the forcing sphere ahead spiral up the viscosity gradient, while the opposite occurs for swimmers propelled by the sphere at the back.

These findings highlight the importance of shape in determining how microswimmers navigate through viscosity gradients. However, as previously mentioned, the hydrodynamic signature of the microswimmers can also play a significant role in determining their response to regions of inhomogeneous viscosity.

#### 2.4.2 Viscotaxis by Swimming Gait

A different approach to studying how viscosity gradients can affect microbial motility is to consider the flow fields generated by different swimming gaits, and how those lead to different responses. As we have already touched upon previously in this



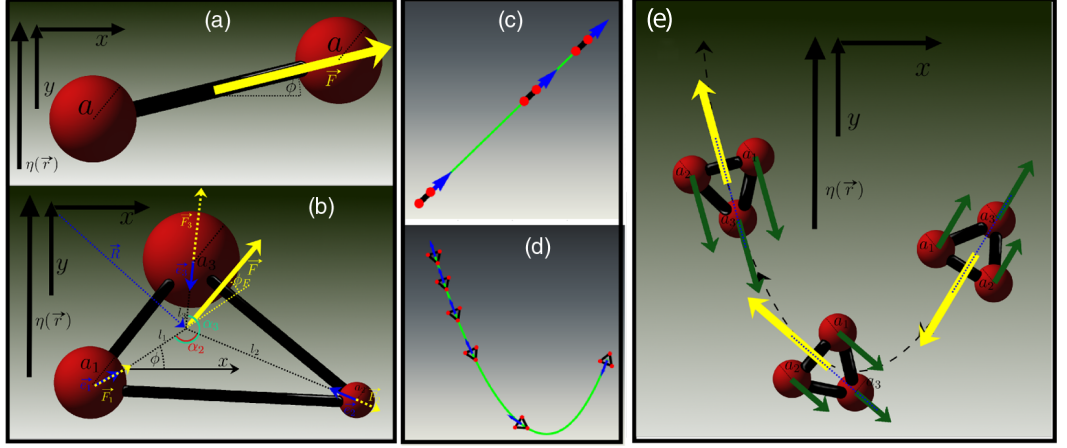


Figure 2.7: Adapted from [41]. Examples of uniaxial (a) and non-uniaxial (b) microswimmers and their typical trajectories in viscosity gradients. Uniaxial swimmers are not affected by the gradient (c) while non-uniaxial swimmers get re-oriented towards the high viscosity region (d). The mechanism behind viscotaxis is detailed in (e), which shows how the force imbalance causes a torque towards high viscosity.

chapter, pusher and puller dipole fields describe remarkably close the real far-flow field generated by the biological microswimmers of interest in this thesis, such as *Chlamydomonas reinhardtii* (puller), bacteria and sperm (both pushers).

In their work, Datt *et al.* derive exact expressions for the translational and angular velocities of a general squirmer navigating through a viscosity gradient [42]:

$$\mathbf{U} = \mathbf{U}_N - \frac{aB_2}{5}(\mathbf{I} - 3\mathbf{e}\mathbf{e}).\nabla(\eta/\eta_0), \quad (2.10)$$

$$\mathbf{\Omega} = -\frac{1}{2}\mathbf{U}_N \times \nabla(\eta/\eta_0), \quad (2.11)$$

where  $\mathbf{U}_N = \frac{2B_1}{3}$  is the velocity of the microswimmer in a fluid of homogeneous viscosity and the  $B_i$  values are known as squirming modes, and determine the properties of the flow field generated by the microswimmer (i.e.  $B_1 < 0$  for pushers and  $B_1 > 0$  for pullers).

From the equations, it appears clear that microswimmers will only be affected by the gradient if they are not swimming parallel to it. In fact, in the event that  $\mathbf{e} \parallel \nabla\eta$  the cross product in eq. 2.11 will be equal to zero and no rotation will occur.

A further consequence of the effect the viscosity gradient has on the swimmer can be inferred from eq. 2.10. Depending on the type of swimmer (i.e. the sign of the squirmer parameters), the particles will either increase or decrease their velocity when swimming up the gradient.

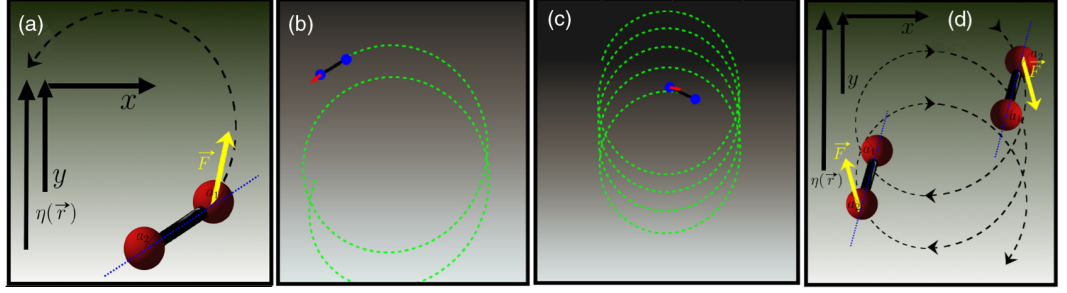


Figure 2.8: Adapted from [41]. Both negative and positive viscotaxis can be achieved by chiral microswimmers. Front driven (a, b) microswimmers exhibit positive viscotaxis, while back driven microswimmers (c, d) exhibit the opposite effect.

An alternative explanation can be given by thinking about how propulsion is achieved for pushers and pullers. For example, pushers will swim fast when navigating down the gradient because they will be generating thrust at their back, where the fluid is more viscous. On the contrary, pullers will be swimming more slowly in a similar situation because thrust will be generated by pulling on the less viscous fluid ahead of them. The situation will obviously be reversed should the swimmers be navigating up the gradient.

Interestingly, Datt *et al.* find that all types of squirmers will eventually swim down the gradient (Fig. 2.9), regardless of their propulsion mechanism. They find the differences to depend on the second squirmer parameter  $B_2$ , which effectively captures the properties of the flow field near the equator of the cell i.e. whether fluid gets pushed out or pulled in.

While all types of swimmers will eventually swim down the gradient, they will do so in different amounts of time. Starting from an orientation perpendicular to the gradient, pullers will be the fastest to re-orient and start swimming towards low viscosity, whereas pushers will be the slowest.

As the authors highlight, these results suggests that (Newtonian) viscosity gradients could potentially be used to sort swimmers depending on their characteristics, similarly to what has already been shown for non-Newtonian fluids [44]. Lastly, it is important to note that the authors do not consider any changes the viscosity could cause to the swimming gait of the swimmers, which - as mentioned in the previous sections - is not strictly correct in an experimental setting. Nevertheless, the models can provide an important framework to interpret the results which will be showed in Chapters 4 and 5.

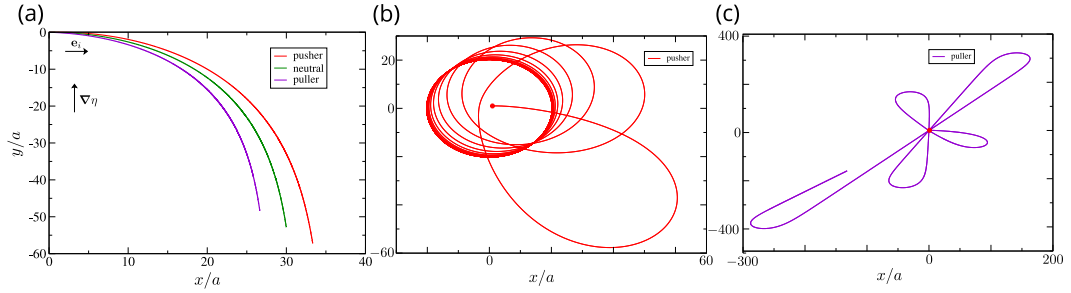


Figure 2.9: a) trajectories of squirmers moving with a starting orientation orthogonal to that of the gradient, all swim towards lower viscosity eventually. (b,c) Trajectories of pusher (b) and puller (c) squirmers navigating in a radially increasing viscosity gradient (the red dot indicates the starting point). Adapted from [42].

## 2.5 Microswimmers in Complex Environments

In the previous sections we have discussed how changing the properties of the fluid surrounding a microorganisms can affect its motility. This however is not the only way in which it is possible to influence microbial motility. In fact, so far we have only discussed the properties of microorganisms swimming in “free space” i.e. far away from any walls or obstacles, but that is hardly the case in nature.

Studying how microswimmers interact with complex geometries is important not only to understand many natural phenomena (it is quite common for organisms to swim near walls, or in complex passageways such as the female reproductive tract) but also to develop biomedical and bioengineering applications [13].

For example, understanding how algae or bacteria interact with obstacles such as pillars could be used to develop smart materials to prevent biofouling, or obstacles could be designed to accumulate sperm cells in specific regions and improve current sorting methods for IVF treatments [12].

In this section we will first cover how different microswimmers interact with plain walls to then move on to how microbial motility is affected by the presence of obstacles.

### 2.5.1 Microswimmer Interaction with Plain Walls

We can study microswimmer interaction with objects by starting from the simplest possible case, i.e. the interaction between a swimmer and a planar wall. Though many interactions can take place when this occurs (electrostatic, depletion etc.), it has now been firmly established that the two interactions playing the biggest role by far in this case are steric and hydrodynamic ones [13].

The study of swimmer interactions with planar walls dates as back as 1963, when Lord Rothschild discovered that swimming bull sperm cells would concentrate on surfaces, as opposed to their dead counterparts. The lack of dead cells accumulating at the walls clearly indicated that the effect was caused by the cells swimming and not by any other “passive” interaction [45].

Since then many years have passed and numerous studies on the subject have been published, revealing that similar phenomena can be observed for a wide range of microswimmers, including sperm cells from different species (bull, sea-urchin) or bacteria such as *E. coli* [21].

The effect of steric interactions on microswimmer behaviour near walls is quite simple to visualise: microswimmers navigating an environment will inevitably reach its walls at some point. Depending on the properties of the swimmer, there will be thermal noise associated with its orientation and motion, which determines how long it will take it to re-orient once the wall is reached. Until then, the microswimmer will continue to swim against the wall, thus leading to an accumulation of cells on it.

While steric interactions allow us to make qualitatively correct predictions regarding microswimmer behaviour near walls, hydrodynamics is essential to fully describe these type of phenomena. In fact, in the close contact regime near-field hydrodynamics and contact interactions determine collision and re-orientation dynamics.

To show how important contact interactions are, we can compare how two strains of *Chlamydomonas reinhardtii* algae behave once they reach a flat wall [21].

First we start by wild-type *Chlamydomonas reinhardtii* (CC125), which swims in a breaststroke manner (i.e. it has flagella ahead of its body): as CR approaches the wall, its flagella probe the surface while simultaneously generating torque to turn the cell away from it.

Next, we observe how CR strain CC2679 behaves near the wall. CC2679 is a strain of CR which has been designed to behave as a “pusher” (i.e. its flagella beat behind the body in a corkscrew like manner, similarly to bacteria). In this case, CR swims along the surface until random re-orientations don’t cause it to move away from it. Due to this effects, CC125 spends on average 0.5 s near a wall, whereas CC2679 takes 10 s to swim away from the wall. It should then be clear that ciliary interactions play an important role in determining microswimmer behaviour near walls.

As we’ll see in later chapters, we can take advantage of knowing about microswimmer properties to design walls which are specifically designed to orient microorganisms towards certain directions or away from walls of our observation chamber.

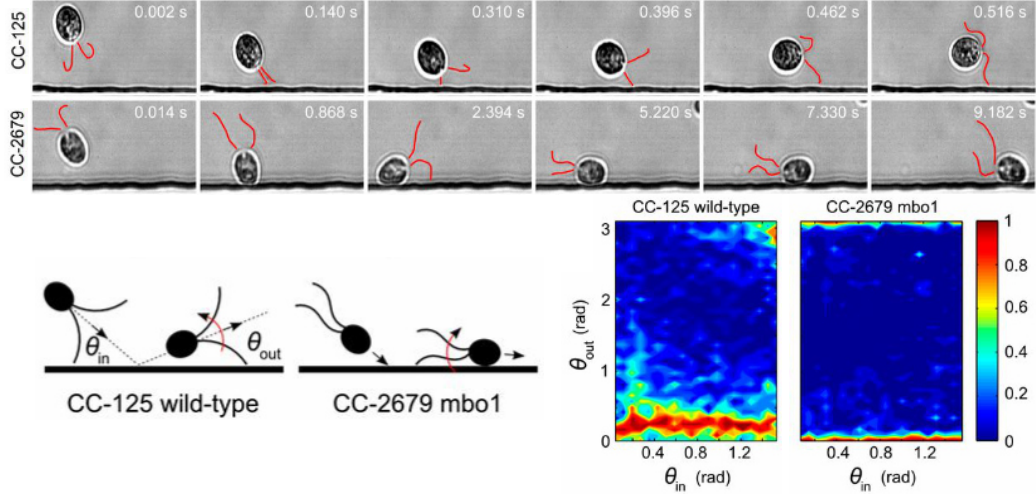


Figure 2.10: Top row: wild-type (CC125) and “pusher” strain (CC2679) of *Chlamydomonas reinhardtii* approaching a planar wall. The puller version of the swimmer quickly re-orient away from the wall, the pusher one continues swimming against it. Bottom row: schematic of the different behaviours at the wall (right) and probability distributions of scattering angle  $\theta_{\text{out}}$  for a given  $\theta_{\text{in}}$ , showing quite clearly the independence of the two parameters. Adapted from Kantsler *et al.* [21].

### 2.5.2 Microbial Motion Rectification

As seen in the previous section, “pusher” microswimmers such as bacteria or sperm tend to align themselves along boundaries and follow them. With the advent of microfluidics and the possibility to carefully design environments at the microscale, research efforts have been focussed on taking advantage of this property to develop devices aimed at concentrating microswimmers in specific regions or sort them based on motility or shape.

The first experimental work on this type of problem came from Galajda *et al.*, who showed that “V-shaped” obstacles can be used to successfully rectify bacterial motion and concentrate *E. coli* in a specific region of a microfluidic device [46].

The device works in a simple way: a main microfluidics chamber is divided in sections by a series of obstacles (Fig. 2.11). The obstacles (V-shaped) are designed so that bacteria can swim successfully from one section to the other if they are moving in one direction, but get re-oriented if they swim in the opposite one. Over time, this leads to bacteria accumulating in the last section of the device (i.e. the section towards which the inside part of the V points towards).

Since then, numerous efforts have been made to study these types of system further both using experimental and simulation tools.

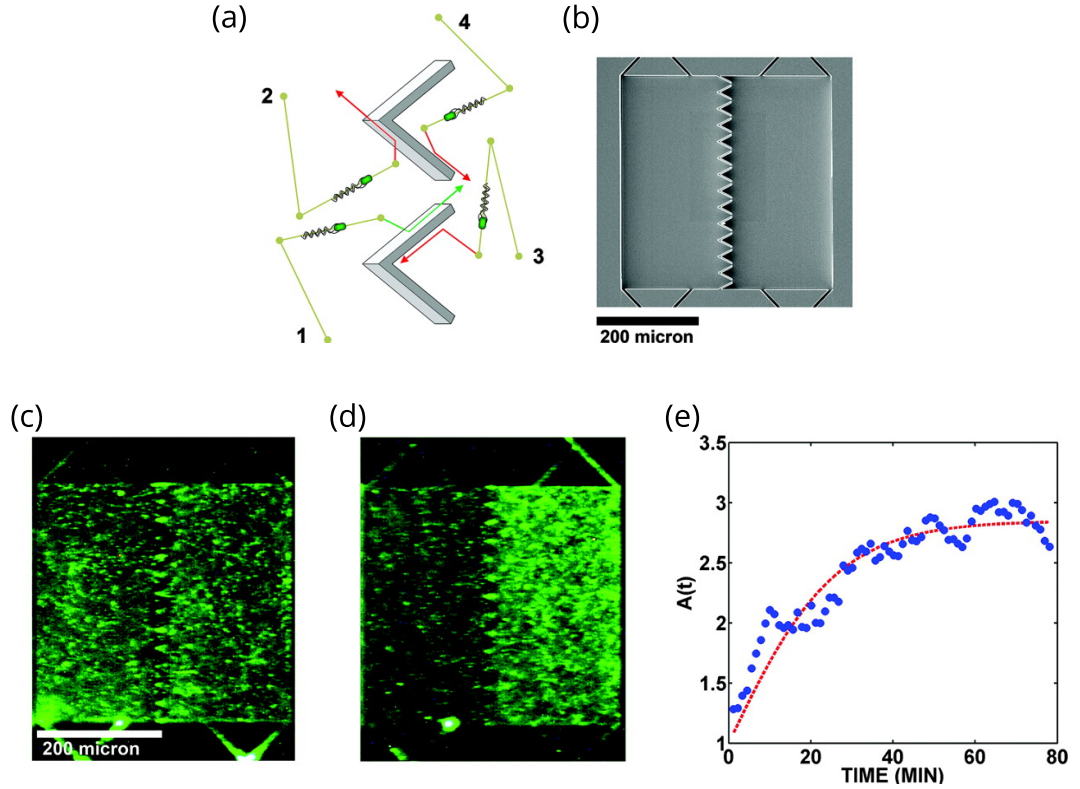


Figure 2.11: (a-b) The design of the original microfluidic device by Galadja *et al.*. The initial concentration of an experiment (c) compared to the final concentration of bacteria in the same device (d) after 80 minutes. (e) The concentration curve for bacteria in the right chamber. Adapted from [46].

For example, Tailleur and Cates showed the efficiency of rectification devices is determined by the ratio at which swimmers encounter the obstacles and the time it takes for them to be rectified by the obstacles [47], while Mijalkov and Volpe performed simulations to show it is possible to design obstacles to separate particles based on their chirality (see Fig. 2.12) [48].

As these types of devices rely on microswimmers navigating the environments, obstacles can also be used to separate microswimmers based on their motility: if a microswimmer is not moving, it will not be re-oriented by the ratchets and not swim towards the final section of a device. For this reason, many research groups have started developing microfluidic devices with the aim of separating motile sperm cells from non-motile ones in an aim to improve in vitro fertilization (IVF) results (see Fig. 2.13) [12, 49].

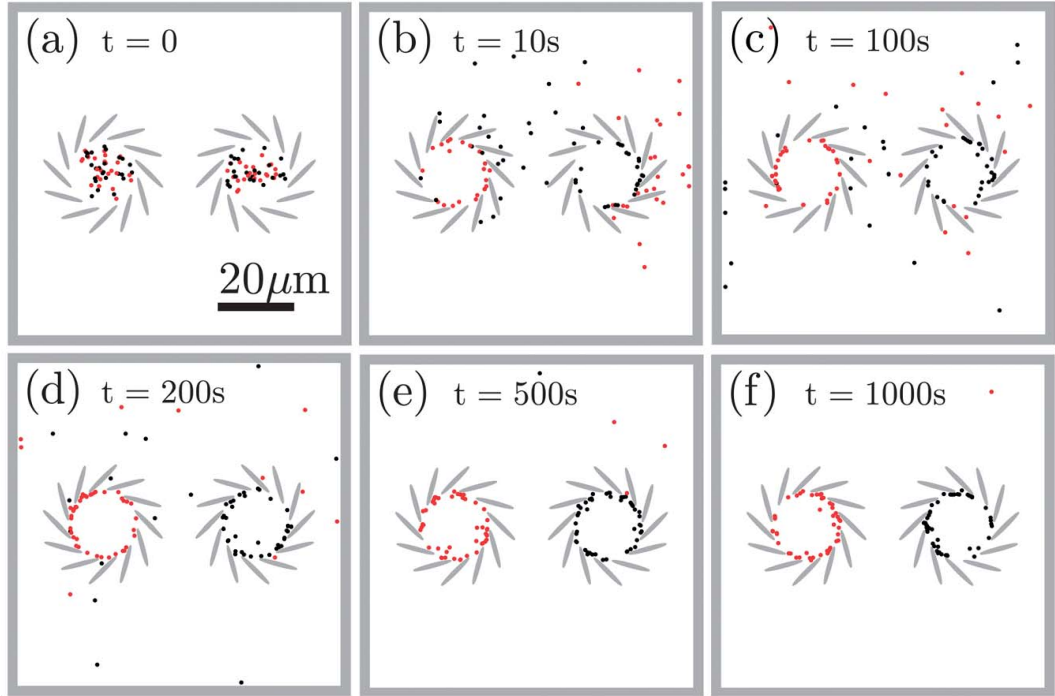


Figure 2.12: Particles separated based on their chirality. Red particles swim in clockwise circles, black particles swim in anticlockwise circles. Adapted from [48].

## 2.6 Microswimmers in Temperature Gradients

So far, we have touched upon external stimuli which cause “passive” responses from the microswimmers. In this last section, I will briefly go over an active type of microbial response: thermotaxis.

As the name suggests, thermotaxis is the response a microswimmer has to a temperature gradient. Similar to viscosity gradients, temperature gradients are ubiquitous in nature and are suspected to play a key role in many important natural phenomena: for example, temperature differences are present in the oviduct and are thought to be one of the sperm guidances methods through which fertilization is achieved [50]. Thermotaxis has also been shown to be important for *Chlamydomonas reinhardtii* algae and *E. coli* bacteria, both of whom can navigate temperature gradients to find the regions which allow them to grow optimally [51, 52].

As Chapter 7 deals with bull sperm response to increased temperature and temperature gradients, in the next section I will outline what has already been found about sperm thermotaxis.



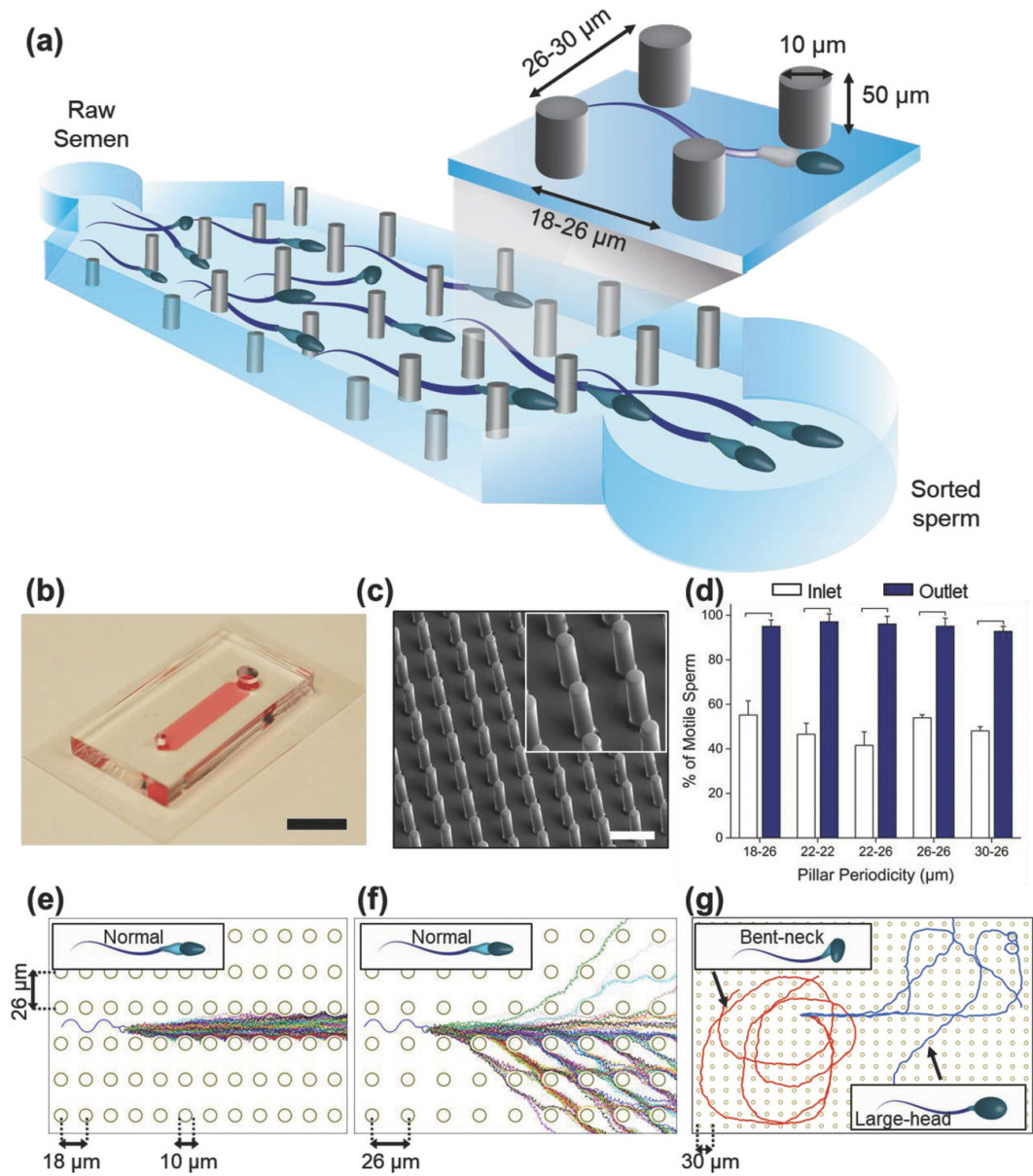


Figure 2.13: Microfluidic device designed to sort sperm cells based on their motility. The device uses pillar arrays to guide sperm cells towards an outlet, ensuring all the motile cells are there while the non-motile cells remain in the inlet region. It also ensures sperm cells with defects (bent-neck or large-head) remain trapped by the pillar array (g). From ref. [12].

### 2.6.1 Sperm Thermotaxis

Before discussing the currently available literature for mammalian sperm thermotaxis, it is important to re-iterate sperm cells from different species might exhibit



different responses to the same stimuli. Nevertheless, it is possible to draw some common properties to sperm response to temperature gradients across species - mainly the accumulation effects towards higher temperatures [4, 50].

While no data is available for humans, temperature differences have been found in the oviduct of rabbits and pigs between the fertilization site and the sperm storage site [53, 54]. However, the presence of temperature gradients does not on its own confirm thermotaxis in sperm cells.

To delve deeper into the matter, recent experimental studies have been performed to understand a) if sperm indeed undergoes positive thermotaxis in temperature gradients; b) what temperature differences can be “sensed” by sperm, if such an effect exists.

First experiments to confirm human sperm thermotaxis were performed by Bahat *et al.*, who developed a simple thermotaxis assay which would allow them to count the number of migrated cells in a linear temperature gradient [9]. While the assay did not permit the authors to track the sperm as it navigated the temperature gradients (see Fig. 2.14) but only to evaluate the percentage of migrated cells in a linear gradient (33 to 37 °C), results were still useful in confirming that a small percentage of human sperm (5-9%) does indeed concentrate in higher temperature regions. Further experiments by the same group also revealed that human sperm is able to sense extremely shallow temperature gradients (0.014 °C/mm) as well as other important findings, such as the tendency of sperm to concentrate in warmer regions even if those are above the physiological temperature range and the ability to respond to negative gradients and not only positive ones.

Similar experiments were performed by Mondal *et al.* to investigate whether bull sperm also responds to temperature gradients in a similar way [55].

Also in this case, results showed quite clearly that between ~10% of the sperm cells in a sample are thermotactic and concentrate in higher temperature regions.

These findings suggest that thermotaxis is one of the methods (combined with rheotaxis, chemotaxis and boundary following effects) by which sperm cells navigate towards the egg during fertilization.

**a**



**b**

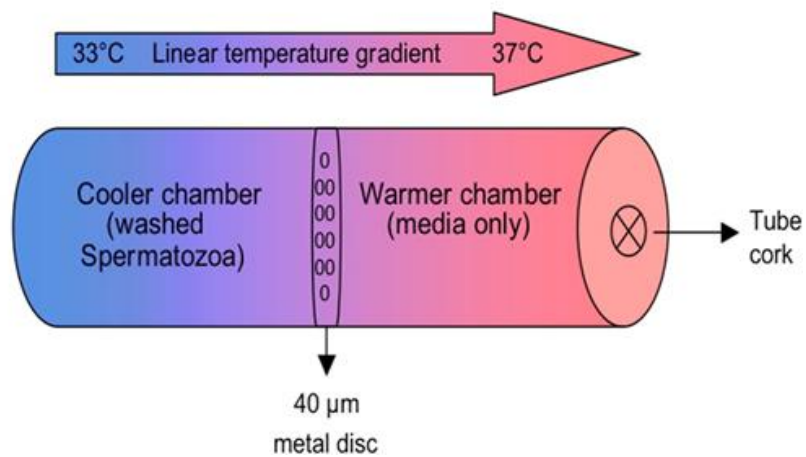


Figure 2.14: Example of a thermotaxis assay device from one of the available studies in the literature. As it appears clear from the figure, the device does not allow live imaging of the sperm as they navigate through the gradient. From [9].

## Chapter 3

# Methodology

The systematic study of microbial motility would not be possible without the use of microfluidics devices. As the name suggests, microfluidics devices enable users to manipulate small volumes of fluid in a precise and controlled way [56]. For this reason, and due to the low cost and effort required to make them, microfluidics have become the golden standard when it comes to developing experiments aimed at understanding precisely how microswimmers behave under specific conditions.

Coupling microfluidics with optical microscopy, modern digital imaging and data analysis has opened a wealth of new possibilities in the field of soft active matter, allowing researchers to perform experiments which would not be possible otherwise [10].

In this chapter, I will first give a detailed description of the design and manufacturing process of microfluidics devices and will then discuss the microscopy, data analysis and culturing techniques used to obtain the results outlined in the next parts of the thesis.

### 3.1 Microfluidics Device Preparation

The first step towards microfluidics experimentation is device design. All device designs used in this thesis were drawn using the commercially available computer-aided design (CAD) software AUTOCAD (Autodesk, Inc.) and the opensource software Inkscape (<https://inkscape.org/>). The CAD designs were used to produce film photomasks of the devices, which were ordered from *Microlithography Services Ltd.*

The film photomask is essential to transfer the device design on to the mould which is then used to produce the devices.

The mould is produced through a process known as *optical photolithography* (steps 1-5 in Fig. 3.1) which is now outlined:

- A layer of photoresist (SU-8, Microchem) is deposited on a Silicon wafer through spin coating to achieve the desired device thickness, which can range from a few  $\mu\text{m}$  to almost 1mm (step 1-2);
- The photomask is then placed on top of the spin-coated wafer and they are exposed to UV light. SU-8 is a negative photoresist: this means that the parts exposed to UV light become cross-linked, while the others stay soluble (step 3-4);
- After exposure, the wafer is placed in a solvent bath. Here, the wafer is developed and all the non-exposed parts of the SU-8 layer get washed away. The wafer is now ready to be used as a mould for microfluidics devices (step 5).

After the pattern has been transferred on the silicon wafer, it can in theory be used as a mould for the devices indefinitely, as long as it is kept dust and damage free. Devices are then produced from the mould through the process of *soft lithography* (steps 6-7 in Fig. 3.1), in which Polydimethylsiloxane (PDMS, Dow Sylgard 184) - a transparent silicone polymer - is poured on the mould before placing it on a hot plate set at 80° for 3-4 hours to cure and solidify. After the PDMS has fully cured, it is then possible to cut it from the mould, which will have left the device geometry stamped on the resin.

Lastly, in order to perform experiments it is necessary to fully seal the microfluidic chamber by bonding the PDMS to a glass coverslip. This is achieved through plasma oxydation (or cleaning).

The PDMS and the coverslip are both placed inside a chamber in which an Oxygen plasma is generated. While in the chamber, the ionized particles of the plasma interact with the surfaces of the objects inside, removing organic contamination and modifying their surface properties. In particular, exposing a PDMS surface to Oxygen plasma exposes silanol groups on it (-OH). This will lead to the formation of covalent bonds (SI - O - SI) when the PDMS is placed on the glass surface. The bonds form a practically unbreakable seal between the PDMS and glass slide, thus allowing us to have water tight devices.

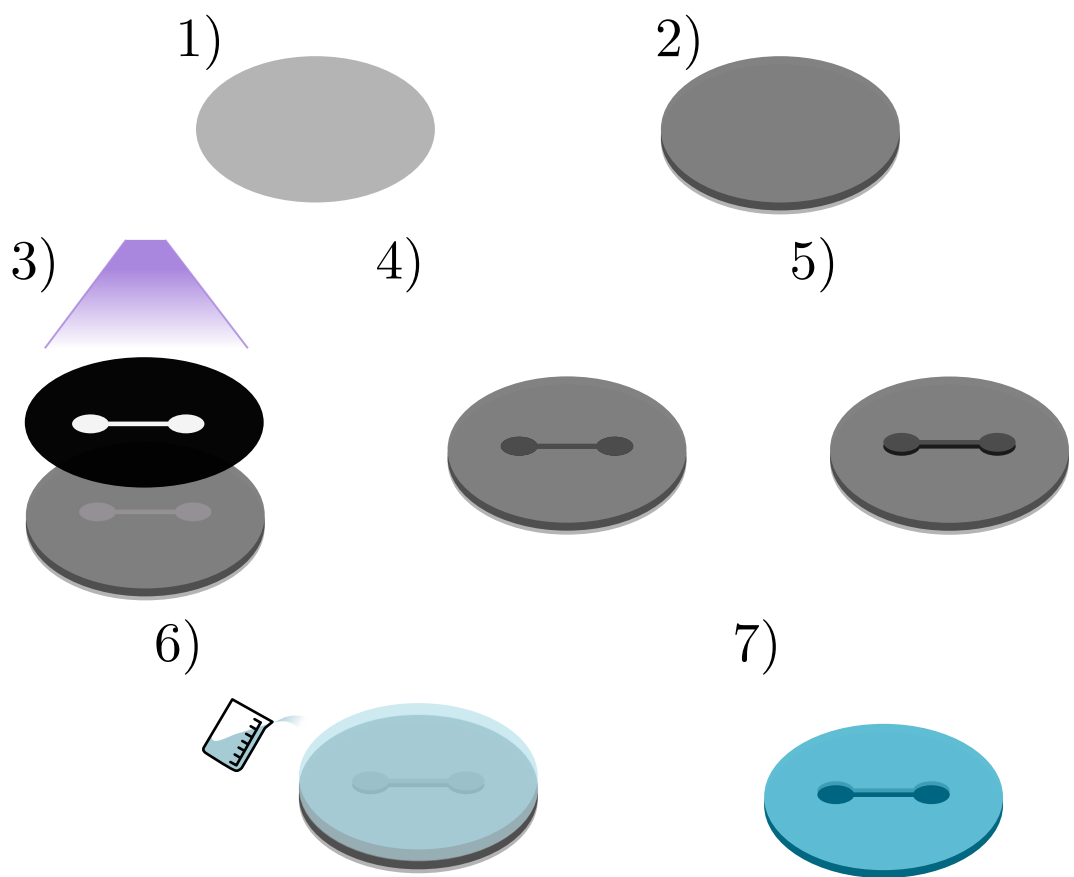


Figure 3.1: A schematic of the optical photolithography (1-5) and soft lithography (6-7) processes followed to make microfluidics devices.

## 3.2 Microscopy and Image Processing Techniques

An inverted Nikon Eclipse was used to perform microscopy during the PhD. Images were acquired using various CCD and CMOS digital cameras connected to a Desktop Computer (see individual chapters for further details on the cameras and acquisition parameters).

In order to achieve the best imaging results for each experiment, various optical microscopy techniques had to be used depending on the specific circumstance:

- **Brightfield Microscopy** - the simplest optical microscopy technique. Sample illumination is achieved with transmitted light and contrast is determined by light attenuation, hence it can be poor when working with biological microorganisms (Fig. 3.2a);
- **Phase Contrast Microscopy** - a method which creates better contrast in the image by separating background and foreground through a series of phase-shift rings which convert phase shifts into brightness changes (Fig. 3.2b);
- **Darkfield Microscopy** - a method through which only light diffracted by the specimen is collected by the objective (Fig. 3.2c);
- **Fluorescence Microscopy** - a microscopy technique in which the sample is illuminated with light of a specific wavelength which causes fluorophores to emit light of a different wavelength. After that, a filter is used to only collect light emitted from the sample (Fig. 3.2d).

### 3.2.1 Particle Tracking

After acquiring videos of microswimmers moving inside the microfluidics devices, it was necessary to extract their positions in each of the video frames and connect them to form the trajectories which would then be analysed. This was achieved through custom MATLAB (Mathworks) and ImageJ (<https://imagej.net/>) scripts developed with the requirements and needs of each dataset in mind.

While not all experiments were analysed using the same algorithm, all scripts used to track particles from videos followed the same key steps and principles (Fig. 3.3), which I will now outline:

1. In order to remove any stationary objects and intensity gradients in the images, a background was calculated as the median of all the images in the sequence and subtracted from each frame;

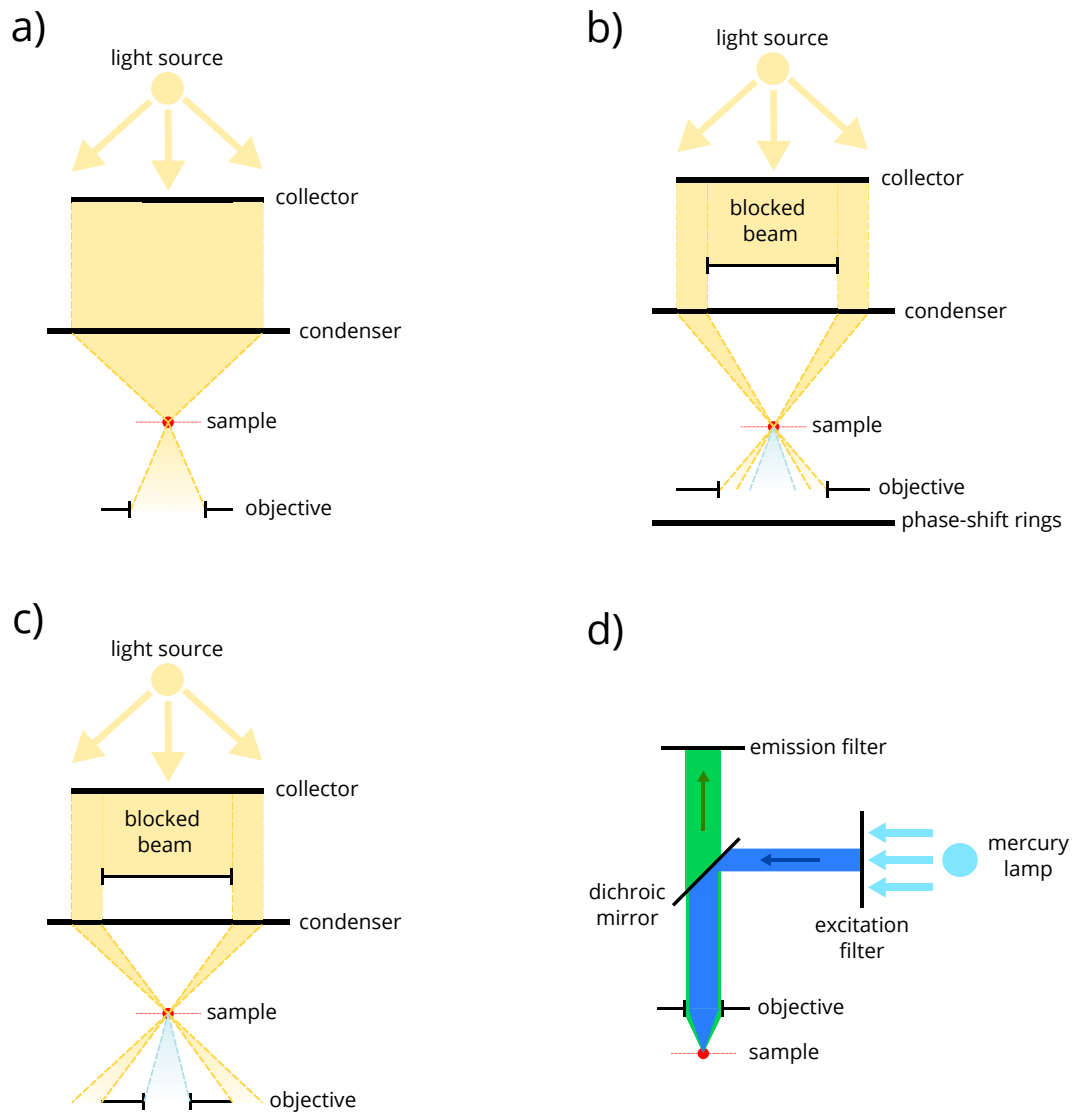


Figure 3.2: Schematics depicting the path light follows in (a) brightfield microscopy, (b) phase contrast microscopy, (c) dark field microscopy and (d) fluorescence microscopy.

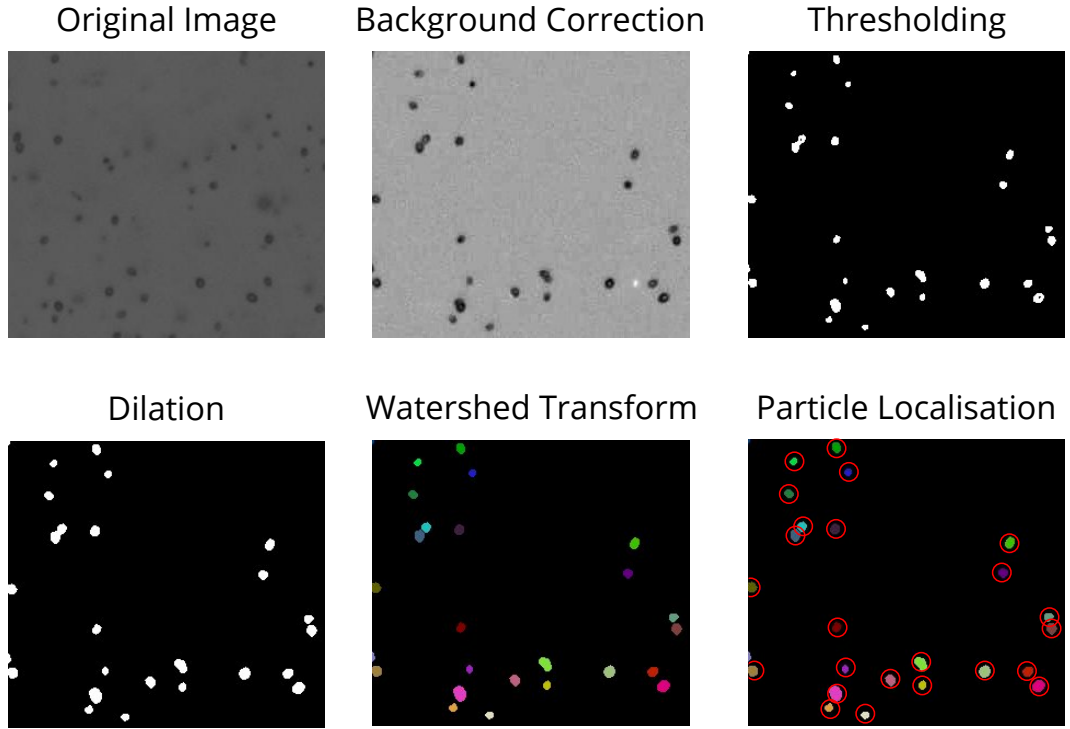


Figure 3.3: An example of the image processing algorithms used to locate and extract the position of *Chlamydomonas reinhardtii* algae from image sequences.

2. In order to identify the swimmers in each frame, a threshold algorithm (i.e. Otsu Thresholding) was applied to each background-corrected image to generate a binary one;
3. Further morphological operations were performed on the binary images to remove any outlier pixels not belonging to the particles (or to clearly separate the sperm head and tail - see Chapter. 5);
4. Using the “cleaned” binary images, the position of all the particles in each frame was stored in an array;

After finding the position of all the particles in the video frames, it was necessary to link them to construct trajectories. The algorithms used to perform this task all followed a similar structure:

1. Each particle found in the first frame of the sequence is assigned a unique “trajectory ID”;
2. Starting from the second frame, the cartesian distance between each particle and all the particles in the previous frame is calculated;



3. If the distance between two particles is smaller than a user-defined radius, the particle in the second frame is assigned the same trajectory ID as the one in the previous frame;
4. If none of the particles in frame one is close enough to a particle in the second frame, the particle is assigned a new trajectory ID;
5. The process is repeated over all the frames.

### 3.3 Microbiology Techniques

#### 3.3.1 *Chlamydomonas reinhardtii*

Agar slants of wild-type (wt, CC125) and short-flagella (slf, CC2347) mutants of *Chlamydomonas reinhardtii* were obtained from the Chlamydomonas Resource Centre ([www.chlamycollection.org](http://www.chlamycollection.org)). The slants were then used to inoculate liquid cultures in tris-acetate-phosphate (TAP) medium [57].

The liquid cultures were grown axenically in a 20°C diurnal chamber set on a 16/8 hour day/night cycle on a rotary shaker set at ~100 rpm.

The cultures were kept at a population density of  $10^5$  cells/ml, so that experiments could be performed with algae in their exponential growth stage.

#### 3.3.2 Bacteria

Cultures of *E. coli* HCB1773<sup>1</sup> strain were streaked from a frozen culture onto 1.5% agar plates containing Tryptone Broth (Sigma Aldrich) and 100 µg/mL Ampicillin (Sigma Aldrich) and grown overnight in an incubator. Individual colonies were then picked from the plate and inoculated in 20mL of Tryptone Broth with 100 µg/mL Ampicillin and 0.1 mM isopropyl β-D-1-thiogalactopyranoside (IPTG, Sigma Aldrich). The liquid culture was then placed on a rotating shaker (100rpm) overnight in the incubator.

Lastly, the culture was diluted 1:100 in fresh Tryptone Broth and placed in the incubator again for 4 hours before performing experiments. This ensured that experiments could be performed using bacteria during their mid-exponential growth phase.

---

<sup>1</sup>A gift from Howard Berg. Ampicillin resistant; Smooth swimmer; Filaments stay bundled; eYFP cloned into SacI/xbal sites; Vector is pTrc99; Replication origin is pBR; IPTG inducible; Can be labelled with maleimide dyes.

### 3.3.3 Sperm

Frozen ram and bull sperm samples were acquired from commercial partners and stored in a liquid nitrogen ( $-196^{\circ}\text{C}$ ) dewar before use.

Samples were thawed by placing them in a  $37^{\circ}\text{C}$  water bath for 30 seconds. Depending on the nature of the experiment performed, the sample was either washed or put through a microfluidic sorting device immediately after thawing.

Sperm washing was performed by placing the sample (200-400  $\mu\text{m}$ ) in an eppendorf tube and diluting it using Tryladyl (Minitube) to achieve a 1.5mL final volume. After that, the sperm was centrifuged at 6000rpm (5.5  $g$ ) for 12 mins (Eppendorf MiniSpin). Lastly, the supernatant was removed and the pellet resuspended in 300 $\mu\text{L}$  of fresh media.

Sperm sorting was performed through a microfluidics sorting device resembling the one discussed in Chapter 6 (Cytoswim). Through the device, it was possible to sort sperm cells so that - at the end -  $\sim 50\mu\text{L}$  of highly motile sample could be extracted. It is important to note that while sperm washing is significantly less effective in removing non-motile sperm from the sample, it allows us to obtain a large sample volume to work with. That was particularly useful when performing experiments such as the one outlined in Chapter 5, where it is necessary to run a syringe pump for 3-5 minutes to ensure the device is correctly set up.

On the other hand, experiments such as the ones shown in Chapter 7 required a small volume of sample ( $\leq 10\mu\text{m}$ ) to be set up, but relied on being performed with high motility cells thus requiring us to use the device designed by Cytoswim.

## Chapter 4

# *Chlamydomonas reinhardtii* behaviour at sharp viscosity interfaces

This chapter is based on work which has been published in a peer-reviewed journal during the PhD:

Coppola, S., Kantsler, V. *Green algae scatter off sharp viscosity gradients*. **Sci Rep** 11, 399 (2021).

### 4.1 Introduction

As shown in the previous chapter, in nature micro-organisms often have to respond to external stimuli and changes in their surroundings when navigating through an environment. These stimuli can be of various sorts, from chemical gradients [58] to external flows [6] or even topological gradients [59].

Another change in the environment that is being navigated by the micro-organisms can be the viscosity of the medium in which they are swimming. It is indeed quite common to find a variety of natural environments which have spatially inhomogeneous viscosities, ranging from sedimentation profiles and biofilms to the female reproductive tract [31, 60].

Recently, theoretical frameworks have been developed to predict the behaviour of a microswimmer in a viscosity gradient. For example Liebchen *et al.* [41] showed how certain body shapes can lead to negative viscotaxis (i.e. moving away from a high viscosity region) due to a systematic imbalance of the viscous forces acting on the microswimmer. Similarly, Datt and Elfring [42] demonstrated that the response

of a microswimmer to a viscosity gradient depends on its flow field by developing a theoretical model based on hydrodynamics.

In order to carry out an experimental investigation on the matter we perform experiments using microfluidic devices, which have proven over recent years to be the standard tool when performing systematic research on microbial motility in inhomogeneous environments [58, 61].

We perform our research using a device which generates a sharp viscosity gradient (i.e. two adjacent regions of significantly different viscosity) which we believe can help identify whether there is a major effect to be seen and investigated further (Fig.6.1). We also highlight that the terms “sharp gradient” and “interface” will be used interchangeably in the chapter.

We use *Chlamydomonas reinhardtii* (CR), a biflagellate  $10\text{ }\mu\text{m}$  “puller” microswimmer which achieves locomotion through breaststroke-like beating and has been thoroughly studied and accepted as a model biological microswimmer in recent years [22]. Qin *et al.* [33] first showed experimentally that the motility of CR is strongly influenced by the viscosity of the environment which they inhabit. In fact, the motility of microorganisms swimming in viscous environments is determined by a complex interplay between the swimmers’ kinematics and material properties as well as the properties of their surrounding environment. Such interplay can include aspects such as the increased drag on the flagella, their rigidity as well as any mechanosensory response from the microswimmers i.e. passive and active responses to the environment [31].

Viscous environments can therefore have profound effects on the propulsion speed and beating frequency of the algae. However, this study by Qin *et al.* [33] is only concerned with environments of homogeneous viscosity, and only explores the effects of viscous environments up to  $\sim 10$  times more viscous than water.

Viscosity has also been predicted to play a role in the flagellar dynamics of CR by Klindt *et al.* [62], who have showed that flagellar synchronization is dependent on the viscosity of the medium in which CR is swimming. In fact, while free swimming CR usually display in-phase synchronization of their flagella to achieve their breaststroke-like swimming, it is also possible for the flagella to lock in an anti-phase synchronization [63]. In such cases, the flagella motion resembles that of freestyle swimming and is characterized by straighter trajectories, as opposed to the run-and-tumble motion which results from breaststroke-like swimming [23].

In this chapter we observe how wild-type (wt) and short-flagella (sfl) CR respond to viscous environments by diluting Methylcellulose (MC) in water (see Methodology section). This allows us to produce media with dynamic viscosity  $\eta_{\text{MC}}$  up to  $\sim 60$

times that of water  $\eta_0 \approx 1$  cP (Fig. 6.1).

We choose to investigate the two strains as there have been experimental reports which suggest the effects of increasing viscosity could change depending on the flagellar length of the algae [35]. We analyse how the velocity and angular diffusion of the algae change as the viscosity of the medium is increased, expanding previously published experimental results and predictions made on the matter [33].

We also perform an analysis of single cell trajectories for CR approaching the interface between the low and high viscosity region, showing that algae can scatter off the interface if they approach it from the low viscosity region at a sufficiently small angle - therefore confirming previous suggestions that “puller” microswimmers could exhibit viscophobicity due to torque imbalance [41, 42].

Finally, we explore how the combination of these different phenomena affects the concentration profile of CR in the channel. Surprisingly, we find that CR either concentrate in the low viscosity region (i.e. where they swim faster) or nowhere at all, maintaining a uniform concentration profile. This highlights that the velocity distribution in the chamber is not the main factor dominating how CR diffuse in the chamber, but rather that the results are a combination of all the effects previously mentioned.

## 4.2 Methods

Algae cultures were grown as described in the methodology chapter, ensuring experiments were performed during the mid-exponential phase of growth.

PDMS Y-junction microfluidic devices ( $\sim 20$   $\mu\text{m}$  high, see inset Fig. 6.1) were manufactured via standard soft lithography techniques as outlined in Chapter 3.

The device was used to generate two bands of equal width but significantly different viscosity through the use of two syringe pumps equipped with 100  $\mu\text{l}$  gastight syringes (Hamilton). Two syringe pumps (KD Scientific) were used to balance the flow rates depending on the viscosity ratio of the two fluids employed in order to generate bands of equal size.

High viscosity media were prepared by dissolving different concentrations (0.15%, 0.30%, 0.50% and 0.75%) of high-grade Methylcellulose (MC) (Sigma Aldrich, M0512) in DI water and an Ubbelohde viscometer was used to measure the dynamic viscosity of the different solutions (Fig. 6.1). The viscosity measurements were found to be in agreement with previously published results [64], which also show that MC behaves as a Newtonian fluid for concentrations below 1%.

To obtain equal concentrations of CR in both media used in the experiments,

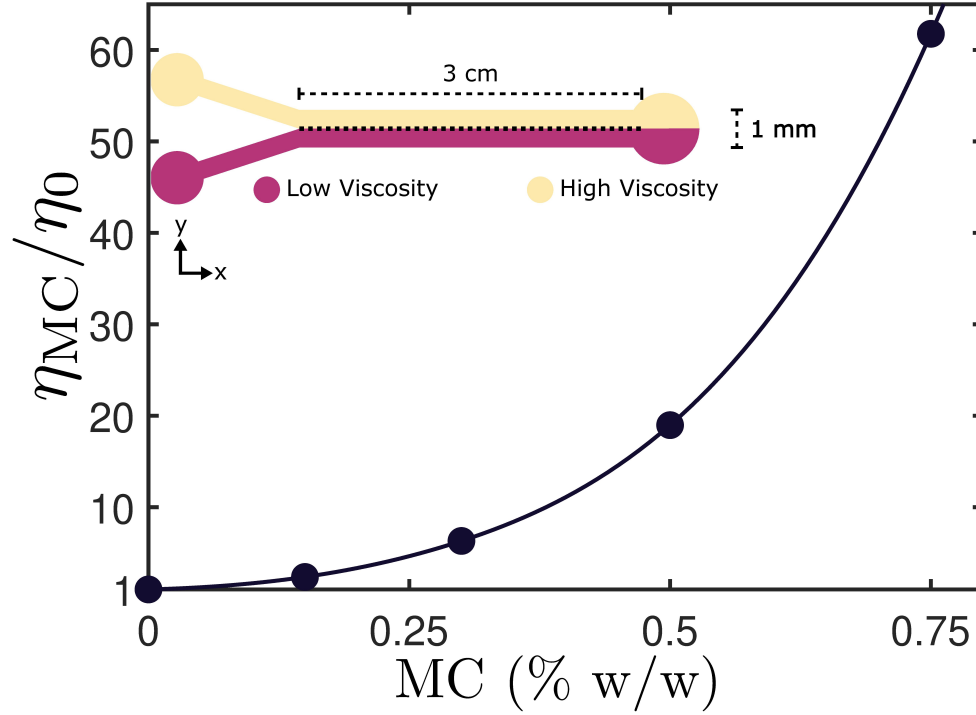


Figure 4.1: Dynamic viscosity measurements for the various solutions of DI Water and methylcellulose which were used as high viscosity media. The circles indicate the concentrations used during the experiments: 0.15%, 0.30%, 0.50% and 0.75%. In the inset, the geometry of the microfluidic device used to perform the experiment (inlets on the left, outlet on the right). Through laminar flow and balanced flow rates it is possible to generate two regions of equal width but different media, as highlighted by the different colours. Error bars smaller than marker size.

two 1.5 ml eppendorfs vials were filled with cultures and centrifuged at  $\sim 1.2$ k rpm for 12 minutes. The supernatant was then removed and substituted with DI water (low viscosity medium) and one of the MC solutions (high viscosity medium). The two eppendorfs were then placed on a rotary shaker for 30 minutes to ensure that any deflagellated algae would regrow their flagella before being used to fill the microfluidic device and perform the experiment. The cell concentration at which experiments were performed ( $10^5$  cell/mL) prevents any collective hydrodynamics effects from contributing to the results reported. All experiments were performed at room temperature.

Brightfield microscopy was performed using a Nikon Eclipse TE2000U inverted microscope equipped with a 4x objective (Nikon, NA 0.10). To prevent any phototactic bias in the data, a longpass coloured glass filter (RG715, Thor Labs) was used to

block any wavelength below 715 nm. Image frames (10 fps) were recorded using a 1920x1200 pixel CCD camera (Pointgrey Grasshopper3) and processed through custom MATLAB software to extract microswimmer trajectories and analyse them.

## 4.3 Results and Discussion

### 4.3.1 Velocity Distributions & Motility Characterization

Fig. 4.2a shows how the velocity of CR changes as a function of its position in the device when 0.30% MC ( $6\eta_0$ ) is used to generate the high viscosity region. As expected, the device generates two regions where the velocity of the algae is significantly different. Furthermore, we measure how the swimming velocity distribution  $V(y)$  across the microfluidic device changes as a function of time. This provides a way to indirectly keep track of how stable the gradient is during the experiment, since a smoothing of the gradient is to be expected due to methylcellulose diffusing. We show the interface is the sharpest for the first 100s, and stays so for 1000s - with the gradient diffusing only by about  $50\mu\text{m}$ .

In order to fully understand how different viscosities affect the swimming velocity of wild-type (wt) and short-flagella (sfl) CR, the ratio  $V_0/V_{\text{MC}}$  (where  $V_0$  is the velocity of CR in its regular medium and  $V_{\text{MC}}$  the velocity in the high viscosity medium) is measured for different concentrations of MC in DI water (Fig.4.2b).

The results shown in Fig.4.2 agree with previous findings reported by Qin *et al.* [33] for wt *Chlamydomonas*, which show that the velocity of swimming algae decreases approximately as  $1/\eta$  for viscosity values up to  $\sim 10\eta_0$ . This result, as already highlighted by Qin *et al.* [33], indicates the algae continue swimming with the same thrust despite the increased viscosity of the media.

We expand on these previous findings by measuring the velocity of CR in environments up to  $60\eta_0$ , showing both strains of CR do not decrease their velocity any further for viscosities of  $\sim 30\eta_0$  and higher. Such results suggest that for sufficiently high viscosities ( $> 10\eta_0$ ) CR might change its swimming gait to optimize efficiency, similar to what has been reported for sperm cells swimming in high viscosity environments [31].

Interestingly, we also observe that increasing the viscosity has a larger effect on wt CR than the sfl strain.

To understand this peculiar finding, we refer to the report published by Bottier *et al.* [35], who carried out an in depth investigation of how cilia beating is affected by its length. In particular, the authors investigated how the force required to overcome viscous drag changes as a function of flagellar length. Results showed that the force

required to overcome drag increases with the length of the flagella, while the overall dynein force (i.e. the force moving the flagella) does not. While this experimental investigation only concerns algae swimming in regular viscosity media and a more detailed study would be needed to confirm our suspicion, we believe its results can offer a qualitative explanation for the difference in effect we measure between the two CR strains. To characterize the behaviour and motility of CR in high viscosity

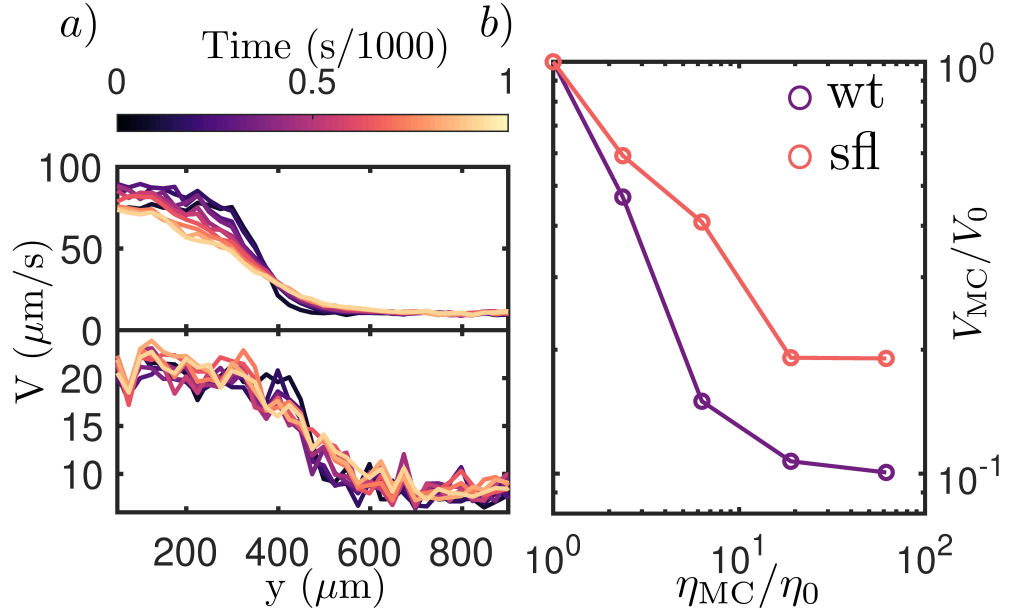


Figure 4.2: a) Swimming velocity of wild-type (top) and short flagella (bottom) *Chlamydomonas reinhardtii* algae as a function of their position in the device in experiments in which 0.30% MC ( $6\eta_0$ ) is used for the high viscosity region between 0 and 1000s after the syringe pump is stopped at the beginning of the experiment (see Fig.1 for a coordinate system reference), showing that the gradient is stable for the time of interest. b) The velocity ratio  $V_{\text{MC}}/V_0$  as a function of the concentration of MC in the high viscosity region.

media, we determine the translational ( $D_{\text{T}}$ ) and rotational ( $D_{\text{R}}$ ) diffusivity of the algae by calculating the mean-squared displacement (MSD) and mean-squared angular displacement (MSAD) from their trajectories.

The MSD is defined as  $\text{MSD}(\Delta t) = \langle |\mathbf{r}(t_0 + \Delta t) - \mathbf{r}(t_0)|^2 \rangle$ . CR exhibit ballistic behaviour at short timescales ( $\text{MSD} \propto \Delta t^2$ ), while at sufficiently long scales their motion can be characterized as diffusive ( $\text{MSD} \propto \Delta t$ ). Therefore, for CR



performing a random walk in two dimensions, it is possible to extract  $D_T$  from  $\text{MSD}(\Delta t) = 4D_T\Delta t$ .

Fig.4.3a shows the  $D_T$  extracted values for wt and sfl CR swimming in environments of increasing viscosity. As expected from the decrease in velocity observed in Fig.4.2, the translational diffusivity of CR also decreases as the viscosity of the surrounding environment is increased.

The MSAD is defined  $\text{MASD}(\Delta t) = \langle |\phi(t_0 + \Delta t) - \phi(t_0)|^2 \rangle$ . In this case, all curves show a diffusive behaviour, making it possible to extract the rotational diffusivity value from  $\text{MASD} = 2D_R\Delta t$ . Fig.4.3b shows the rotational diffusivity of CR decreases when the viscosity of the surrounding medium is increased. This is further highlighted by the typical trajectories (Fig.4.3), in which it is possible to observe that CR swimming at high viscosity do not display any sharp changes in direction, but are rather straight. This contrasts with typical CR trajectories for algae swimming in low viscosity media, which have been observed to display a “run-and-tumble” type of motion. It is possible to explain the decrease in angular diffusivity and the

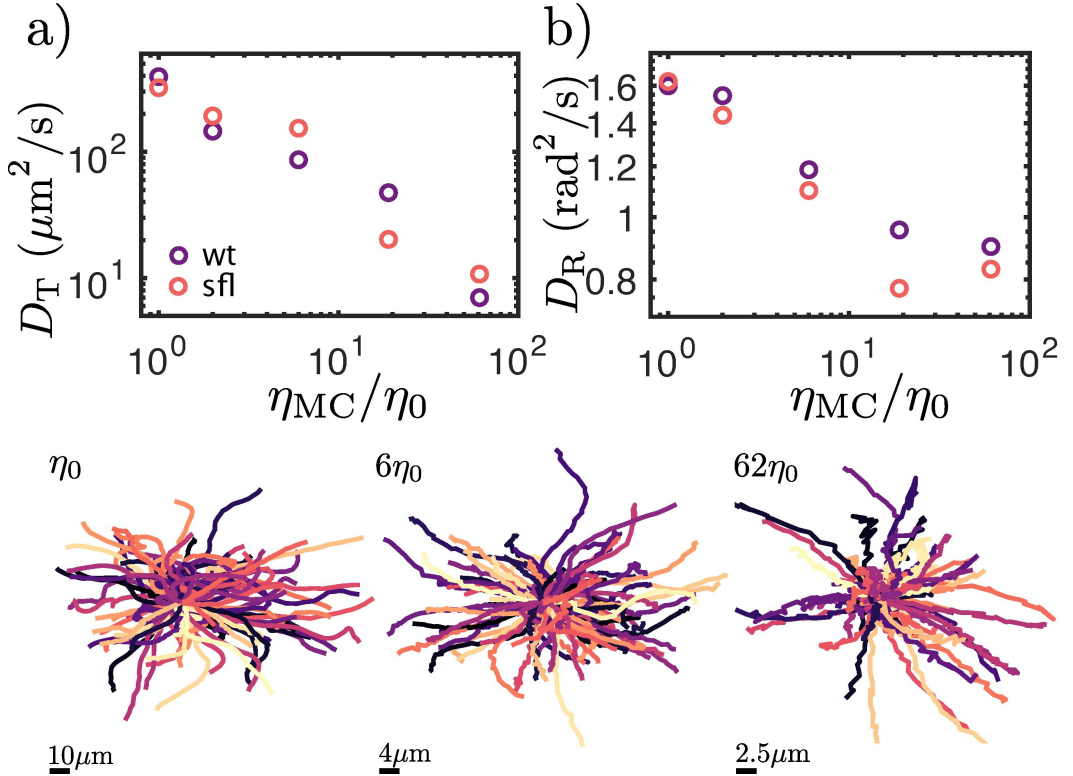


Figure 4.3: Top row: translational and rotational diffusion coefficients for wt and sfl CR as a function of the viscosity of the surrounding medium. Error bars smaller than the marker size. Bottom row: typical 3s trajectories for CR swimming in different viscosity media.

change in trajectory shape by considering the effect the surrounding viscosity has been predicted to have on CR flagellar beating and synchronization. G. S. Klindt *et al.* [62] have predicted that a high viscosity medium could induce anti-phase synchronization of the flagella i.e. freestyle swimming as opposed to the traditional breaststroke swimming which is observed at low viscosity.

### 4.3.2 Scattering at the Interface

After measuring how the velocity and diffusion properties of CR change in the two regions, we study the behaviour of the algae as they approach the interface. In order to avoid any bias from the diffusion of the gradient, we only consider trajectories obtained in the first 100s after setting up the two regions i.e. when the gradient is the sharpest (see Fig.4.2a). We then consider how the scattering angle  $\theta_{\text{out}}$  varies as a function of the incoming angle  $\theta_{\text{in}}$  for CR trying to cross the interface from the low viscosity region to the high viscosity region and viceversa. We define  $\theta_{\text{in}}$  and  $\theta_{\text{out}}$  as the average orientation of CR 1s prior to reaching and leaving the interface respectively.

As the algae can be considered to be swimming in 2D due to the height of the microfluidic device ( $20\mu\text{m}$ ), we do not take into account the role played by the azimuthal angle of approach. Angles are defined as shown in the insert in Fig.4.4b, where  $\theta_{\text{in}} \in [0, \pi/2]$  and  $\theta_{\text{out}} \in (-\pi/2, \pi/2)$  for low to high viscosity crossing attempts and  $\theta_{\text{in}} \in [-\pi/2, 0]$  and  $\theta_{\text{out}} \in (-\pi/2, \pi/2)$  for high to low viscosity ones.

When algae try to cross the interface to go from the low viscosity region to high viscosity one, we find that for small incoming angles ( $\theta_{\text{in}} \lesssim \pi/6$ ) both wt and sfl CR tend to scatter off it and stay in the low viscosity region. On the contrary, when approaching the interface from the high viscosity region, CR manage to cross to the low viscosity region. Furthermore, for the cases in which  $\eta_{\text{MC}}/\eta_0 > 1$ , we find  $\theta_{\text{out}}(\theta_{\text{in}})$  to have no significant dependence on the viscosity ratio between the two regions or the length of the flagella (Fig.4.4b). Fig.4.4a shows trajectories for wt CR approaching the interface for small and large incoming angles. This allows to visualise quite clearly how CR scatters off the interface for small angles when trying to cross from low to high viscosity but can cross successfully in the opposite case. Interestingly, the scattering effect we observe resembles that of crawling cells scattering away from high friction regions when trying to cross from a low friction one [65, 66]. We can understand the origin of these experimental results by using the theoretical model proposed by Datt and Elfring [42] in their work. The authors have in fact shown that a squirmer swimming through a region of linearly changing viscosity gradient will have an angular velocity of the form  $\mathbf{\Omega} = \frac{1}{2}\mathbf{U}_N \times \nabla(\eta/\eta_0)$ ,

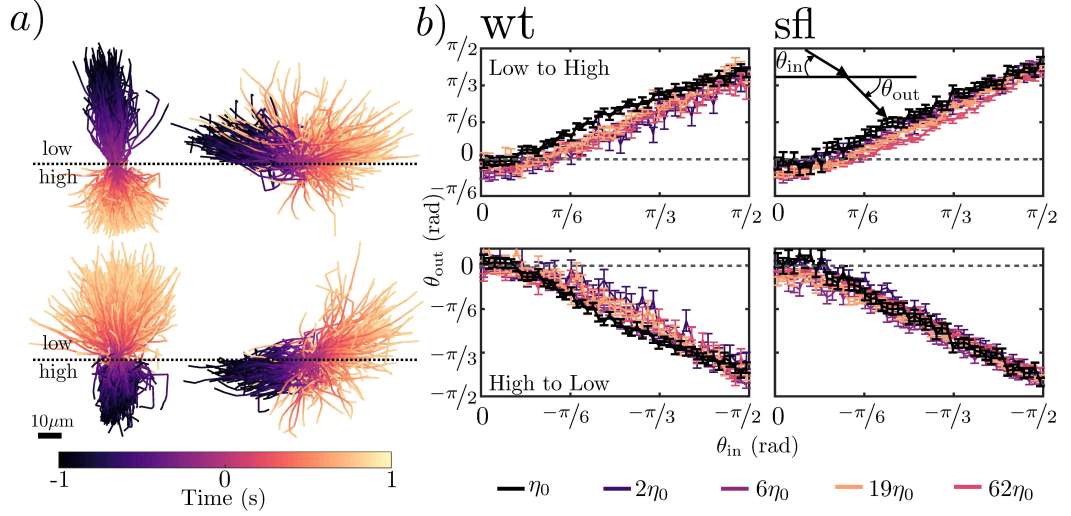


Figure 4.4: Left: examples of low and high incoming angle trajectories for wt CR trying to cross from low to high (0.30% MC,  $6\eta_0$ ) viscosity region and viceversa; Right: resulting outgoing angle for a given incoming angle when CR try to cross the interface. The black line indicates a control experiment, in which algae are crossing from the low viscosity region to an identical one. As expected due to rotational diffusion, control lines are not centred at 0 and perfectly straight [23]. For each line,  $\sim 10^5$  crossings were recorded and analysed.

where  $\mathbf{U}_N = (\frac{2B_1}{3})\mathbf{e}$  is the velocity of a squirmer in a Newtonian fluid of uniform viscosity and  $B_1$  and  $\mathbf{e}$  represent the first squirmering mode coefficient and the orientation of the microswimmer (full derivation and details can be found in the referenced work). We can then consider - similar to what has been done in [42] - the case in which the gradient increases linearly only in one direction. It is then immediately obvious that the torque caused by the change in viscosity will be at its greatest for the case  $\mathbf{e} \perp \nabla(\eta/\eta_0)$  and will tend to zero as  $\mathbf{e} \parallel \nabla(\eta/\eta_0)$ .

It is however necessary to point out that Datt and Elfring's model is based on two assumptions: i) the squirmers are freely swimming and are not bound by any surfaces and ii) the gradient is linear and slowly changing. Our experiments - as outlined in the methodology section - are performed in microfluidic chambers of  $\sim 20\mu\text{m}$  height and thus the algae examined in this chapter are not freely swimming but rather confined. This confinement has been shown to affect the properties of the flow field generated by CR algae both theoretically and experimentally [21, 67–69], therefore a direct comparison between our work and that of Datt and Elfring is not possible. Similarly, as we mentioned in the previous sections and in the methodology, the type of gradient we study in this paper is a sharp gradient rather than a linearly

increasing one. Nevertheless, we do believe the model outlined can offer a way to qualitatively understanding our results, particularly in the context of the concentration profiles analysed in the next section of this manuscript.

The equations of motion derived by Datt and Elfring *et al.* [42] for a squirmer in a viscosity gradient can also be used to gain some intuitive understanding as to why there is critical angle above which algae can cross successfully over a sharp interface. In fact, as the incoming angle  $\theta_{\text{in}}$  approaches  $\pi/2$  the swimmer will navigate deeper into the gradient before re-orienting towards the lower viscosity region. Since in our case the region of changing viscosity is of a finite length, results suggest that for angles over  $\sim \pi/6$ , algae can successfully reach the high viscosity region.

It is worth pointing out that while Datt and Elfring include the type of swimming gait in their work distinguishing between pushers and pullers, they do not include any potential change to swimming gait due to viscosity or viscous forces on individual flagella, which are likely to play a significant role in the effects reported in this chapter.

Lastly, we highlight our results agree with a recently published study by Stehnach *et al.*, who confirmed independently that CR exhibit viscophobic behaviour through similar experiments to those reported in this chapter [70].

### 4.3.3 Concentration Profile

To conclude our analysis of algae in regions of inhomogeneous viscosity, we studied the time evolution of the concentration profile of the algae in the chamber. Measurements were taken for 1000s, as it was established the gradient is stable in this timescale (Fig. 4.2). In order to quantify where the algae concentrate in the device we introduce the normalised ratio  $\nu$ , which is defined as  $\nu = (N_{\text{H}} - N_{\text{L}})/(N_{\text{H}} + N_{\text{L}})$ , where  $N_{\text{H}}$  and  $N_{\text{L}}$  are the number of algae in the high and low viscosity regions respectively.

Interestingly, we observe that wt CR concentrate in the low viscosity region for experiments with high viscosity of  $2\eta_0$  and  $6\eta_0$ , whereas the concentration remains uniform for the  $19\eta_0$  and  $62\eta_0$  cases. Similarly, sfl CR tend to concentrate in the low viscosity region. The results are particularly striking because recent studies have shown that it is possible to concentrate microswimmers in regions where their velocity is lower, due to the increased residence time. However, it is worth noting that the method of generating a velocity distribution in this paper is significantly different than those employed in those studies, in which photokinetic bacteria were used [71, 72].

We believe the results to be a combination of all the effects mentioned in the pre-

vious sections: (i) the velocity distribution, which favours concentration in regions where the algae swim slower; (ii) the decrease in angular diffusion for algae in high viscosity media; (iii) the re-orientation effect at the interface, which can help algae accumulate at low viscosity, since it will create a flux imbalance of algae in favour of the low viscosity region.

It is possible for the effects to cancel each other out, keeping the concentration profile uniform in the channel. Similarly, the effects can lead to accumulation in the low viscosity region, as is it shown in Fig.4.5.

Lastly, as mentioned in the introductory section, microswimmer response to viscous environments is caused by a complex interplay of active (mechanosensory) responses as well as passive ones (i.e. the increased drag on the flagellum and the body or the flow field signature of the microswimmer). Consequently, the results reported are valid for CR algae but are likely to differ for other types of microswimmers, such as sperm cells (pushers instead of pullers, see next Chapter), which have been reported to have a similar swimming velocity in low and high viscosity fluids [31] and would cross the interface differently due to their flow field, as predicted by Datt and Elfring [42].

## 4.4 Conclusions

In this chapter, we have studied the behaviour of the green alga *Chlamydomonas reinhardtii* in regions of inhomogenous viscosity and, in particular, how it navigates sharp viscosity gradients.

We show that CR motility is affected significantly by the viscosity of the surrounding environment, and that flagellar length affects how much it is slowed down for a given viscosity.

We use a Y-junction microfluidic device to generate a sharp viscosity gradient and analyse how CR algae navigate through it, showing that algae can always cross successfully when swimming from high viscosity to low viscosity but that the same is not true for the opposite case. In fact, we show that algae swimming from low viscosity to high viscosity can scatter off the gradient depending on their angle of approach. This is due to their flagella positioning and swimming gait: in fact, the scattering (i.e. returning towards low viscosity) occurs when CR approach the gradient almost parallel to it ( $\theta_{\text{in}} \leq \pi/6$ ). In such case, one of the flagella is in the high viscosity region and the other in the low viscosity one. A torque is then generated and CR turns towards lower viscosity, similarly to the “triangle swimmer” studied in simulation by Liebchen *et al.* (see Chapter 2) [41].

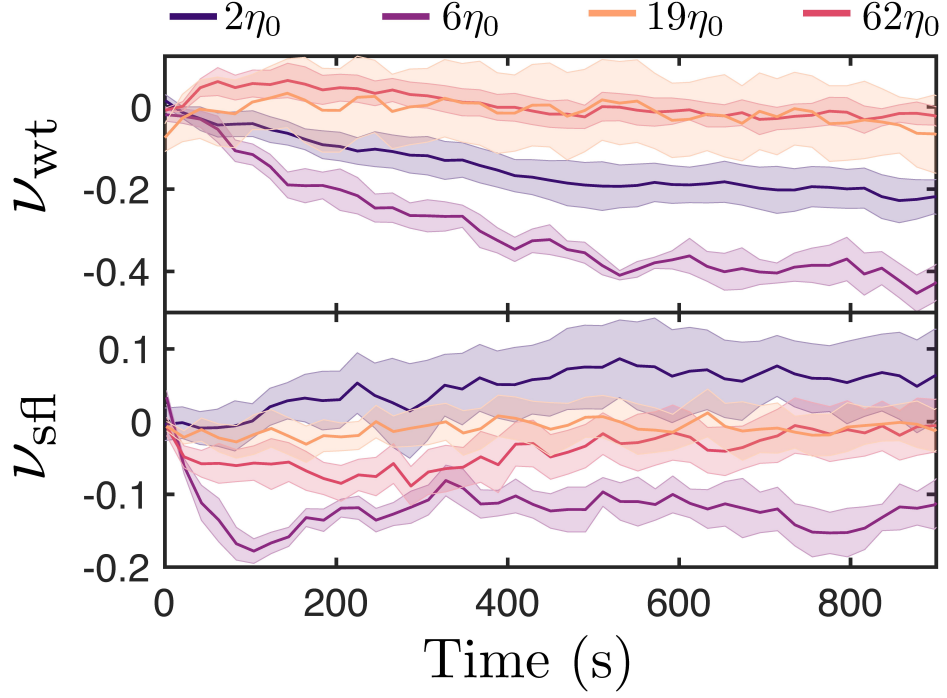


Figure 4.5: The time evolution of the normalised ratio  $\nu$  for wt (top) and sfl (bottom) CR for different viscosity ratios of the two regions. In all cases there is no accumulation in the high viscosity region ( $\nu \rightarrow 1$ ), but rather accumulation in the low viscosity region or nowhere at all.

Lastly, we measure how the concentration of algae in the microfluidic device evolves over time. In this case, results show an unexpected phenomenon of concentration in the low viscosity region (i.e. where algae swim faster) or no concentration at all - likely due to a net neutral combination of all the effects at play in the system, with the velocity gradient favouring concentration in high viscosity and the scattering favouring concentration in low viscosity.

## Chapter 5

# Ram Sperm behaviour at sharp viscosity interfaces

### 5.1 Introduction

As discussed in previous chapters, microorganisms often find themselves swimming in regions of inhomogeneous viscosity in nature. This is particularly true for sperm cells, as they have to navigate numerous environments of differing viscosity on their journey to the egg during fertilization [41, 73].

Despite the clear importance of understanding how sperm cells navigate viscosity gradients, experimental reports on the subject are currently not available in the literature due to technical challenges associated to performing such experiments. Nevertheless, previously published results and theoretical models offer an important starting point to design and interpret experiments.

For example, it has now been shown that sperm can swim efficiently even in environments up to 100 times more viscous than those of normal buffer, a clear difference from microorganisms such as *Chlamydomonas reinhardtii* (CR), as shown in Chapter 4 [39, 74].

The reports indicate sperm cells can adapt their flagellar waveforms to increase their swimming efficiency and sustain the higher mechanical load while retaining the majority of their swimming velocity - a feat which allows them to navigate through the complex, viscous environments of the female reproductive tract [39].

The clear difference in response to increased viscosity between sperm and CR further highlights how fluid properties, swimming dynamics and flagellum characteristics are all responsible for determining how a microswimmer will navigate viscosity gradients or swim in a high viscosity environment. For this reason, further experiments

are necessary to start developing an understanding of how sperm navigates viscosity gradients on its way to the egg.

In this chapter, we employ a similar methodology to that reported in the previous chapter to investigate how ram sperm cells navigate a sharp viscosity gradient, as well as how they respond to an increased viscosity of the media in which they are swimming.

We show that both flagella beating amplitude and frequency are reduced when sperm swims through a high viscosity environment, and that its swimming velocity is consequently affected. Interestingly, we see an initial increase in swimming velocities in environments twice as viscous as water, with velocity then being reduced for higher viscosities.

Lastly, we investigate how sperm navigates through a sharp viscosity gradient - as done for CR in the previous chapter. In this case, results show that no significant effect is present for sperm cells. Possibly due to a combination of sperm's flow field and gate as well as sperm's ability to adapt more easily to the increased viscosity as compared to CR.

## 5.2 Experimental Details

### 5.2.1 Media and Sample Preparation

High viscosity media solutions of Tryladyl (Minitube GmbH, Germany) and Methylcellulose (0.15, 0.50 and 0.75%) were prepared following the same protocol outlined in Chapter 4. Low viscosity media contained Tryladyl only, with no added Methylcellulose.

Frozen ram sperm samples were thawed and prepared via sperm washing following the steps reported in the Methodology chapter, as the experiments required a large volume of sample ( $<50 \mu\text{L}$ ) to be set up correctly.

### 5.2.2 Experimental Setup & Imaging

Despite the aim being identical to that of the previous chapter, technical limitations made it so that it was not possible to perform experiments with sperm cells following the same methods used for *Chlamydomonas reinhardtii* algae. In particular, some of the challenges were:

- i) it is not easy to re-suspend sperm samples in different viscosity media by centrifuging and removing the supernatant, as the sample will include a large percentage of non-motile cells;



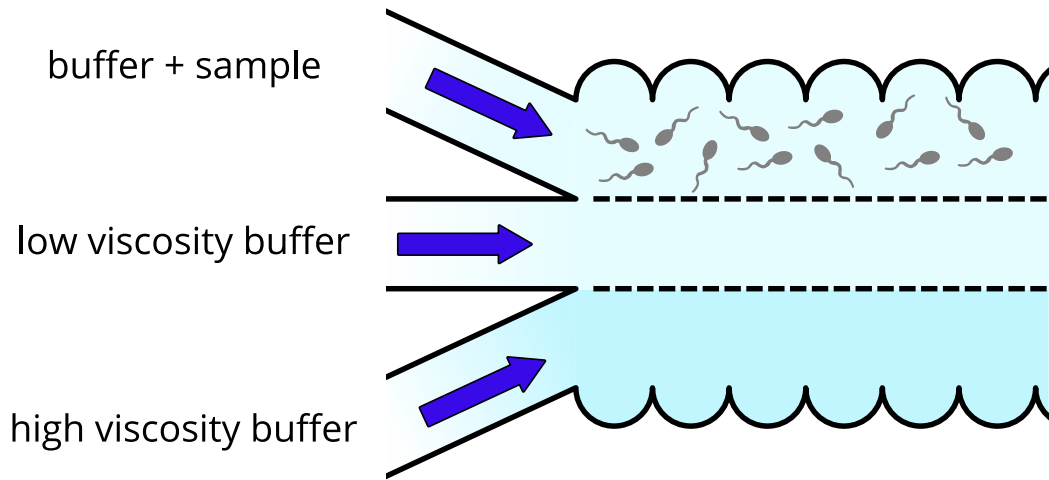


Figure 5.1: The device used to study sperm behaviour when crossing sharp viscosity interfaces.

- ii) experiments require a large volume to be set up as the syringe pumps need to be run for 2-5 minutes to ensure the different viscosity regions are appropriately set up;
- iii) it is not possible to use microfluidics sorting devices to get a high motility sample first as the sample will not have sufficient volume and cell density.

A new microfluidic device was designed to overcome the technical challenges outlined above. The device ( $50\text{ }\mu\text{m}$  tall) consists of a three-way junction which allows to flow through a diluted sperm sample, fresh Tryladyl buffer and the high viscosity media of choice. Similarly to the previous version of the device, different viscosity zones are set up by flowing the fluids in using two syringe pumps (one for the sample and low viscosity fluid, the other for the high viscosity buffer) ensuring flow rates are balanced to achieve regions of the same size. After the different viscosity regions are set up the motile sperm cells travel from the sample region to the other regions, allowing us to investigate how ram sperm navigates through the sharp gradient. The device also features concave walls (radius  $60\mu\text{m}$ ) to prevent sperm accumulation on the boundaries on the device.

Unfortunately this type of device does not allow us to obtain reliable cell concentration measurements as done in the previous chapter due to constant influx of sperm in the low and high viscosity areas from the buffer and sample region. Nevertheless, it allows us to study in detail sperm behaviour in uniform viscous environments as well as how the cells navigate through sharp viscosity gradients.

Images were acquired using an Edgertronic (<https://edgertronic.com/>) camera and a Pointgrey Grasshopper CCD camera for 150 fps and 20 fps imaging respectively. High speed images were acquired to study how sperm responds to an increase in the surrounding viscosity, while the 20 fps image sequences were used to study the behaviour of the sperm cells crossing the viscosity interface.

All imaging was performed using phase-contrast objectives. In particular, high speed images were acquired using at 30x magnification (20x with a 1.5x magnifier) while the images of sperm crossing the interface were acquired at 6x magnification (4x with a 1.5x magnifier). Imaging involving sperm crossing the interface was performed in the first 5 minutes after setting up the gradient to ensure it would be sharp and stable.

### 5.2.3 Data Analysis and Flagella Tracing

Particle tracking was performed as outlined in the methodology section to obtain the trajectories used for the analysis of sperm cells crossing the viscosity interface. Extra image processing was necessary to extract flagella data from high speed sequences and analyse it.

Tracking sperm flagella or filaments has been an interest of soft matter physicists for many years, thus it is not surprising that in recent years many methodology papers and open source image processing pipelines have been published on the subject [75, 76]. However, these methods are often based on high magnification darkfield imaging of the sperm flagella or images with very specific properties, making it hard to adapt them for one's unique purposes.

For this reason, we developed a code specifically designed to tackle the challenges we would encounter using image sequences collected using our setup.

The flagella tracking pipeline is divided in two sections: in the first section, the flagella and sperm heads are located in each frame of the sequence; in the second part, a semi-manual code creates trajectories for the sperm heads and assigns a flagella shape for each time-step, also giving the user the option to step in and manually draw or select the flagella shape.

The steps performed in the first section of the pipeline are outlined in Fig. 5.2. In brief, after some initial polishing and thresholding of the frame, a morphological opening is applied to identify the sperm heads in the image. It is then possible to obtain an image containing the sperm flagella by subtraction. Lastly, the *imskel* function is used to skeletonize the image and obtain the position and points making out each flagella in the image.

In the second part of the process, the user is asked to select one the sperm cells found in an arbitrary (user selected) starting frame. After that, the code constructs a trajectory for the sperm cell and locates the closest tracked flagellum at each step. For each step, the user is shown what the output would look like and can then choose between 5 options: (i) confirm and continue (ii) pick another flagellum tracked (iii) manually find the next position of the sperm head and draw the flagellum (iv) only draw the flagellum (v) stop tracking and exit programme.

Using this method, it was possible to combine the speed of automated particle tracking with the precision provided by human control and input where necessary. It is worth noting that for all the tracks analysed human input was kept to a minimum ( $<5\%$  of the frames analysed to build a track) and was mostly used to aid the programme in keeping track of sperm cells when the sperm head would rotate and thus potentially be missed by the tracking algorithm.

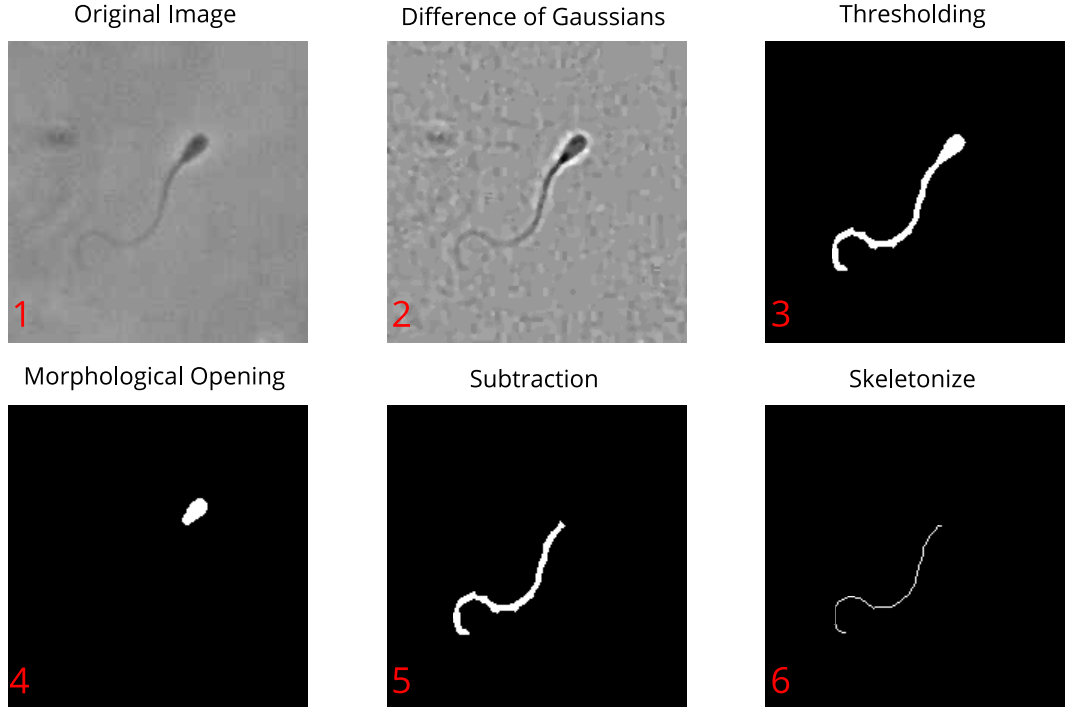


Figure 5.2: The image processing steps performed to extract the sperm head position and the respective flagella shape from high speed images. Difference of Gaussians refers to the process of subtracting from the original image one that has undergone gaussian blurring with  $\sigma = 2$ . Subtraction refers to the difference between image 3 and image 4 to obtain a binary image with the flagella shape only.

## 5.3 Results & Discussion

### 5.3.1 Ram Sperm Motility in High Viscosity Media

We measured sperm cell velocity in media ranging from Tryladyl with no added MC to Tryladyl + 0.75% MC. Results show that - unsurprisingly - increasing the viscosity of the media causes ram sperm cells to swim slower due to excess mechanical load. Interestingly however, despite an increase in viscosity up to  $\sim 60\eta_0$  (where  $\eta_0$  is the viscosity of water) the sperm retain a large percentage of their progressive velocity. This is similar to previously reported results by Smith *et al.* for human sperm, and has at its origin the need for sperm to navigate high viscosity environments on the way to the egg [32, 73].

Another interesting finding from our analysis of the swimming velocity of sperm cells as a function of viscosity, is the initial increase in velocity before a reduction due to the increased load. This is likely caused by a significant reduction in cell yawing during swimming, which allows sperm to travel faster when the increased mechanical load is not yet enough to start hindering its motion.

To quantify the amount of yawing by the sperm head, we measure the amplitude of the lateral head displacement (ALH). This is calculated by constructing the average trajectory first (the red line in Fig. 5.3b) and then measuring the distance between the head and the average line at each time-step. This generates a sinusoidal signal from which we can calculate the ALH as double the average peak displacement. Furthermore, the ALH is directly related to the bending of the proximal region of the tail - thus giving us information on the curvature of the flagellar beating pattern [77].

We find that ALH is reduced when viscosity is increased, indicating that sperm yawing is reduced as well as the bending of the flagellum (i.e. the flagellum is straighter). This result echoes previously published measurements for human sperm, which it have showed that the wavelength of the wave propagating along the flagellum increases in high viscosities, leading to reduced yawing and bending [31, 32].

Next we look at the flagellar waveforms of sperm swimming in different viscosities, focussing in particular on curvature amplitudes and beating frequencies.

We find the beating frequencies by considering how the curvature of the sperm flagellum at a given arclength along it ( $15\ \mu\text{m}$ ) varies over time. As the curvature reflects the periodicity of the flagellar beating, it is possible to evaluate its autocorrelation function to remove any noise from the measured signal and extract from the beating frequency of the sperm flagellum [78].

Through this analysis, we find that sperm beats at  $\sim 10$  Hz in low viscosity buffer,

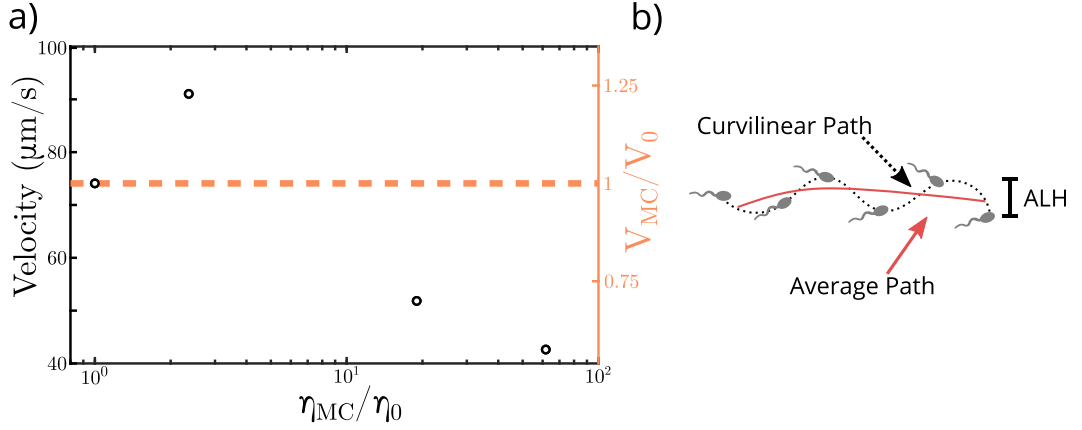


Figure 5.3: a) Sperm velocity as a function of viscosity, calculated from the average path, b) schematic outlining the sperm motility parameters measured in the chapter.

while the frequency is reduced to  $\sim 3$  Hz once the viscosity is increased ( $19$  and  $62\eta_0$ ).

The result highlights the remarkable ability sperm has to adapt its swimming gait in environments of high viscosity to increase its swimming efficiency. In fact, despite reducing its swimming frequency to a third of the original one, the swimming velocity only drops to just over half of the swimming velocity in low viscosity buffer. This suggests that - similar to human sperm - ram sperm increases its swimming efficiency by covering a larger distance per beat. Furthermore, the reduction in ALH highlights that the method used to increase swimming efficiency is the same (i.e. increase the radius of curvature of the flagellum) [31, 32].

### 5.3.2 Crossing Viscosity Interfaces

The scattering angles for sperm cells approaching the interface were obtained by calculating the average trajectory traced by sperm cells in the 1s before and after hitting the viscosity discontinuity, through which the angle of approach  $\theta_{\text{in}}$  and angle of escape  $\theta_{\text{out}}$  could be calculated (Fig. 5.5). To help with comparison, we keep the angle ranges equal to those from Chapter 4.

An important distinction to make between sperm and *Chlamydomonas reinhardtii* is how trajectories normally look in low viscosity media, in particular how curved they are. Sperm has a pronounced flagellar asymmetry which leads to trajectories generally being curved rather than straight with tumbles (as is the case for CR). This appears clear in the control line in Fig. 5.5, in which it is possible to note that the relationship between  $\theta_{\text{in}}$  and  $\theta_{\text{out}}$  is not the same as in CR, with it being better represented by a curve of the type  $y = mx - q$  rather than  $y = mx$  as is the case

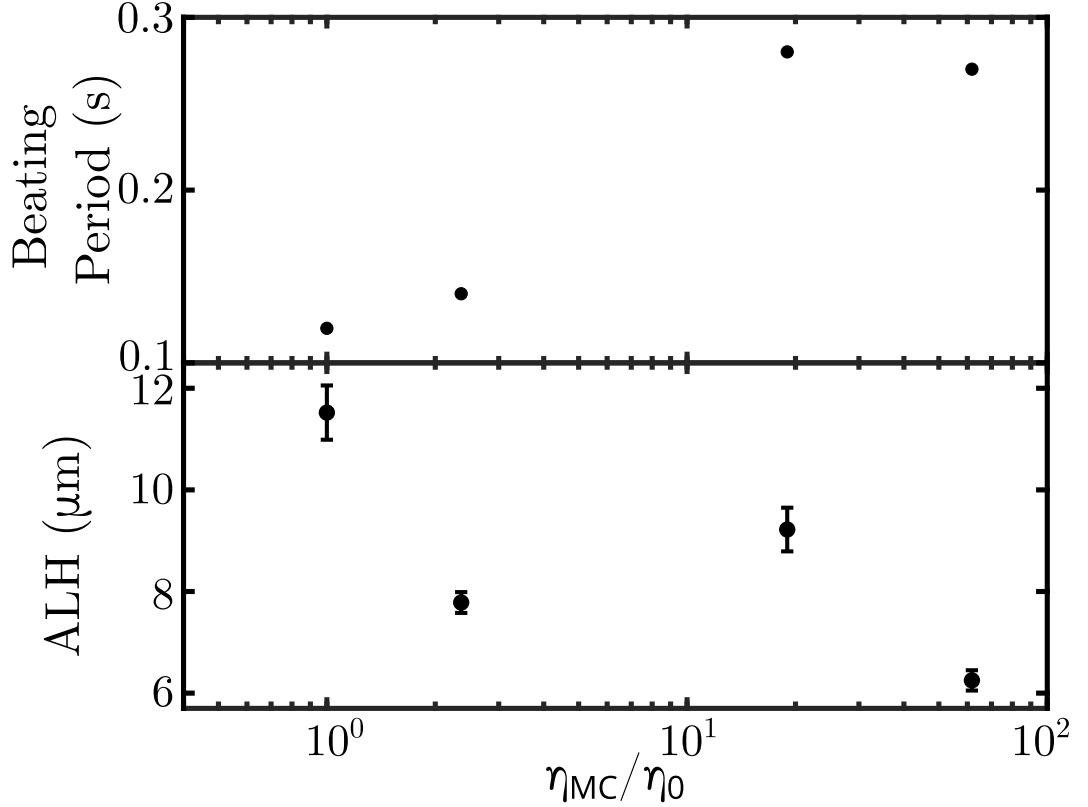


Figure 5.4: Top: beating period of sperm flagella as a function of viscosity. Error bars smaller than marker size. Bottom: Amplitude of the lateral head displacement as a function of viscosity.

for CR.

The particular type of trajectories usually traced by sperm complicate the analysis, but nevertheless it is possible to draw some conclusions by comparison with the other measured lines, which regard events when the gradients are set up with 0.15%, 0.50% and 0.75% MC (2, 20 and  $60\eta_0$  respectively).

Results show that any events in which sperm cells turn away from the gradient are consistent with how sperm trajectories are normally curved due to flagellar asymmetry, thus meaning that no scattering is present for ram sperm regardless of whether the gradient is approached from the low or high viscosity region.

To understand why no significant effect is measured for sperm cells, we can consider how sperm achieves propulsion and compare the results from Fig. 5.5 to those reported in the previous chapter for CR.

CR achieve propulsion through two front flagella which perform a breaststroke motion, whereas sperm has a single flagellum which moves in a whip-like manner to

propel the cell forward. Results from Chapter 4 suggest that scattering effects at the interface are a consequence of the two CR flagella being in different media, thus experiencing different forces which lead to a torque imbalance through which the algae are rotated towards the low viscosity region.

This situation resembles closely that of the “triangle” microswimmer in a viscosity gradient studied by Liebchen *et al.* (see Chapter 2) [41], which also moves towards the low viscosity region of a gradient due to a torque imbalance similar to that cause by the two CR flagella.

On the contrary, sperm resembles the dumbbell microswimmer studied in the simulations - particularly at higher viscosities when cell yawing is reduced. As mentioned in Chapter 2 this type of swimmer does not experience any torque imbalance and is able to navigate through gradients without them affecting its swimming direction.

Furthermore, as shown in the previous part of the results section, sperm is not affected by an increase in viscosity as much as CR. This suggests that perhaps an effect would be seen in a smoother gradient, if the inhomogeneous viscosity had a longer time to affect the trajectory - but that is outside the scope of this chapter.

We also highlight that these results somewhat disagree with predictions made by Datt and Elfring in their theoretical model, according to which all types of swimmers (pullers, pushers or squirmers) will be re-directed towards the low viscosity region of a gradient. However, we believe the difference in results to be an opportunity to highlight how important it is to include the shape and swimming gait of a swimmer in ones model to make accurate predictions, as they play a fundamental role in how the microswimmer responds to the gradient.

## 5.4 Conclusions

In this chapter, we have studied the motility of ram sperm in regions of increasing viscosity. Through our analysis, we show that - as expected - sperm has the peculiar ability to retain most of its swimming velocity even in viscosities as high as 60 times that of water contrary to other microswimmers (see *Chlamydomonas reinhardtii* in the previous chapter). Furthermore, by analysing the amplitude of the head displacement and the frequency at which the sperm flagellum beats as a function of viscosity, we provide evidence that bull sperm modifies its swimming gait at higher viscosities to swim with greater efficiency, thus retaining most of its swimming speed. This change in gait resembles that observed in human sperm, with the flagellum bending less at higher viscosities [32].

We then turn our attention to how ram sperm navigates sharp viscosity gradients

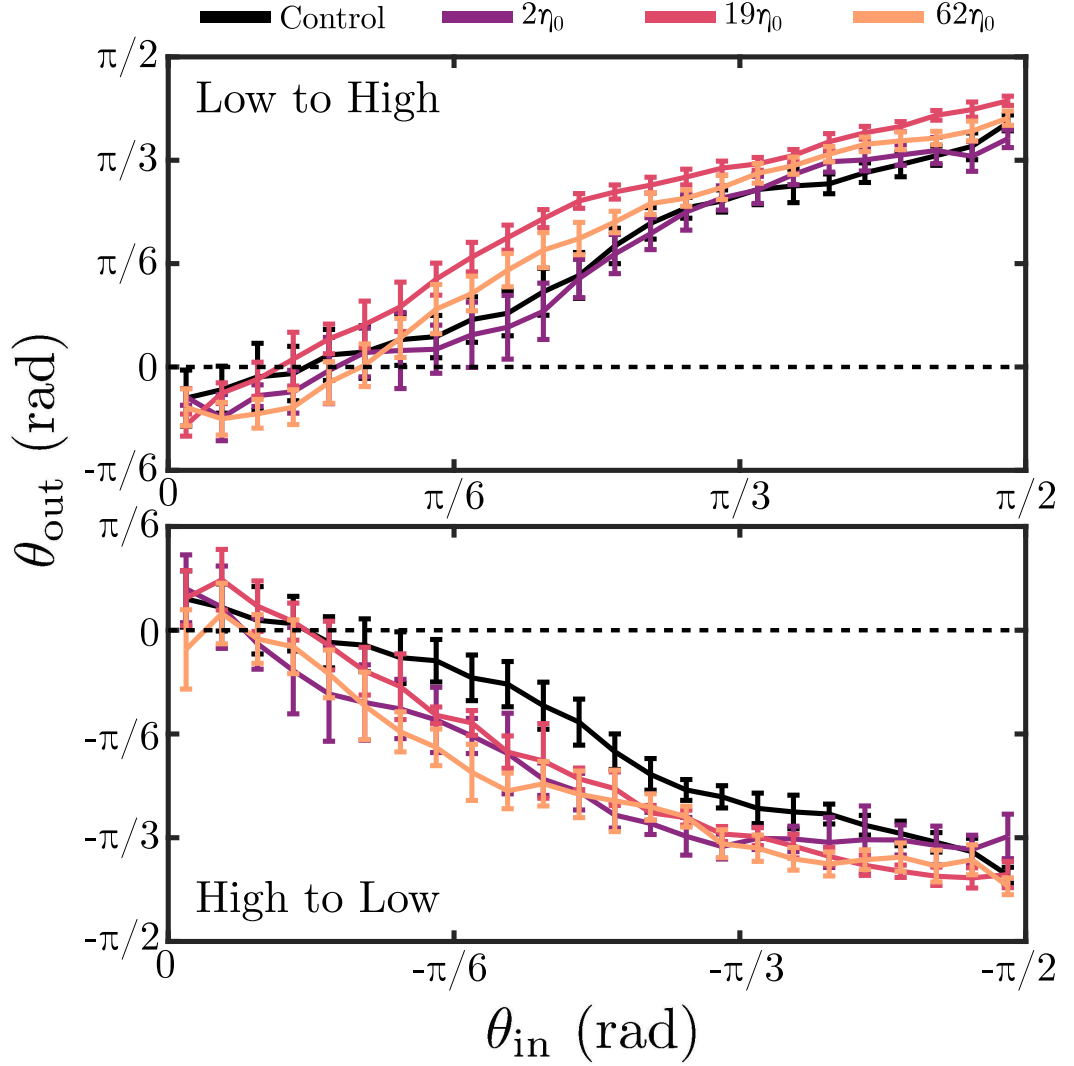


Figure 5.5: Sperm scattering at the viscosity interface when crossing from low to high viscosity (top) or viceversa (bottom). Control lines are found from sperm swimming from low viscosity to low viscosity. The control lines are not perfectly straight and centred at origin as they will be affected by the rotational diffusion of the swimming cells.

in attempt to draw a comparison between a “pusher” microswimmer (sperm) and a “puller” microswimmer (*Chlamydomonas reinhardtii*, Chapter 4). We show that no effect is present for sperm, which is able to navigate from low to high viscosity and viceversa without any measurable scattering effects. This is in contrast with what is observed in Chapter 4 for *Chlamydomonas reinhardtii*, which can scatter off the gradient when approaching it from the low viscosity region.



We conclude the lack of scattering is caused by how propulsion is achieved by sperm i.e. a single flagellum at the back, rather than two flagella at the front, which doesn't allow any torque imbalances to be generated even when sperm approaches the gradient almost parallel to it.

## Chapter 6

# Curved Ratchets improve Bacteria Rectification in Microfluidics Devices

This chapter is based on work which has been published in a peer-reviewed journal during the PhD:

Coppola, S., Kantsler, V. *Curved ratchets improve bacteria rectification in microfluidic devices*. **Phys. Rev. E** 104, 014602 (2021).

### 6.1 Introduction

Being able to control microbial behaviour not only allows us to answer important biological questions, but also makes it possible to develop biomedical technologies with a wide range of applications, from reducing biofouling on ship hulls to advancing IVF methods by improving sperm sorting methods [79, 80].

External cues such as chemical or viscosity gradients are however not the only way to modulate microswimmer concentration profiles: mechanical cues such as specifically designed walls or obstacles can help concentrate swimmers in desired areas, or even separate them depending on size and shape [81, 82].

Therefore, numerous studies have been carried out in an effort to understand how microorganisms behave near boundaries [13, 83, 84]. Through this, it has been shown that microorganisms behave differently near walls depending on their swimming gait [21]. In particular, it was found that pushers (i.e. sperm and bacteria) accumulate on flat walls, while pullers (i.e. *Chlamydomonas reinhardtii*) quickly re-orient and scatter away from them [67]. This is caused by the positioning of

the flagella in the two cases: “pushers” have their flagella located at the back of their body and keep pushing into the wall once they reach it, “pullers” have flagella located at the front of their body, and use them to re-orient themselves when they reach a flat surface [21, 85–87].

With the advent of microfluidics in active matter research and the possibility to easily design environments with specific geometries in which to assess microbial motility, it has also been possible to study and understand how microorganisms behave near curved walls of different sizes and properties (i.e. concave, convex).

These studies revealed that bacteria tend to follow convex surfaces and that concave walls can be used to reduce bacteria accumulation near walls by reorienting bacteria towards the bulk [88, 89]. These effects have since been studied in detail through simulations, theoretical models and further experiments aimed at understanding how simple circular obstacles (i.e. pillars) can be used to modulate the diffusion of microorganisms [13].

It is also possible to produce microfluidic devices with obstacles (ratchets) specifically designed to re-orient bacteria in a specific direction. Such obstacles have been studied experimentally by Galajda *et al.*, who studied the behaviour of bacteria in two chambers separated by a series of “V” shaped funnels (Fig. 6.1) which rectify bacteria motion towards one of the two chambers by allowing bacteria to cross in one direction but not the other, as bacteria will follow the obstacle boundary [46]. These results have since been investigated further through detailed numerical simulations and theoretical models, which have highlighted the possibility of developing ratchets with specific geometries to accommodate a number of different applications; from simply re-orienting bacteria to developing drug delivery systems and separating mixtures of active and passive particles [90].

Despite this, not a lot of attention has been dedicated to how such rectification devices relying on ratchets can be optimized experimentally, with the “funnel” geometry generally being the preferred one in experimental work.

In this chapter we investigate how ratchet geometry can influence bacteria rectification processes and how it is possible to take advantage of specific shapes to optimize rectification effects. We use a smooth-swimming (i.e. non-tumbling), fluorescent strain of the model microswimmer *E. coli* HCB1773 to compare the ratchets, revealing that indeed their geometry plays a key role in sorting the bacteria - and that ratchets with curved geometries perform better than the funnel geometry previously presented in the literature. We investigate these results further by showing ratchet performance is dependent on the time bacteria spend on its surface as well as the angle at which they depart it.

Lastly, we perform simple numerical simulations to verify our findings and confirm that curved ratchets are better performing than funnel ones.

## 6.2 Methodology

Polydimethylsiloxane (PDMS) devices were fabricated through standard soft lithography techniques. The devices ( $\sim 3\mu\text{m}$  tall) consist of a central  $4\times 1$  mm chamber with two reservoirs on the sides, where the inlets are also located (Fig. 6.1). The main chamber is divided in four regions separated by a series of ratchets (gap size  $20\mu\text{m}$ ), and the height of the devices ensures bacteria are confined to move only in 2D. The effects of 8 different ratchet geometries are compared in this paper. Ratchet geometries include the previously studied “funnel” design as well as curved geometries with half-circle concavities. We describe ratchet geometries by introducing the parameters  $R_{\text{in}}$  and  $R_{\text{out}}$ , which refer to the radius of the concavities re-orienting the bacteria and the radius of the main body of the ratchet respectively (see Fig. 6.1).

To prevent any flat wall accumulation effects, the chamber walls are made up of a series of concavities, which are known to reduce bacteria concentration at the surface up to 50% compared to flat walls [88, 91].

PDMS devices were bonded to glass coverslips through a plasma cleaning process, in which they were left inside a plasma cleaner (Harrick) for approximately 2 minutes and then - after being bonded - placed on a hot plate set at  $80^\circ$  for a short amount of time ( $\leq 5$  minutes) for optimal bonding. The coverslips were treated in a 30% w/w  $\text{H}_2\text{O}_2$  solution (Sigma Aldrich) for  $>24$  hours before being used to ensure a successful plasma cleaning process and reducing the chances of bacteria sticking to the walls.

In order to facilitate filling devices - which is made significantly harder than normal due to their low height - we filled devices minutes after taking them off the hot plate: this ensured the devices would still be hydrophilic due to the effect of plasma cleaning on PDMS, thus reducing the possibility of having air bubbles trapped inside them [92].

Lastly, the devices were sealed by injecting unpolymerised PDMS in the inlets and outer reservoirs to eliminate any drift effects which could contribute to the concentration profile measurements.

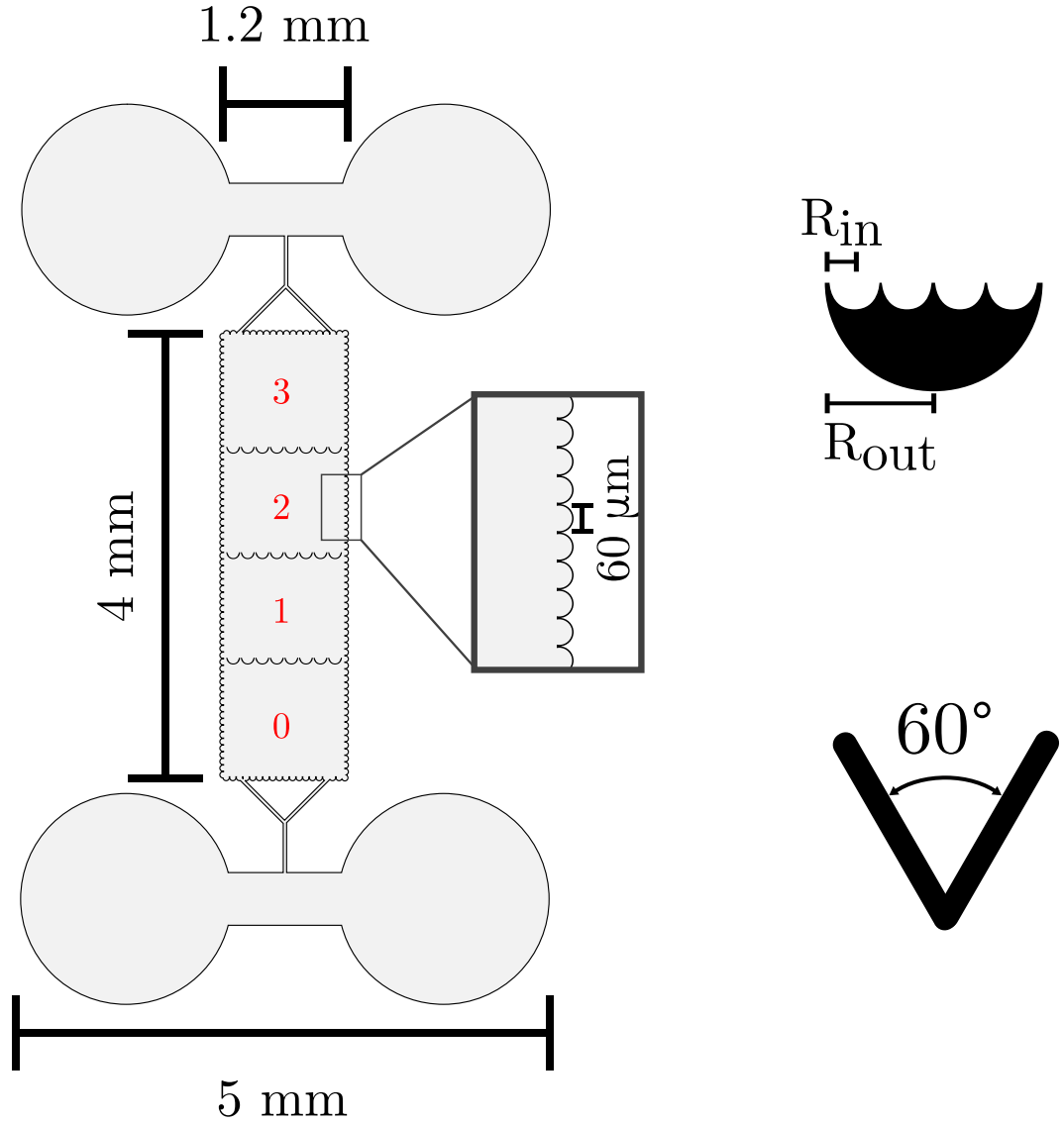


Figure 6.1: Left: a schematic of one the microfluidics devices used to perform the experiments, including all relevant details and dimensions. The numbers indicate the direction in which bacteria are rectified towards. Right: an example of a ratchet with a curved geometry, and a typical “funnel” ratchet.

### 6.2.1 Microscopy and Imaging

Frames of the initial conditions of the first and last chamber of the devices were recorded at the start of the experiments. After that, 10s at 15fps were recorded every 150 seconds. Bacteria counts were obtained by averaging the number of bacteria counted in each frame to reduce any random error due to image processing.

Microscopy was performed on a Nikon Eclipse inverted microscope equipped with a

phase contrast (PhL), plan fluorite corrected 4x objective (Nikon, NA 0.13). Frames were acquired through a 1920x1200 CCD camera (FLIR Grasshopper3).

High magnification images of the bacteria approaching the ratchets were recorded through a sCMOS camera (Andor Zyla 5.5) at 10fps. A 40x oil immersion objective was used (Zeiss, NA 1.3) to ensure the fluorescent bacteria would be clearly visible. Image frames were analysed through custom MATLAB (Mathworks) and ImageJ scripts using the tracking methodology outlined in the Methodology Chapter. Figures were arranged in panels using the open-source software Inkscape. The software was also used to make the schematics presented in Fig. 6.1, which were then converted in MATLAB for use in the simulations.

## 6.3 Experimental Results

### 6.3.1 Concentration Curves

In order to quantify bacteria accumulation in the experiments, we introduce the ratio  $C(t)/C_0$ , in which  $C(t)$  and  $C_0$  are the number of bacteria in the last chamber at time  $t$  and the number of bacteria in the first chamber and the start of the experiment respectively. We define chamber numbering in relation to the direction in which motion is rectified by the ratchets (i.e. the last chamber is the one bacteria are re-oriented towards).

Fig. 6.2 shows bacteria density in the last chamber increases over time for all the ratchet designs we performed experiments with. Furthermore, results show that the ratchets' design affects their performance, with some performing better than others over the timescale of the experiment. In particular, we find that curved ratchets outperform the funnel design by 20-30%.

We believe this effect to be caused by two main differences between funnel and curved ratchets: (i) by varying the radius of the curved ratchets, we can modulate the re-orientation time of the bacteria, reducing it to improve performance; (ii) smooth-swimming bacteria can occasionally get stuck in the funnel ratchet, while such type of effect is much less prevalent when bacteria swim on curved surfaces. We find this interpretation to be consistent with previous experimental results which show sperm cells (pushers, like bacteria) accumulate at the apex of V-shaped ratchets but are successfully re-oriented by rounded obstacles [93].

Unsurprisingly,  $R_{in}$  is the biggest contributor to ratchet performance, as it is clearly shown in Fig.6.2. In particular, we find that ratchets with smaller radius perform better than their larger counterparts. More details of these effect are shown in

the next section, but conceptually the reason for this result is immediately obvious: ratchet with large  $R_{\text{in}}$  require a longer time to re-orient bacteria, whereas for smaller radii, bacteria re-orient quickly and point towards the next section of the device.

We also find that  $R_{\text{out}}$  plays a role in determining rectification effects. By comparing the concentration ratio curves between the ratchet  $R_{\text{in}}=15\mu\text{m}$ ,  $R_{\text{out}}=120\mu\text{m}$  and its counterpart with  $R_{\text{out}}=60\mu\text{m}$ , it is clear that the latter outperforms the former by 30%. This once again requires a detailed analysis of bacteria trajectories on this surfaces (see next section) but can be explained by the likelihood of bacteria detaching from the outer side of the ratchet before reaching the next chamber increasing with the outer radius of curvature of the ratchets.

We point out that - despite having the smallest  $R_{\text{in}}$  - the ratchets with  $R_{\text{in}}=7.5\mu\text{m}$  are by far the worst performing, showing barely any sign of bacterial rectification of all. This is due to the resolution limits of the photolithography process, in which sharp corners tend to be smoothed out when the chamber geometry is transferred from the photomask to the wafer used to produce the devices. As a consequence of this effect, concavities as small as those are reproduced in the microfluidic device as - effectively - a flat wall with small dents which bacteria can swim over.

We include the results as we believe they (a) offer a good “control” experiment of how the device would perform with effectively no re-orienting concavities and (b) allow us to make the point that higher resolution techniques could be used to obtain even better rectification results.

We do highlight however that there is likely to be a fundamental limit to how much re-orienting concavities can be reduced in size before effects such as trapping start arising. It is also likely that reducing significantly the size of the ratchets to approach the scale of a swimming bacterium would likely lead to the bacterium simply swimming over the concavities, i.e. not being rectified. However, a detailed study of the hydrodynamics at play in such systems and experiments allowing for better feature resolution in microfluidics devices, such as micropattern generator. We point out that in an ideal case, the ratio  $C(t)/C_0$  should tend to 4 as  $t \rightarrow \infty$  (i.e. all bacteria have successfully moved to the final chamber), but in our experiments we measure final values of the ratio ranging from 1.3 to 2. One obvious reason for this is result is the length of time for which experiments are carried out, as reaching  $C(t)/C_0 = 4$  is likely to take significantly longer than 30 minutes. The second reason is the size of the device and - more specifically - the size of each chamber ( $\approx 1000\mu\text{m}$ ): even when the bacteria get successfully re-oriented towards the next chamber (and despite them being smooth swimmers), the length of the chamber will be longer than the characteristic length of their path. This will cause them

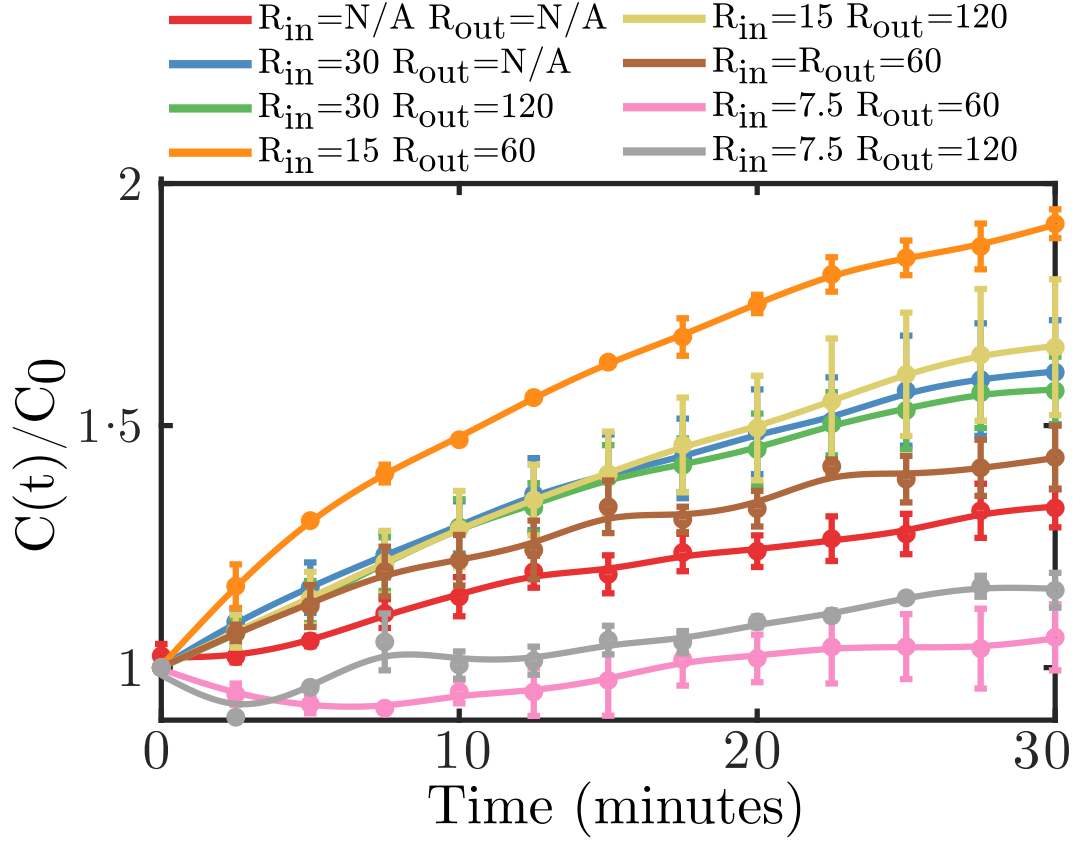


Figure 6.2: Concentration curves for all the ratchet geometries studied in the paper. N/A indicates a funnel geometry. Results show clearly that  $R_{in}$  plays a key role in improving ratchet performance. Each line is the average of 3 experiments.

to hit to the wall, where the concavities will re-orient the bacteria with an angle approximately perpendicular to the wall (and the direction of motion towards the next chamber).

Nevertheless, we believe the larger size of the chambers, coupled with the properties of the wall employed in the experiments allow us to compare effectively how good each ratchet geometry is without results being skewed by bacteria following flat walls or similar phenomena.

### 6.3.2 Ratchet Comparison

To further understand why certain ratchet geometries perform better than others, we analyse how bacteria trajectories vary depending on the specific geometry.

Fig. 6.4a shows the residence time of bacteria on the inner ( $R_{in}$ ) and outer ( $R_{out}$ ) side of the ratchet. This is defined as the time it takes for the bacteria to hit the



surface of the ratchet, and then leave it. We find that the geometry of the outer side of the ratchet is not as important as that of the inner one, with all three geometries providing a circa 60% success rate of bacteria crossing to the successive chamber one they hit them. However, as described in the previous section, reducing the the outer radius  $R_{\text{out}}$  improves rectification results (Fig. 6.2) so that should be a factor to take into account when designing ratchets for optimal performance. We also report on

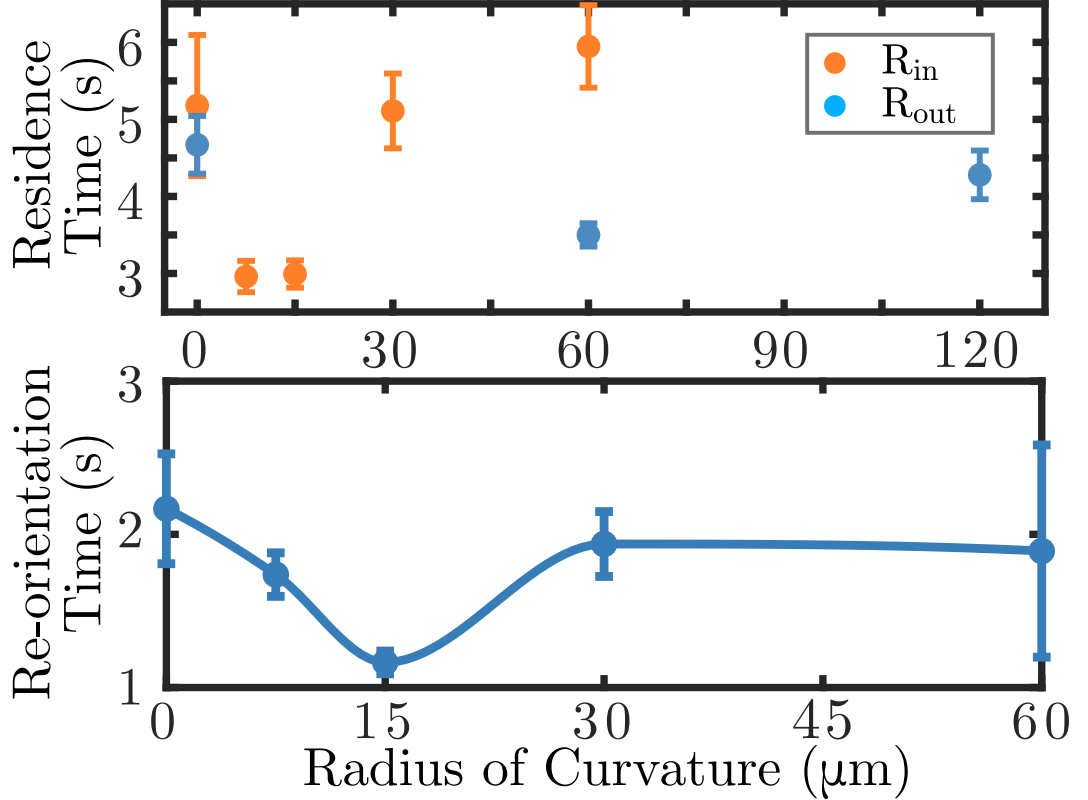


Figure 6.3: Top: the average time bacteria spend on the ratchets when they hit their inside surface (orange) and outside surface (light blue). To facilitate comparisons, we place funnel geometries at  $R=0\mu\text{m}$ . Bottom: the average time it takes bacteria to be re-oriented towards the successive chamber, when they hit the ratchet. For each point  $>10^2$  trajectories were analysed.

the re-orientation time of bacteria once they reach the inner side of the ratchets. The re-orientation time is defined as the amount of time it takes the bacteria's orientation angle to go from the range  $[-\pi/2, 0]$  i.e. pointing towards the first chamber, to  $[0, \pi/2]$  i.e. pointing towards the final chamber (Fig. 6.4b). Results show that circular ratchets generally perform better than the funnel geometry, which instead has a larger re-orientation time. Furthermore, performing the residence time analysis for bacteria approaching the outer side of the ratchet shows a reduction from  $\sim 5\text{s}$  to

$\sim 3.5$ s in residence time for smaller values of  $R_{\text{out}}$ , explaining why better effects can be obtained for ratchet with same  $R_{\text{in}}$  but different  $R_{\text{out}}$ .

One point to analyse further is that of the residence time results for the  $7.5\mu\text{m}$ . In fact, while the residence time of bacteria on that type of ratchet is as low as the best performing ratchet ( $30\mu\text{m}$ ) - results show devices with this type of geometry perform the worst, effectively showing no rectification effects. To analyse this effect we look at the trajectories of bacteria on this type of ratchet, which highlight the problem previously mentioned in section 6.3.1: ratchets with a radius of  $7.5\mu\text{m}$  are effectively equivalent to flat walls with small dents. Because of this, bacteria are able to swim along them and do not get re-oriented successfully, thus maintaining an orientation parallel to the ratchet surface after leaving it. To further analyse this point, we

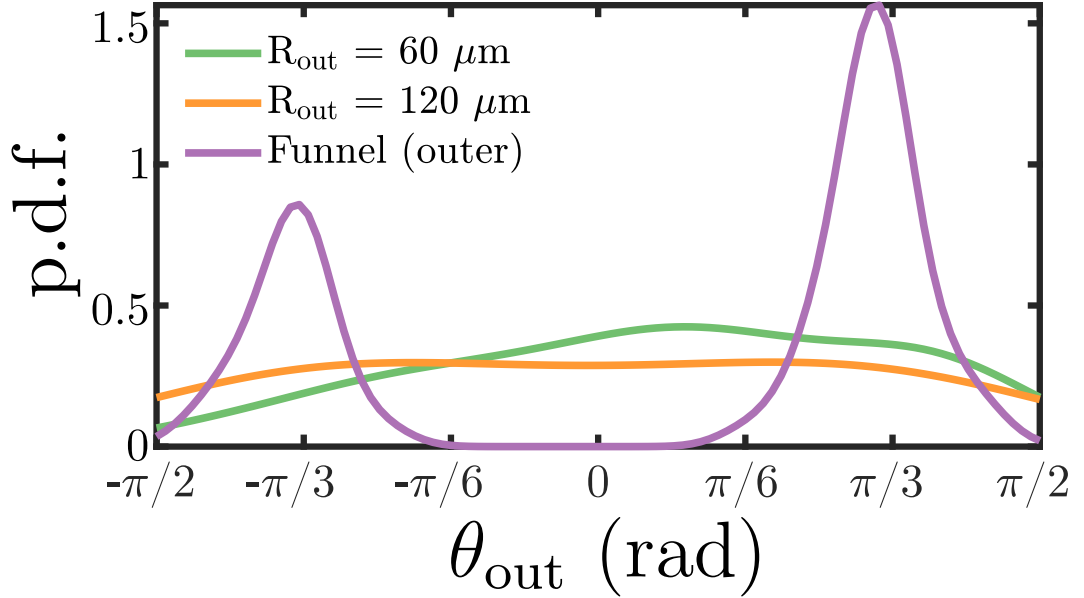


Figure 6.4: Experimentally determined scattering angle for bacteria approaching the ratchets from the outer side (i.e. trying to go to the next chamber) for the funnel and  $R_{\text{out}}=30, 60\mu\text{m}$  ratchets. Negative angles indicate events in which the bacteria stay in the original chamber, positive angles indicate successful crossing events. P.d.f. curves were obtained by fitting a kernel density estimation to the respective histograms. The funnel p.d.f. peaks at  $\pm\pi/3$  indicate that bacteria follow funnels and depart at angles parallel to their surfaces.

measure the probability density function of the angle  $\theta_{\text{out}}$  at which bacteria leave the ratchets after swimming along them (Fig. 6.5). We define the case  $\theta_{\text{out}} = \pi/2$  as the case in which bacteria swim directly towards the successive chamber, and the case  $\theta_{\text{out}} = 0$  as that in which bacteria swim vertically (i.e. towards the wall). Results show that all ratchet geometries have similar  $\theta_{\text{out}}$  distributions, with the

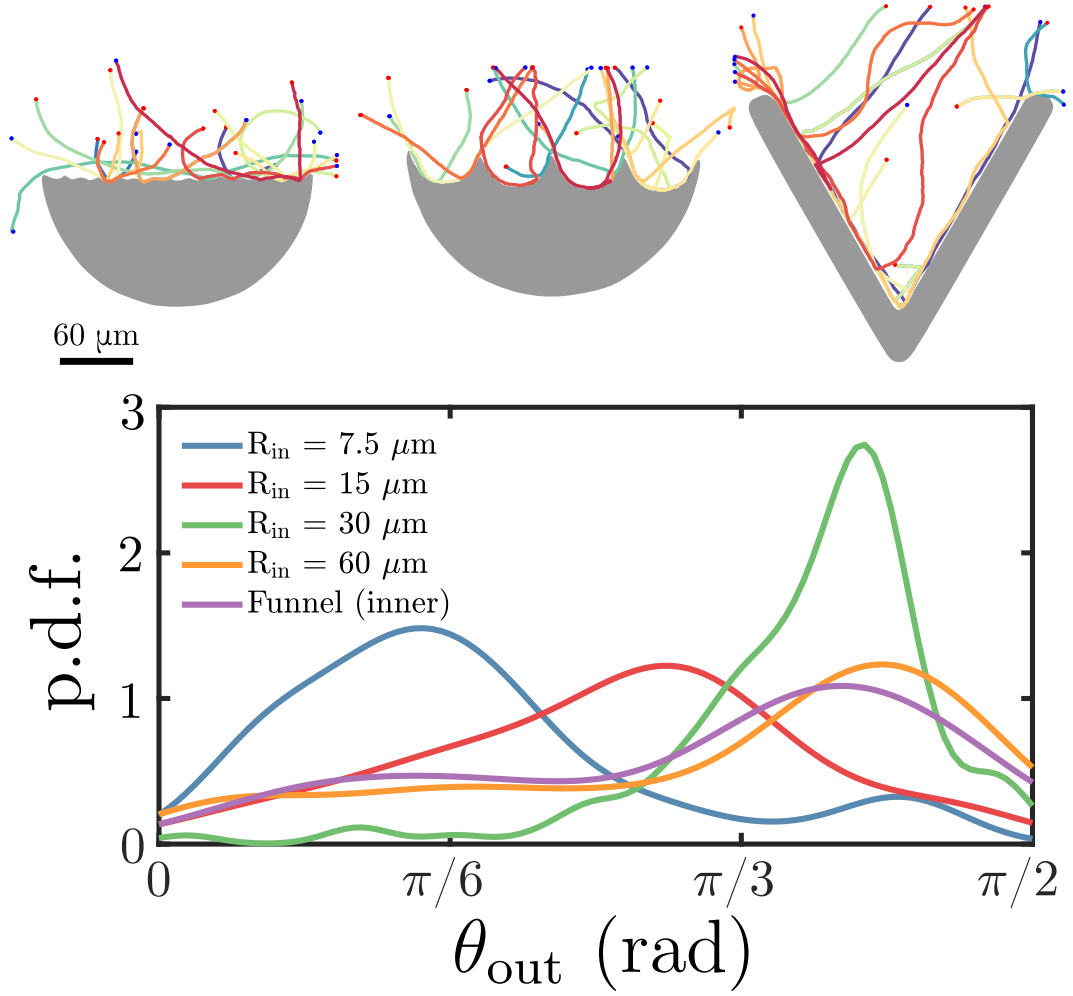


Figure 6.5: Top: sample *E. coli* trajectories for three types of ratchets ( $R_{in} = 7.5, 30 \mu\text{m}$  and funnel left to right). Bottom: probability distribution function of the angle  $\theta_{out}$  at which bacteria depart the ratchet surface when they undergo re-orientation. The p.d.f. curves were obtained by fitting a kernel density estimation to the respective histograms.

exception of the case where  $R_{in}$  at the angular distribution is centred below  $\pi/6$ , clearly indicating that bacteria leave the surface of the ratchet almost parallel to it (i.e. no re-orientation effect is present), as clearly visible from the trajectories shown in Fig.6.5.

## 6.4 Numerical Simulation

To further analyse ratchet properties and confirm our experimental results, we developed a simple numerical simulation to study the system. In this simulation,

each bacteria is modelled as an Active Brownian Particle (ABP) which obeys the equations of motion:

$$\begin{aligned}\frac{d}{dt}x &= v \cos(\phi) + \sqrt{2D_T}W_x, \\ \frac{d}{dt}y &= v \sin(\phi) + \sqrt{2D_T}W_y, \\ \frac{d}{dt}\phi &= \sqrt{2D_R}W_\phi,\end{aligned}\tag{6.1}$$

where  $x$ ,  $y$  and  $\phi$  represent the position of the particle and its orientation,  $v$  its velocity and  $D_r$  and  $D_t$  its translational and rotational diffusion coefficients. The  $W$  factors represent independent white noise processes [94].

Simulation parameters were chosen to correctly capture the typical swimming velocity of *E. coli* and the smooth swimming nature of the bacteria strain used in the experiments reported in this chapter, which is controlled by the  $D_r$  parameter [95].

Simulation Parameter	Value
$v$	20 $\mu\text{m/s}$
$D_t$	0.01 $\mu\text{m}^2/\text{s}$
$D_r$	0.05 $\text{rad}^2/\text{s}$

Table 6.1: Parameter values used in the numerical simulations presented in Fig. 6.7 .

In the simulation, when bacteria reach the surface of one the obstacles, they immediately change orientation to one that is parallel to the surface at the point of contact with the obstacle, similarly to previously reported simulations [87, 94].

The algorithm that deals with obstacle interactions is implemented as follows (see Fig. 6.6):

1. update the particle positions according to Eq. 6.1;
2. check if the new particle position is inside any of the obstacles;
3. if the particle isn't in an obstacle, move on to next timestep;
4. if the particle is in the obstacle, then
  - (a) find the line between the proposed updated position  $[\tilde{x}_{t+1} \ \tilde{y}_{t+1}]$  and the previous position  $[x_t \ y_t]$
  - (b) determine where the line meets the obstacle, and set those coordinates as the updated position  $[\tilde{x}_{t+1} \ \tilde{y}_{t+1}]$

- (c) find the tangent angle to the obstacle curve at the point  $[\tilde{x}_{t+1} \tilde{y}_{t+1}]$  and update the angle  $\phi_{t+1}$  accordingly

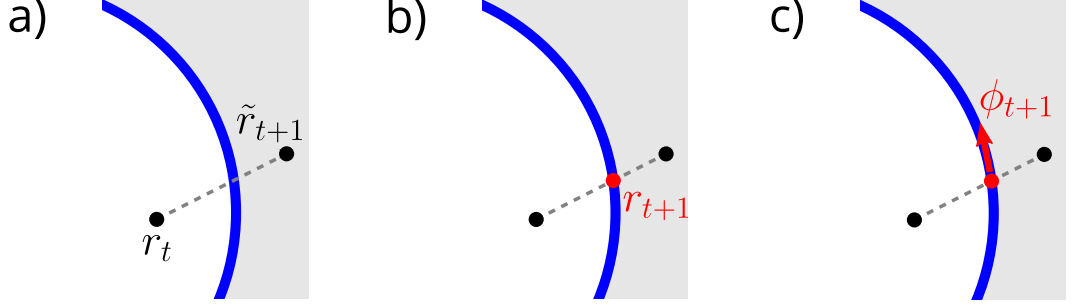


Figure 6.6: Visual representation of the scattering algorithm employed in the numerical simulations.

While not being completely accurate as hydrodynamics forces are completely neglected in this case and steric interactions are simplified significantly, we do believe the simulation offers some insight in the expected behaviour of the device and can confirm our results in showing that bacteria rectification can indeed be optimized by using curved geometries, as opposed to funnels.

Chamber geometries for the simulations were extracted from the schematic files used to produce the microfluidic devices. We do not include the ratchet geometries with  $R_{\text{in}} = 7.5\mu\text{m}$  because as mentioned, in our experiments those geometries are more similar to a flat wall than a circular funnel and thus they would not be represented correctly by our “boundary-following” model.

Results show that even in the simulation, the funnel geometry is the worst performing one (Fig. 6.7), and that the ratchet with  $R_{\text{in}} = 15$ ,  $R_{\text{in}} = 60$  is the best performing one. This confirms our experimental results, showing that bacteria rectification devices can make use of circular geometries to improve the rate at which they concentrate bacteria as well their overall effect.

We point out that concentration ratios in the simulation are higher than those measured in the experiments, but that can easily be explained by highlighting a few differences between the simulated “ideal” system and the experimental one. First of all, in the simulation bacteria can’t get stuck to surfaces (occasionally observed in the experiments), leading to much faster re-orientation times; secondly, once bacteria reach the ratchet boundary they follow it completely: this means their  $\theta_{\text{out}}$  distributions are centred closer to  $\pi/2$  and narrower which also increases the efficiency of the ratchets.

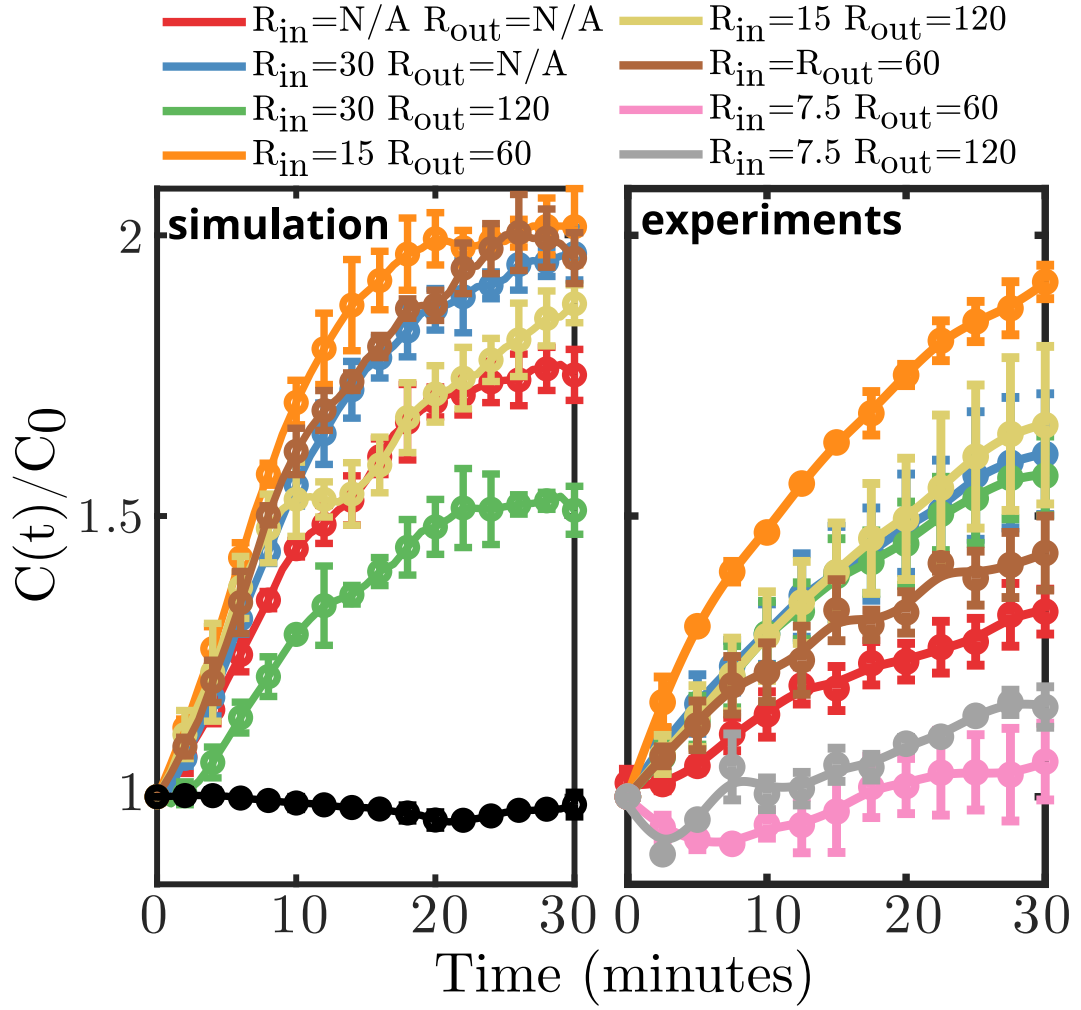


Figure 6.7: Left: Concentration curves from the numerical simulation in which the experiments were reproduced. Each line is the average from 5 simulation runs. The black line represents a “control” simulation in which no ratchets are present in the chamber. Right: experimental results (Fig. 6.2) - added here to allow the reader to compare better.

## 6.5 Conclusions

In this chapter we studied how microfluidic devices designed to rectify bacterial motion can be optimised by varying the geometry of the ratchets responsible for motion rectification.

We showed that circular ratchets perform better than previously studied V-shaped “funnel” ones, due to the reduced bacteria trapping and reduced re-orientation time. We furthered this analysis by performing experiments in which the radius of the curved ratchets was changed, showing that ratchets with radius  $7.5 \mu\text{m}$  are the best

performing ones. Moreover, we show that reducing the radius below this value can lead to negative effects such as bacteria trapping, increased residence time or poor scattering angles.

Lastly, we corroborate our results by developing a numerical simulation through which the experiments are repeated *in silico* with similar findings.

## Chapter 7

# Bull Sperm Thermotaxis

### 7.1 Introduction

On their way to the egg, spermatozoa are known to be “steered” by external factors such as temperature (thermotaxis) or chemical (chemotaxis) gradients and fluid flows (rheotaxis) [4].

However, despite recent experimental efforts which have confirmed the presence of temperature gradients in the oviducts of many mammals and sperm’s thermotactic response to them, much remains to be found out about sperm thermotaxis [9, 50]. For example, while proving that bull sperm does indeed concentrate at higher temperature regions of a gradient, Mondal *et al.* performed their experiments using a setup which did not allow live imaging of sperm cells navigating the temperature gradient [55]. Therefore, no information is available to help us understand how rapidly sperm navigate to the warmer region.

Similarly, no experiments have been carried out to understand how sperm motility changes as external temperature is increased since the early experiments of Rikmenspoel (1984) which were limited in scope by the technology available at the time [40]. This also leaves a gap in the literature regarding how bull sperm motility changes with temperature (though we highlight that the same can be said for other mammalian sperm such a human).

Nevertheless, through a careful analysis of the literature it is possible to highlight some common properties of mammalian sperm thermotaxis. For example, only sperm cells which can be capacitated will respond to the gradient (i.e. be thermotactic). The number of such cells in a given sample varies depending on species, with human sperm samples having 10-20% thermotactic cells and bull sperm samples 30-50% [9, 96].



In this chapter, we set out to expand on the already published results by using modern imaging and analysis techniques as well as a different experimental approach which allows us to live image sperm cells as they navigate the gradient.

Through this improved approach we are able to carry out a detailed study of sperm motility in temperatures ranging from 25 to 40°C, and report a previously unreported sperm behaviour at higher temperatures. Furthermore, we are able to study flagella waveforms at different temperatures in detail to understand better the origin of this novel phenomenon.

Lastly, thanks to the use of microfluidics we are able to image the sperm after setting up the gradient - this allows us to obtain a detailed curve for sperm accumulation at higher temperatures, with results aligning with previously published ones for other mammalian sperm cells. We also show that thermotaxis is a reversible process, indicating that temperature gradients could be used to modulate sperm concentration over time.

## **7.2 Experimental Details**

### **7.2.1 Sperm Preparation**

Bull sperm straws were thawed and prepared as outlined in the methodology section. In particular, the sperm samples used in this work were sorted using Cytoswim's microfluidics device (see Methodology for more details). This method was chosen over the sperm washing method as the experiments did not require a large volume of sample to be set up (15-20  $\mu\text{L}$ ) but did instead benefit from being performed with high motility cells so that effects could be studied in detail, without non-motile cells complicating image processing.

### **7.2.2 Experimental Setup**

A schematic of the experimental setup used to generate the temperature gradient can be found in Fig. 7.1. Two Indium-tin-oxide (ITO) coated glass slides were connected to an ARDUINO device for which a custom PID Controller LabVIEW script was written. The PID Controller allowed us to control the temperature of each slide independently, and made sure temperatures would stay constant during the experiment.

We then designed a microfluidics device which would consist of two chambers located on each of the ITO slides (i.e. at the two constant temperatures) connected by a channel in which a temperature gradient could be found.

As measuring temperature at the microscale is a challenging task, we simulated the experimental setup in Fusion365 (Autodesk). In the simulation, we look at how the temperature of a glass coverslip placed over the two ITO slides changes once we set them to have different, uniform temperatures (Fig. 7.1).

While the simulations are obviously no substitute for experimental confirmation,

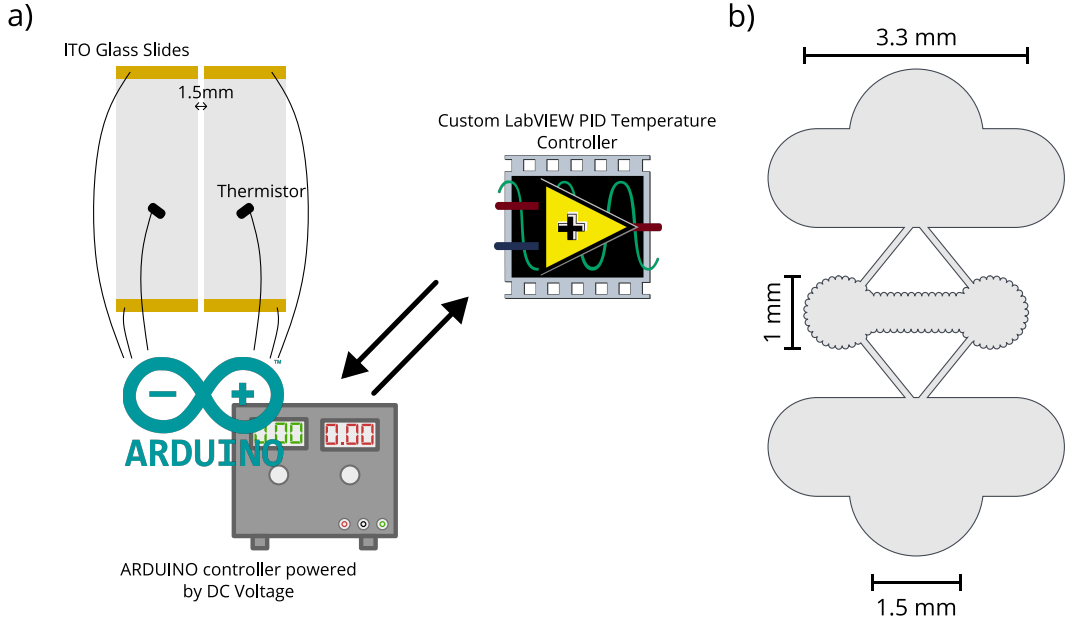


Figure 7.1: a) A schematic of the experimental setup used for the experiments reported in this chapter. b) The microfluidics device used to perform the experiments, the inlets are located in the top and bottom chambers, which are also later plugged with unpolymerised PDMS.

we believe they offer us enough reassurance the gradient is generated. This is further confirmed by the results later reported in the chapter.

Another point of concern for the reader might be whether the temperature of a heated up ITO slide is uniform, and if the thermistor readings (the key element of our PID controller) can be relied upon.

The answer to the first concern is - unfortunately - negative. ITO slides will have a slightly non-uniform temperature, with the sides (where the voltage is applied) being up to 1-1.5 °C warmer than the middle region for our configuration. It is however important to remember that the PID Controller will ensure the temperature of the thermistor (i.e. that of the region where it is placed) is the desired one.

Hence, by placing the thermistors as close as possible to where the microfluidics device will be placed, we can rely on the temperature being the desired one.

Another point of concern, as previously mentioned, might be whether the thermis-

tors used can be relied upon. To confirm this, we tested the plates while measuring the temperature simultaneously with multiple thermometers to confirm the thermistors are indeed calibrated correctly.

### 7.2.3 Device Preparation and Imaging Details

PDMS microfluidics devices were prepared as described in the methodology section. The device (Fig. 7.2) consists of two 1 mm circular chambers connected by a rectangular channel. It is 50  $\mu\text{m}$  tall and features concavities in the walls to ensure sperm does not accumulate on them, but stays in the bulk.

The device was first filled with a buffer consisting of Tryladyl and 0.2% BSA (bovine serum albumin) and then with the sample extracted from the microfluidics sorting device, also filled with the same buffer. The presence of BSA in the buffer reduces the chances of sperm cells getting stuck on the glass or PDMS surfaces.

Lastly, the two reservoirs were filled with unpolymerised PDMS to eliminate any bias due to sperm swimming from them to the circular chambers during the experiment.

After that, the device was placed on the two ITO slides ensuring that each of the two circular chamber ends would be aligned with the edge of the ITO slides. This way, it was possible to generate a temperature gradient between them, while keeping the temperature in the circular chambers uniform. Microscopy was performed on

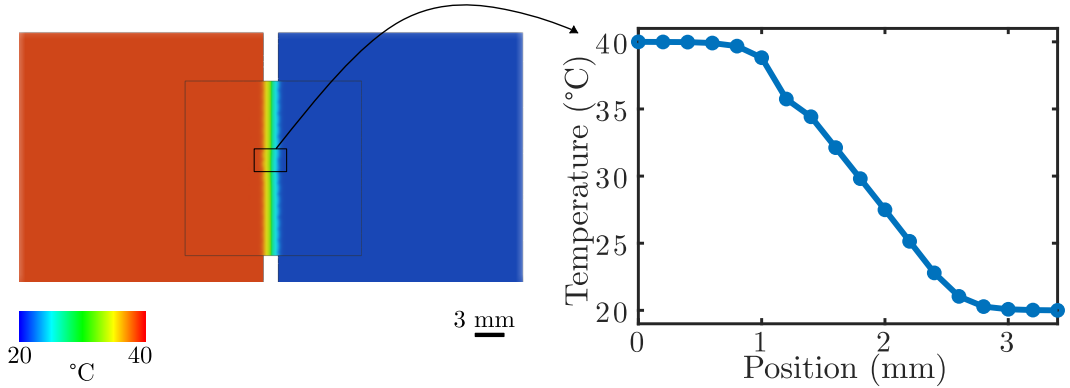


Figure 7.2: Right: Heatmap obtained from the heat diffusion simulations outlined in the text. Left: Temperature profile of the coverslip surface in the region between the two ITO slides.

a Nikon Eclipse inverted microscope. Depending on the focus of the experiments (flagella and motility analysis, accumulation over time), different imaging procedures were followed.

For long time-scale experiments, darkfield imaging was performed using a 2x objective (Nikon, 0.06 NA). Short image sequences (150 frames) were acquired every 10 minutes using a 2048x2048 CCD USB3 Pointgrey Camera recording at 10 fps. Experiments lasted 90 minutes to allow sperm to navigate from one chamber to the other.

Experiments concerned with the detailed analysis of the motility of bull sperm at different temperatures were performed using a Ph1 Phase Contrast 20x Nikon Objective combined with a 1.5x magnifier (30x total magnification) which allowed for clear visualisation of the sperm flagella. High-speed imaging was achieved through an Edgertronic camera recording 992x992px frames at 150fps for up to 10s. Image processing was performed using similar methods to those outlined in previous chapters, in particular Chapter 5. Flagella analysis was also performed using the methods previously mentioned in Chapter 5.

## 7.3 Results

### 7.3.1 Sperm Motility as a function of Temperature

To gain an understanding of any phenomena which may arise when sperm navigates temperature gradients, we started our investigation by studying how sperm behaves in an environment of homogeneous temperature as that temperature is increased. From an analysis of the swimming velocity, it is possible to identify two regimes as the temperature increases (Fig. 7.3): from 25 to 32 °C the velocity increases; whereas a sharp drop is seen afterwards with the velocity reaching a minima at 37.5 °C. Note that swimming velocity is defined in this chapter as the average path velocity (VAP in CASA systems, i.e. the swimming velocity calculated from the average trajectory traced by head displacements over time) but the same trend is observed in the curvilinear velocity (VCL) [97].

Interestingly, another consequence of the increase in temperature is the emergence of circular trajectories (Fig. 7.4). In fact, as the temperature is increased, we start noticing the emergence of circular trajectories in the sample, until all sperm cells start swimming in a circular motion at 40°C .

The emergence of circular trajectories at higher temperatures could be a factor determining the emergence of thermotaxis: as sperm cells start tracing circular trajectories, the space they explore is reduced significantly, as the trajectories appear to be stable around a central point rather than spiral like as in the case of bacteria swimming near surfaces [98]. To delve deeper into how exactly the circular trajectories emergence, we use high speed data to analyse in detail the motion of sperm

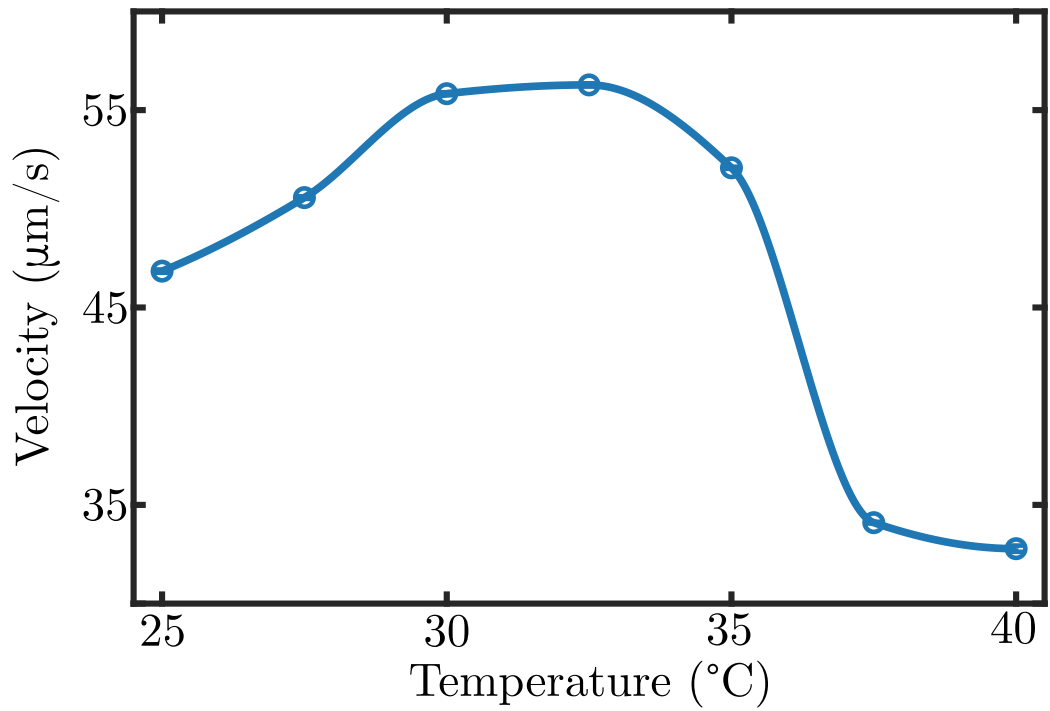


Figure 7.3: Temperature dependence of the average path velocity for bull sperm.

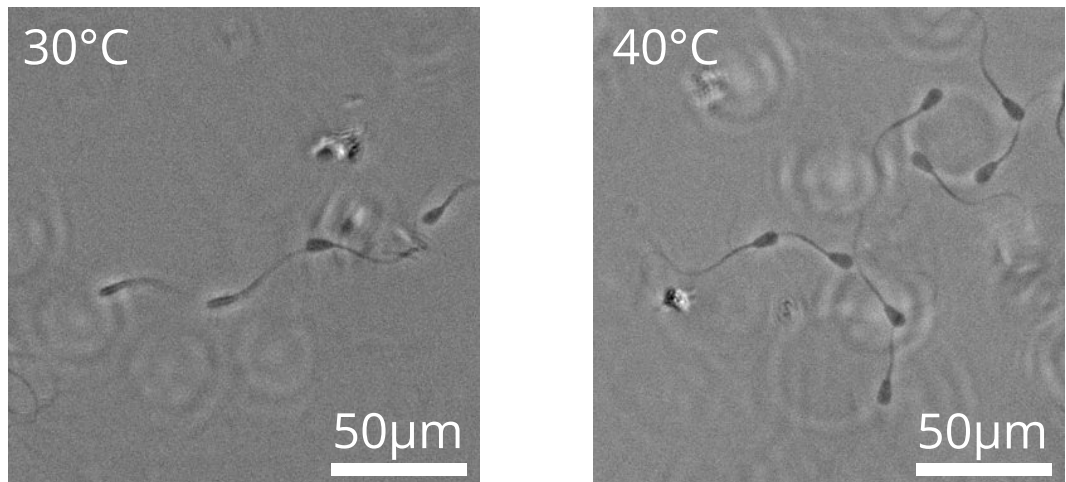


Figure 7.4: Sum of four frames taken 0.5 seconds apart of sperm cells swimming at (left) 30°C and (right) 40°C to highlight how the circular motion arises as the temperature is increased.

cells and their flagella dynamics as a function of temperature (Fig. 7.5a,b).

We start by analysing the radius of curvature of the average sperm trajectories as a function of temperature (Fig. 7.5c), which highlight how the trajectories become

more curved as the temperature of the surrounding environment is increased, ultimately leading to circular trajectories of small radius ( $\sim 20\mu\text{m}$ ).

Circular trajectories have been observed in sperm cells before, and have been shown to be a consequence of a change in swimming gait and increased flagellar curvature [99]. For this reason, we perform a similar analysis here to understand if the cause for circular trajectories is the same for sperm cells in high temperature environments.

To find the average flagellar curvature for a given sperm cells, we first trace flagellar beating for one second at 150fps and calculate the curvature at each point along the flagellum for all the timesteps. We then find the average curvature at each point for a 1s period, and from that calculate the overall average curvature of the flagellum. Results show that indeed the curvature of the flagellum increases for temperatures above  $30^\circ\text{C}$  (Fig. 7.6), reaching its highest point at  $40^\circ\text{C}$  (i.e lowest radius). This suggests that sperm changes its gait as the temperature of the surrounding environment rises, increasing the curvature of its flagellum and thus swimming in circular trajectories. We also find that the relationship between the curvature of the flag-

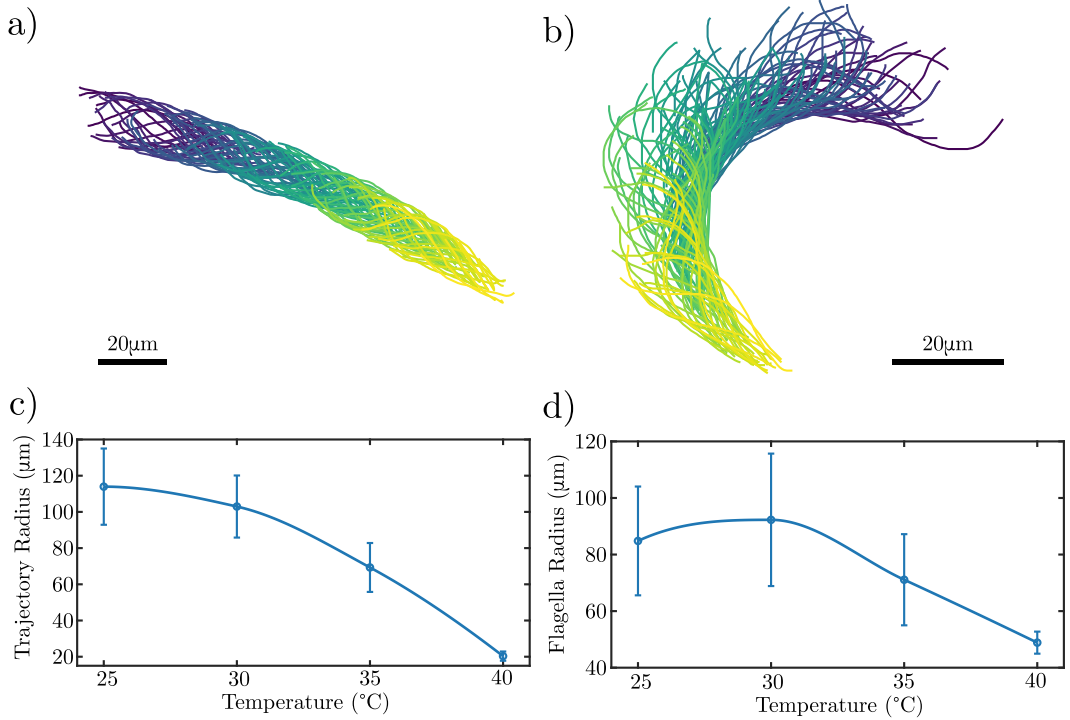


Figure 7.5: Top: Flagella shapes for sperm swimming at 25 (a) and 40 (b) °C (both trajectories are one second long). Bottom: radius of sperm trajectories (c) and average radius of sperm flagella (d) as a function of temperature.

ella and that of the associated trajectories is well captured by a linear relationship. This is consistent with results published by Friedrich *et al.*, who showed that circular trajectories in sperm cells arise from the anisotropy of the flagellar beat and an increased curvature through a combination of high-speed microscopy and resistive force theory calculations [99].

The asymmetry of the flagellar beat has its roots in the architecture of the sperm flagellum and in the activity of the molecular motors within it. This suggests that any increase in flagellar curvature is caused by active processes, as curved trajectories have also been shown to be how sperm responds to chemical gradients in sea urchin [100]. It is therefore possible that the mechanisms might operate in very similar ways as they would normally be found operating in tandem to allow sperm to navigate through the reproductive tract in search for the egg.

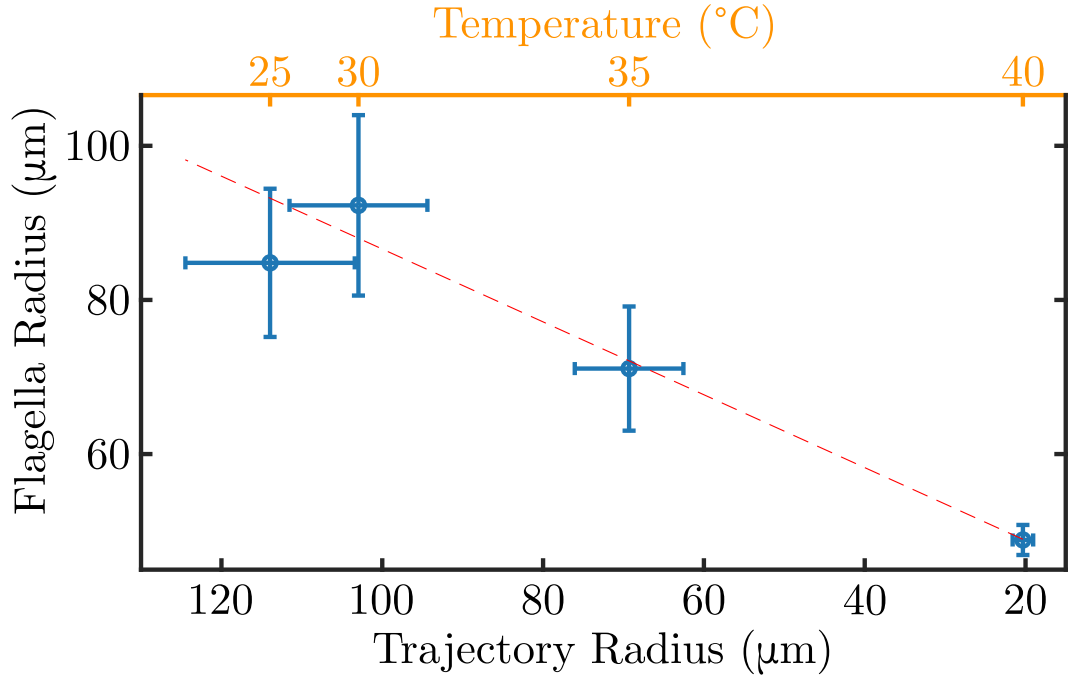


Figure 7.6: The linear trajectory between sperm trajectory radius and the corresponding flagellar radius. Top x-axis is the temperature at which the data was collected. In red, dashed, is a linear fit obtained by linear regression to account for errors in both axes.

### 7.3.2 Sperm Thermotaxis

After analysis the motion of sperm in region of homogeneous temperatures, we turned our attention to the behaviour of sperm in temperature gradients (Fig. 7.1).

We analysed four different types of gradients, and observed how the concentration of sperm cells in the two chambers would vary over a 90 minute period of time. At the start of each experiment, the ratio between the number of cells in the high temperature region and low temperature region  $C_{\text{high}}/C_{\text{low}}$  would be  $\sim 1$ . Results

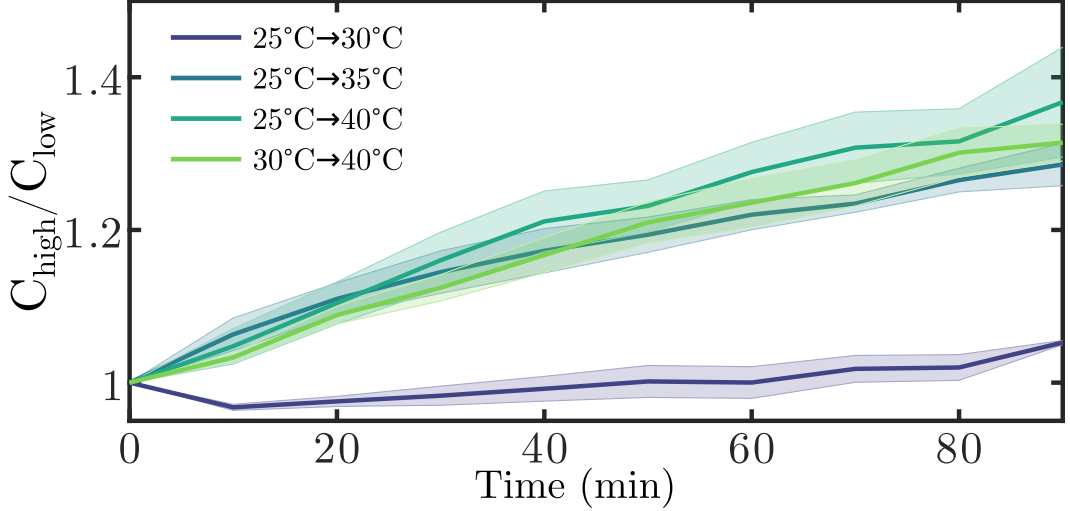


Figure 7.7: Time evolution of the ratio between sperm cells in the high and low temperature regions for the four different types of gradients used to study bull sperm thermotaxis. Shaded areas indicate errors. Each line is the average of three different experiments.

showed that bull sperm does indeed concentrate in the high temperature region of the device. In particular, the effect appeared to be minimal for the gradient between 25 and 30°C while for all the other gradients studied, the thermotactic effect was measured to be equal, with sperm concentration in the high temperature region being 30% higher at the end of the measuring period.

These results are found to be in line with previously published work on thermotaxis of human and mouse sperm, in which the net migration of sperm cells due to the temperature gradients was measured to be in the same range.

The small percentage of sperm cells accumulating in higher temperature regions is consistent with the number of cells which are expected to be responsive in a sample. In fact, it has been shown that only capacitated sperm cells are thermotactic (i.e. respond to temperature gradients) [9], and the fraction of sperm cells found to be capacitated in bull sample has been found to be in the 30-50% range [96].

Interestingly, we only see a small effect for the gradient 25-30°C. No data is available for bull sperm thermotaxis in this temperature range, but reports have shown that human sperm is thermotactic in the range between 29 and 41°C.



Our results suggest that the same, or similar, might be true for bull sperm. The small concentration increase in the 30°C chamber could then be explained by assuming that only sperm in the closest part of the connecting channel navigate and concentrate there, with the rest of the sperm swimming at temperatures below 29°C remaining unaffected.

Note that in our experiments sperm cells were not allowed to pre-capacitate before the gradient was set up, while in the other experiments mentioned pre-capacitation was allowed. This suggests that the thermotactic effect could have been slightly increased and sped up with previous capacitation (see next paragraphs and Fig. 7.8). Experiments were also performed to understand whether the thermotactic effect can be reversed. In an example experiment shown in Fig. 7.8, the gradient direction was reversed after ~25 minutes and sperm were observed concentrating in the opposite direction (i.e. they followed the gradient reversal). Such experiment suggest sperm do not have “memory” of the gradient, but simply follow the temperature changes as perceived during motion. Interestingly, the effect following temperature reversal

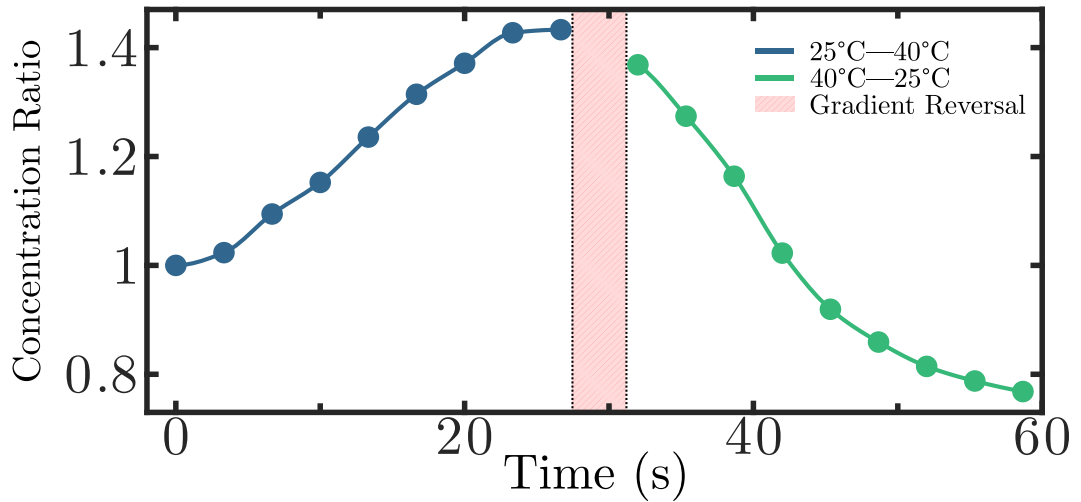


Figure 7.8: Concentration ratio curve for an experiment in which the gradient was reversed after 30 minutes. Results show that sperm moves towards the high temperature region in both cases, with a slight increase after the reversal - potentially due to capacitation. The gradient reversal area indicates the time during which the ITO covered slides change temperatures and reach the new desired ones.

is higher than the original effect. This suggests that pre-capacitation does indeed improve results and could have been used to increase the concentration of sperm cells in our gradient experiments.

## 7.4 Conclusions

In this chapter we have carried out an investigation to understand how bull sperm cells behave as a function of temperature. Furthermore, we were able to use microfluidics to study how thermotaxis occurs in bull sperm.

Results show that swimming velocity follows two regimes when temperature is increased: an increase for temperatures between 25 and 32.5°C and a decrease for temperatures higher than that, plateauing at  $\sim 37.5^\circ\text{C}$ .

An interesting feature of bull sperm motility which arises as the temperature of the surrounding environment is increased is circular trajectories. In fact, for temperatures above 35°C we see sperm cells swimming in circular trajectories. These trajectories get tighter as temperature is increased, with a radius of  $20\mu\text{m}$  for sperm cells swimming at 40°C. Most importantly, we find the centre of the circles traced by sperm to be stable in time (i.e. sperm cells are not swimming in spiral trajectories, but rather stay in one stable trajectory).

We use high speed imaging to obtain detailed data of the flagellar motility of sperm cells as the temperature is increased to gain an understanding of this phenomenon. Analysing the flagellar waveforms we find that circular trajectories arise as a consequence of increased curvature (i.e. bending) of the flagella as the temperature is increased (due to the internal processes which control how flagella is moved). Furthermore, we find there to be an approximately linear relationship between the curvature of the flagellar beat and the curvature of the corresponding trajectory generated by it, in line with resistive force theory predictions made by Friedrich *et al.* [99].

We then measured how sperm concentration changes in time when sperm are placed in a region of inhomogeneous temperature. For all temperature gradients studied we measured a concentration increase of  $\sim 40\%$  in the high temperature region (in line with the number of capacitated cells usually found in a sample), with the exception of the gradient 25-30°C likely due to the temperature being too low to capacitate the sperm.

Lastly, we performed experiments to investigate how sperm responds to a temperature gradient being reversed, showing that thermotaxis can be reversed to concentrate sperm in different regions, also indicating that sperm thermotaxis is caused by instant response to the gradient.

## Chapter 8

# Conclusions

In this thesis, we have studied the behaviour of a diverse range of biological microswimmers under the influence of various external stimuli, from viscosity and temperature gradients to mechanical obstacles.

Through this analysis we were able to draw conclusions which can be useful to understand many natural phenomena involving microswimmers as well as develop microfluidics devices which could be used as bioengineering tools.

We conclude the thesis with a recap of the major findings from each chapter:

- In **Chapter 4** we carried out a study of the behaviour of the green alga *Chlamydomonas reinhardtii* (CR) as it navigates sharp viscosity gradients. We showed that the motility of CR is severely hindered by an increase in viscosity of the surrounding environment, with the swimming velocity reduction effect being dependent on the flagellar length of the algae. We then analysed the trajectories of algae approaching the interface, showing that CR scatter off it when swimming from the low viscosity region to the high viscosity one if they approach the interface at a small angle, due to a torque imbalance caused by the two flagella being in different viscosity media. We concluded our study by measuring how the concentration of algae changes with time in environments of inhomogeneous viscosity, showing the unexpected result of algae concentrating in the low viscosity region, or maintaining a uniform concentration rather than concentrating in the high viscosity region (i.e. where they swim slower) as otherwise expected.
- In **Chapter 5** we performed similar experiments with ram sperm, a “pusher” microswimmer (as opposed to the “puller” CR). Contrary to CR, we show that sperm retains most of its swimming velocity even in high viscosity environments ( $\sim 60$  times the viscosity of water) by changing its swimming gait

and improving its swimming efficiency. Furthermore, we show that sperm is able to navigate the viscosity interface regardless of where it approaches it from. We conclude this is due to the difference in swimming gait between CR and sperm, mainly where the flagella are located in the body, as well as the difference in how the two microorganisms respond to the increased viscosity of the surrounding environment.

- In **Chapter 6** we turn our attention to how microfluidics devices can be developed to take advantage of certain microbial responses to external stimuli (in this case, obstacles and walls) to guide them. We develop a microfluidics device which allows us to rectify bacterial motion in a given direction through the use of specially designed obstacles. We perform experiments showing that the rectifying effect can be improved by using circular ratchets of small radius, also highlighting how small such radius can be before issues such as trapping start arising. In particular, we show how both residence time on the obstacle and the angle at which the microswimmers depart it affect performance. These results are then further confirmed through numerical simulations.
- In **Chapter 7** we analyse how the motility of bull sperm is affected by the temperature of the surrounding environment. We show that at high temperatures ( $> 35^{\circ}\text{C}$ ) bull sperm starts swimming in circular trajectories. We then performed a detailed study of flagellar motility as a function of temperature using high speed imaging. Through this analysis we show that circular trajectories arise from a change in gait at higher temperature, in which the bend and asymmetry of the flagella is increased, thus leading to circular trajectories being formed. Lastly, we perform experiments showing that bull sperm performs thermotaxis, and that thermotaxis can be reversed (i.e. sperm concentration can be changed over time by manipulating the gradient).

# Bibliography

- [1] K. Son, D. R. Brumley, and R. Stocker, “Live from under the lens: exploring microbial motility with dynamic imaging and microfluidics,” *Nature Reviews Microbiology*, vol. 13, pp. 761–775, Nov. 2015.
- [2] J. Elgeti, R. G. Winkler, and G. Gompper, “Physics of microswimmers - Single particle motion and collective behavior: A review,” *Reports on Progress in Physics*, vol. 78, no. 5, 2015.
- [3] G. H. Wadham and J. P. Armitage, “Making sense of it all: bacterial chemotaxis,” *Nature Reviews Molecular Cell Biology*, vol. 5, pp. 1024–1037, Dec. 2004.
- [4] M. Eisenbach and L. C. Giojalas, “Sperm guidance in mammals — an unpaved road to the egg,” *Nature Reviews Molecular Cell Biology*, vol. 7, pp. 276–285, Apr. 2006.
- [5] J. Arrieta, A. Barreira, M. Chioccioli, M. Polin, and I. Tuval, “Phototaxis beyond turning: persistent accumulation and response acclimation of the microalga *chlamydomonas reinhardtii*,” *Scientific Reports*, vol. 7, June 2017.
- [6] V. Kantsler, J. Dunkel, M. Blayney, and R. E. Goldstein, “Rheotaxis facilitates upstream navigation of mammalian sperm cells,” *eLife*, vol. 3, p. e02403, 2014.
- [7] Marcos, H. C. Fu, T. R. Powers, and R. Stocker, “Bacterial rheotaxis,” *Proceedings of the National Academy of Sciences*, vol. 109, pp. 4780–4785, Mar. 2012.
- [8] J. Park, D.-H. Kim, and A. Levchenko, “Topotaxis: A new mechanism of directed cell migration in topographic ECM gradients,” *Biophysical Journal*, vol. 114, pp. 1257–1263, Mar. 2018.

- [9] A. Bahat, S. R. Caplan, and M. Eisenbach, “Thermotaxis of human sperm cells in extraordinarily shallow temperature gradients over a wide range,” *PLoS ONE*, vol. 7, p. e41915, July 2012.
- [10] R. Rusconi, M. Garren, and R. Stocker, “Microfluidics expanding the frontiers of microbial ecology,” *Annual Review of Biophysics*, vol. 43, pp. 65–91, May 2014.
- [11] J. S. Guasto, K. A. Johnson, and J. P. Gollub, “Oscillatory flows induced by microorganisms swimming in two dimensions,” *Physical Review Letters*, vol. 105, Oct. 2010.
- [12] T. Chinnasamy, J. L. Kingsley, F. Inci, P. J. Turek, M. P. Rosen, B. Behr, E. Tüzel, and U. Demirci, “Guidance and self-sorting of active swimmers: 3d periodic arrays increase persistence length of human sperm selecting for the fittest,” *Advanced Science*, vol. 5, p. 1700531, Dec. 2017.
- [13] C. Bechinger, R. Di Leonardo, H. Löwen, C. Reichhardt, G. Volpe, and G. Volpe, “Active particles in complex and crowded environments,” *Reviews of Modern Physics*, vol. 88, no. 4, 2016.
- [14] E. Lauga and T. R. Powers, “The hydrodynamics of swimming microorganisms,” *Reports on Progress in Physics*, vol. 72, p. 096601, Aug. 2009.
- [15] E. M. Purcell, “Life at low reynolds number,” *American Journal of Physics*, vol. 45, pp. 3–11, Jan. 1977.
- [16] S. Kim and S. J. Karrila in *Microhydrodynamics*, Butterworth-Heinemann, 1991.
- [17] K. Drescher, R. E. Goldstein, N. Michel, M. Polin, and I. Tuval, “Direct measurement of the flow field around swimming microorganisms,” *Physical Review Letters*, vol. 105, p. 168101, 2010.
- [18] K. Drescher, J. Dunkel, L. H. Cisneros, S. Ganguly, and R. E. Goldstein, “Fluid dynamics and noise in bacterial cell-cell and cell-surface scattering,” *Proceedings of the National Academy of Sciences of the United States of America*, vol. 108, pp. 10940–10945, 2011.
- [19] T. J. Pedley and J. O. Kessler, “Hydrodynamic phenomena in suspensions of swimming microorganisms,” *Annual Review of Fluid Mechanics*, vol. 24, pp. 313–358, Jan. 1992.

- [20] K.-T. Wu, Y.-T. Hsiao, and W.-Y. Woon, “Entrapment of pusher and puller bacteria near a solid surface,” *Physical Review E*, vol. 98, Nov. 2018.
- [21] V. Kantsler, J. Dunkel, M. Polin, and R. E. Goldstein, “Ciliary contact interactions dominate surface scattering of swimming eukaryotes,” *Proceedings of the National Academy of Sciences*, vol. 110, pp. 1187–1192, Jan 2013.
- [22] R. Jeanneret, M. Contino, and M. Polin, “A brief introduction to the model microswimmer *Chlamydomonas reinhardtii*,” *European Physical Journal: Special Topics*, vol. 2156, pp. 2141–2156, 2016.
- [23] M. Polin, I. Tuval, K. Drescher, J. P. Gollub, and R. E. Goldstein, “*Chlamydomonas* Swims with Two “Gears” in a Eukaryotic Version of Run-and-Tumble Locomotion,” *Science*, vol. 325, pp. 487–490, 2009.
- [24] P. Hegemann and B. Bruck, “Light-induced stop response in *Chlamydomonas reinhardtii*: Occurrence and adaptation phenomena,” *Cell Motility and the Cytoskeleton*, vol. 14, no. 4, pp. 501–515, 1989.
- [25] H. C. Berg and D. A. Brown, “Chemotaxis in *Escherichia coli* analysed by three-dimensional tracking,” *Nature*, vol. 239, pp. 500–504, Oct. 1972.
- [26] N. C. Darnton, L. Turner, S. Rojevsky, and H. C. Berg, “On torque and tumbling in swimming *Escherichia coli*,” *Journal of Bacteriology*, vol. 189, pp. 1756–1764, Mar. 2007.
- [27] H. C. Berg, “The rotary motor of bacterial flagella,” *Annual Review of Biochemistry*, vol. 72, pp. 19–54, June 2003.
- [28] A. J. Wolfe, M. P. Conley, T. J. Kramer, and H. C. Berg, “Reconstitution of signaling in bacterial chemotaxis,” *Journal of Bacteriology*, vol. 169, pp. 1878–1885, May 1987.
- [29] C. B. Lindemann and K. A. Lesich, “Functional anatomy of the mammalian sperm flagellum,” *Cytoskeleton*, vol. 73, pp. 652–669, Oct. 2016.
- [30] *Anatomy and Physiology II*. Lumen, 2021. [Online; accessed 2021-08-24].
- [31] K. Ishimoto, H. Gadêlha, E. A. Gaffney, D. J. Smith, and J. Kirkman-brown, “Human sperm swimming in a high viscosity mucus analogue,” *Journal of Theoretical Biology*, vol. 446, pp. 1–10, 2018.

- [32] D. J. Smith, E. A. Gaffney, H. Gadêlha, N. Kapur, and J. C. Kirkman-Brown, “Bend propagation in the flagella of migrating human sperm, and its modulation by viscosity,” *Cell Motility and the Cytoskeleton*, vol. 66, pp. 220–236, Apr. 2009.
- [33] B. Qin, A. Gopinath, J. Yang, J. P. Gollub, and P. E. Arratia, “Flagellar kinematics and swimming of algal cells in viscoelastic fluids,” *Scientific Reports*, vol. 5, pp. 1–7, 2015.
- [34] S. Camalet and F. Jülicher, “Generic aspects of axonemal beating,” *New Journal of Physics*, vol. 2, no. 24, pp. 0–23, 2000.
- [35] M. Bottier, K. A. Thomas, S. K. Dutcher, and P. V. Bayly, “How does cilium length affect beating?,” *Biophysical Journal*, vol. 116, pp. 1292–1304, 2019.
- [36] K. S. Wilson, O. Gonzalez, S. K. Dutcher, and P. V. Bayly, “Dynein-deficient flagella respond to increased viscosity with contrasting changes in power and recovery strokes,” *Cytoskeleton*, vol. 72, pp. 477–490, Sept. 2015.
- [37] R. P. Jansen, “Cyclic changes in the human fallopian tube isthmus and their functional importance,” *American Journal of Obstetrics and Gynecology*, vol. 136, pp. 292–308, Feb. 1980.
- [38] J. Kremer, “A simple sperm penetration test.,” *International journal of fertility*, vol. 10, pp. 209–215, 1965.
- [39] K. Ishimoto, H. Gadêlha, E. A. Gaffney, D. J. Smith, and J. Kirkman-Brown, “Human sperm swimming in a high viscosity mucus analogue,” *Journal of Theoretical Biology*, vol. 446, pp. 1–10, 2018.
- [40] R. Rikmenspoel, “Movements and active moments of bull sperm flagella as a function of temperature and viscosity,” *Journal of Experimental Biology*, vol. 108, pp. 205–230, Jan. 1984.
- [41] B. Liebchen, P. Monderkamp, B. Ten Hagen, and H. Löwen, “Viscotaxis: Microswimmer Navigation in Viscosity Gradients,” *Physical Review Letters*, vol. 120, p. 208002, 2018.
- [42] C. Datt and G. J. Elfring, “Active Particles in Viscosity Gradients,” *Physical Review Letters*, vol. 123, p. 158006, 2019.
- [43] P. Maggaretti, M. N. Popescu, and S. Dietrich, “Active colloids at fluid interfaces,” *Soft Matter*, vol. 12, no. 17, pp. 4007–4023, 2016.



- [44] A. J. Mathijssen, T. N. Shendruk, J. M. Yeomans, and A. Doostmohammadi, “Upstream swimming in microbiological flows,” *Physical Review Letters*, vol. 116, Jan. 2016.
- [45] L. Rothschild, “Non-random distribution of bull spermatozoa in a drop of sperm suspension,” *Nature*, vol. 198, pp. 1221–1222, June 1963.
- [46] P. Galajda, J. Keymer, P. Chaikin, and R. Austin, “A wall of funnels concentrates swimming bacteria,” *Journal of Bacteriology*, vol. 189, pp. 8704–8707, Sept. 2007.
- [47] J. Tailleur and M. E. Cates, “Sedimentation, trapping, and rectification of dilute bacteria,” *EPL (Europhysics Letters)*, vol. 86, p. 60002, June 2009.
- [48] M. Mijalkov and G. Volpe, “Sorting of chiral microswimmers,” *Soft Matter*, vol. 9, no. 28, p. 6376, 2013.
- [49] M. Zaferani, S. H. Cheong, and A. Abbaspourrad, “Rheotaxis-based separation of sperm with progressive motility using a microfluidic corral system,” *Proceedings of the National Academy of Sciences*, vol. 115, pp. 8272–8277, July 2018.
- [50] M. Eisenbach, S. Cerezales, and S. Boryshpolets, “Behavioral mechanisms of mammalian sperm guidance,” *Asian Journal of Andrology*, vol. 17, no. 4, p. 628, 2015.
- [51] M. Sekiguchi, S. Kameda, S. Kurosawa, M. Yoshida, and K. Yoshimura, “Thermotaxis in chlamydomonas is brought about by membrane excitation and controlled by redox conditions,” *Scientific Reports*, vol. 8, Oct. 2018.
- [52] A. Paulick, V. Jakovljevic, S. Zhang, M. Erickstad, A. Groisman, Y. Meir, W. S. Ryu, N. S. Wingreen, and V. Sourjik, “Mechanism of bidirectional thermotaxis in escherichia coli,” *eLife*, vol. 6, Aug. 2017.
- [53] A. Bahat, M. Eisenbach, and I. Tur-Kaspa, “Periovulatory increase in temperature difference within the rabbit oviduct,” *Human Reproduction*, vol. 20, pp. 2118–2121, Apr. 2005.
- [54] R. H. F. Hunter and R. Nichol, “A preovulatory temperature gradient between the isthmus and ampulla of pig oviducts during the phase of sperm storage,” *Reproduction*, vol. 77, pp. 599–606, July 1986.

- [55] A. Mondal, Y. Takagi, S. A. Baba, and K. ichi Hamano, “Involvement of calcium channels and intracellular calcium in bull sperm thermotaxis,” *Journal of Reproduction and Development*, vol. 63, no. 2, pp. 143–148, 2017.
- [56] S. Venkatesan, J. Jerald, P. Asokan, and R. Prabakaran, “A comprehensive review on microfluidics technology and its applications,” in *Lecture Notes in Mechanical Engineering*, pp. 235–245, Springer Singapore, 2020.
- [57] E. H. Harris, *The Chlamydomonas Sourcebook*. Academic Press, Oxford, UK, 2009.
- [58] J. R. Seymour, T. MicAhmed, and R. Stocker, “A microfluidic chemotaxis assay to study microbial behavior in diffusing nutrient patches,” *Limnology and Oceanography: Methods*, pp. 477–488, 2008.
- [59] K. Schakenraad, L. Ravazzano, N. Sarkar, J. A. J. Wondergem, R. M. H. Merks, and L. Giomi, “Topotaxis of active Brownian particles,” *Physical Review E*, vol. 101, p. 032602, 2020.
- [60] J. N. Wilking, T. E. Angelini, A. Seminara, M. P. Brenner, and D. A. Weitz, “Biofilms as complex fluids,” *MRS Bulletin*, vol. 36, pp. 385–391, 2011.
- [61] J. R. Seymour, R. Simó, T. Ahmed, and R. Stocker, “Chemoattraction to dimethylsulfoniopropionate throughout the marine microbial food web,” *Science*, vol. 329, pp. 342–345, 2010.
- [62] G. S. Klindt, C. Ruloff, C. Wagner, and B. M. Friedrich, “In-phase and anti-phase flagellar synchronization by waveform compliance and basal coupling,” *New Journal of Physics*, vol. 19, p. 113052, 2017.
- [63] K. Y. Wan and R. E. Goldstein, “Coordinated beating of algal flagella is mediated by basal coupling,” *Proceedings of the National Academy of Sciences*, vol. 113, pp. E2784–E2793, 2016.
- [64] J. V. Herráez-Domínguez, F. G. G. de León, O. Díez-Sales, and M. Herráez-Domínguez, “Rheological characterization of two viscosity grades of methylcellulose: An approach to the modeling of the thixotropic behaviour,” *Colloid and Polymer Science*, vol. 284, no. 1, pp. 86–91, 2005.
- [65] C. Abaurrea-Velasco, T. Auth, and G. Gompper, “Vesicles with internal active filaments: self-organized propulsion controls shape, motility, and dynamical response,” *New Journal of Physics*, vol. 21, p. 123024, 2019.

- [66] E. L. Barnhart, K.-C. Lee, K. Keren, A. Mogilner, and J. A. Theriot, “An adhesion-dependent switch between mechanisms that determine motile cell shape,” *PLoS Biology*, vol. 9, p. e1001059, 2011.
- [67] M. Contino, E. Lushi, I. Tuval, V. Kantsler, and M. Polin, “Microalgae scatter off solid surfaces by hydrodynamic and contact forces,” *Physical Review Letters*, vol. 115, Dec. 2015.
- [68] E. Lushi, V. Kantsler, and R. E. Goldstein, “Scattering of biflagellate microswimmers from surfaces,” *Physical Review E*, vol. 96, p. 023102, 2017.
- [69] M. Mirzakhloo and M.-R. Alam, “Flow characteristics of chlamydomonas result in purely hydrodynamic scattering,” *Physical Review E*, vol. 98, p. 012603, 2018.
- [70] M. R. Stehnach, N. Waisbord, D. M. Walkama, and J. S. Guasto, “Viscophobic turning dictates microalgae transport in viscosity gradients,” *Nature Physics*, vol. 17, pp. 926–930, May 2021.
- [71] J. Arlt, V. A. Martinez, A. Dawson, T. Pilizota, and W. C. Poon, “Painting with light-powered bacteria,” *Nature Communications*, vol. 9, pp. 1–7, 2018.
- [72] G. Frangipane, D. Dell’Arciprete, S. Petracchini, C. Maggi, F. Saglimbeni, S. Bianchi, G. Vizsnyiczai, M. L. Bernardini, and R. Di Leonardo, “Dynamic density shaping of photokinetic *E. coli*,” *eLife*, vol. 7, p. e36608, 2018.
- [73] J. C. Kirkman-Brown and D. J. Smith, “Sperm motility: is viscosity fundamental to progress?,” *Molecular Human Reproduction*, vol. 17, pp. 539–544, June 2011.
- [74] A. Nsamela, P. Sharan, A. Garcia-Zintzun, S. Heckel, P. Chattopadhyay, L. Wang, M. Wittmann, T. Gemming, J. Saenz, and J. Simmchen, “Effect of viscosity on microswimmers: a comparative study,” *ChemNanoMat*, Apr. 2021.
- [75] B. J. Walker, K. Ishimoto, and R. J. Wheeler, “Automated identification of flagella from videomicroscopy via the medial axis transform,” *Scientific Reports*, vol. 9, Mar. 2019.
- [76] J. Hansen, S. Rassmann, J. Jikeli, and D. Wachten, “SpermQ—a simple analysis software to comprehensively study flagellar beating and sperm steering,” *Cells*, vol. 8, p. 10, Dec. 2018.

- [77] T.-W. Su, L. Xue, and A. Ozcan, “High-throughput lensfree 3d tracking of human sperms reveals rare statistics of helical trajectories,” *Proceedings of the National Academy of Sciences*, vol. 109, pp. 16018–16022, Sept. 2012.
- [78] B. J. Walker, S. Phuyal, K. Ishimoto, C.-K. Tung, and E. A. Gaffney, “Computer-assisted beat-pattern analysis and the flagellar waveforms of bovine spermatozoa,” *Royal Society Open Science*, vol. 7, p. 200769, June 2020.
- [79] R. Samuel, H. Feng, A. Jafek, D. Despain, T. Jenkins, and B. Gale, “Microfluidic—based sperm sorting & analysis for treatment of male infertility,” *Translational Andrology and Urology*, vol. 7, pp. S336–S347, July 2018.
- [80] C. Phiphattanaphiphop, K. Leksakul, R. Phatthanakun, and T. Khamlor, “A novel microfluidic chip-based sperm-sorting device constructed using design of experiment method,” *Scientific Reports*, vol. 10, Oct. 2020.
- [81] C. O. Reichhardt and C. Reichhardt, “Ratchet effects in active matter systems,” *Annual Review of Condensed Matter Physics*, vol. 8, pp. 51–75, Mar. 2017.
- [82] P. Denissenko, V. Kantsler, D. J. Smith, and J. Kirkman-Brown, “Human spermatozoa migration in microchannels reveals boundary-following navigation,” *Proceedings of the National Academy of Sciences*, vol. 109, pp. 8007–8010, May 2012.
- [83] J. Elgeti and G. Gompper, “Microswimmers near surfaces,” *The European Physical Journal Special Topics*, vol. 225, pp. 2333–2352, Nov. 2016.
- [84] A. P. Berke, L. Turner, H. C. Berg, and E. Lauga, “Hydrodynamic attraction of swimming microorganisms by surfaces,” *Physical Review Letters*, vol. 101, July 2008.
- [85] M. Molaei, M. Barry, R. Stocker, and J. Sheng, “Failed escape: Solid surfaces prevent tumbling of *Escherichia coli*,” *Physical Review Letters*, vol. 113, Aug. 2014.
- [86] P. Sartori, E. Chiarello, G. Jayaswal, M. Pierno, G. Mistura, P. Brun, A. Tiribocchi, and E. Orlandini, “Wall accumulation of bacteria with different motility patterns,” *Physical Review E*, vol. 97, Feb. 2018.

- [87] I. Berdakin, Y. Jeyaram, V. V. Moshchalkov, L. Venken, S. Dierckx, S. J. Vanderleyden, A. V. Silhanek, C. A. Condat, and V. I. Marconi, “Influence of swimming strategy on microorganism separation by asymmetric obstacles,” *Physical Review E*, vol. 87, May 2013.
- [88] R. Mok, J. Dunkel, and V. Kantsler, “Geometric control of bacterial surface accumulation,” *Physical Review E*, vol. 99, no. 5, p. 52607, 2019.
- [89] O. Sipos, K. Nagy, R. Di Leonardo, and P. Galajda, “Hydrodynamic Trapping of Swimming Bacteria by Convex Walls,” *Physical Review Letters*, vol. 114, no. 25, pp. 1–5, 2015.
- [90] P. K. Ghosh, V. R. Misko, F. Marchesoni, and F. Nori, “Self-propelled janus particles in a ratchet: Numerical simulations,” *Physical Review Letters*, vol. 110, June 2013.
- [91] H. A. Guidobaldi, Y. Jeyaram, C. A. Condat, M. Oviedo, I. Berdakin, V. V. Moshchalkov, L. C. Giojalas, A. V. Silhanek, and V. I. Marconi, “Disrupting the wall accumulation of human sperm cells by artificial corrugation,” *Biomicrofluidics*, vol. 9, p. 024122, Mar. 2015.
- [92] D. Bodas and C. Khan-Malek, “Hydrophilization and hydrophobic recovery of PDMS by oxygen plasma and chemical treatment—an SEM investigation,” *Sensors and Actuators B: Chemical*, vol. 123, pp. 368–373, Apr. 2007.
- [93] A. Guidobaldi, Y. Jeyaram, I. Berdakin, V. V. Moshchalkov, C. A. Condat, V. I. Marconi, L. Giojalas, and A. V. Silhanek, “Geometrical guidance and trapping transition of human sperm cells,” *Physical Review E*, vol. 89, Mar. 2014.
- [94] G. Volpe, S. Gigan, and G. Volpe, “Simulation of the active brownian motion of a microswimmer,” *American Journal of Physics*, vol. 82, pp. 659–664, July 2014.
- [95] M. S. Kumar and P. Philominathan, “The physics of flagellar motion of e. coli during chemotaxis,” *Biophysical Reviews*, vol. 2, pp. 13–20, Dec. 2009.
- [96] Thundathil, Gil, Januskauskas, Larsson, Soderquist, Mapletoft, and Rodriguez-Martinez, “Relationship between the proportion of capacitated spermatozoa present in frozen-thawed bull semen and fertility with artificial insemination,” *International Journal of Andrology*, vol. 22, pp. 366–373, Dec. 1999.

- [97] C. Alquézar-Baeta, S. Gimeno-Martos, S. Miguel-Jiménez, P. Santolaria, J. Yániz, I. Palacín, A. Casao, J. Á. Cebrián-Pérez, T. Muiño-Blanco, and R. Pérez-Pé, “OpenCASA: A new open-source and scalable tool for sperm quality analysis,” *PLOS Computational Biology*, vol. 15, p. e1006691, Jan. 2019.
- [98] E. Lauga, W. R. DiLuzio, G. M. Whitesides, and H. A. Stone, “Swimming in circles: Motion of bacteria near solid boundaries,” *Biophysical Journal*, vol. 90, pp. 400–412, Jan. 2006.
- [99] B. M. Friedrich, I. H. Riedel-Kruse, J. Howard, and F. Jülicher, “High-precision tracking of sperm swimming fine structure provides strong test of resistive force theory,” *Journal of Experimental Biology*, vol. 213, pp. 1226–1234, Apr. 2010.
- [100] H. V. Ramírez-Gómez, V. J. Sabinina, M. V. Pérez, C. Beltran, J. Carneiro, C. D. Wood, I. Tuval, A. Darszon, and A. Guerrero, “Sperm chemotaxis is driven by the slope of the chemoattractant concentration field,” *eLife*, vol. 9, Mar. 2020.